INSTITUT D'OPTIQUE GRADUATE SCHOOL

ÉCOLE DOCTORALE ONDES ET MATIERE

PHYSIQUE

THÈSE

pour l'obtention du grade de Docteur en science de l'Institut d'Optique Graduate School

préparée au Laboratoire Charles Fabry

date of thesis defence: 26/02/2016

par

Henning Labuhn

–

Rydberg excitation dynamics and correlations in arbitrary 2D arrays of single atoms

Directeur de thèse :	Antoine Browaeys	-	Laboratoire Charles Fabry
Composition du jury			
Rapporteurs :	Gerhard Birkl	-	Technische Universität Darmstadt
	Matt Jones	-	Durham University
Examinateurs :	Pierre Pillet	-	Laboratoire Aimé Cotton
	Matthias Weidemüller	-	Universität Heidelberg
Membres invités :	Thierry Lahaye	-	Laboratoire Charles Fabry

Contents

Chapter 1

Introduction

The ability to experimentally isolate, manipulate, and observe quantum systems at the single particle level has developed to an important tool in the study of quantum mechanics. Even though Erwin Schrödinger himself said as late as 1952 that it "is fair to state that we are not experimenting with single particles, any more than we can raise Ichthyosauria in the zoo", only that "in thought experiments, we sometimes assume that we do" [Schrödinger, 1952], scientist have long begun to study quantum mechanics on a single particle level. In 2012, the Nobel Prize in physics was awarded to Serge Haroche and David Wineland for their "ground-breaking experimental methods" in this field [Haroche, 2013; Wineland, 2013]. Since their pioneering results, one line of evolution from those fundamental experiments was to extend the investigation of single quantum systems to ensembles of larger numbers of interacting quantum particles. This allowed the study of fundamental quantum mechanical effects such as entanglement, probing e.g. the Bell inequalities [Brunner *et al.*, 2014] or the propagation of entanglement [Cheneau *et al.*, 2012; Jurcevic *et al.*, 2014].

The outstanding level of experimental control over such multi-particle quantum systems has furthermore led to a new field of research in quantum physics, the simulation of physical systems under well controlled conditions. Richard Feynman [1982] first proposed this idea of a quantum simulator more than 30 years ago, motivated by the fact that the information one needs to store on a classical computer for the numerical treatment of a quantum mechanical problem scales exponentially with the number of particles [Hauke *et al.*, 2012; Georgescu, Ashhab, and Nori, 2014].

For instance, due to the small length scales in condensed matter systems, it is often impossible to probe microscopic physical properties *in situ*. Likewise, the theoretical study of strongly correlated quantum systems on a microscopic level, such as electrons in a high T_c superconductor, often reaches the limit of what is possible to calculate numerically on a classical computer, as soon as the system size exceeds a few tens of particles.

Quantum simulation is an alternative approach to study such effects , which consists in 'building' a well-controllable quantum system, rules by the same many-body

Hamiltonian as the simulated system, with access to microscopic observables and phase diagrams in the laboratory. A prime example of this approach is the study of spin Hamiltonians. Despite their seemingly simple character, they can often be used to describe the complex dynamics in strongly correlated materials [Auerbach, 2012], yet for many cases especially the dynamics of the system cannot be computed on classical computers as soon as the system size exceeds a few tens of spins.

A useful quantum simulator, independent of the chosen system, needs to fulfil three main technical requirements, assuming already a successful implementation of a given model, i.e. that there is a direct mapping between the simulated system and the simulator [Somaroo *et al.*, 1999]. First, the quantum simulator needs to be scalable to large number of particles, in order to play out its advantage for example over a numerical simulation on a classical computer. Second, its coherence time needs to be sufficiently larger than the important timescales of the involved physics, in order to retain the quantum nature of the simulation. Third, the quantum simulator needs to be benchmarked, for instance against an analytically known solution or a numerical calculation in a regime where this is still possible, or a different quantum simulator, in order to the affirm the validity of a result when simulating a given problem.

The realisation of a fully reconfigurable quantum simulator fulfilling all three requirements has yet to be demonstrated. However, implementing aforementioned spin Hamiltonians in the lab has already proven to be successful with various quantum systems [Georgescu, Ashhab, and Nori, 2014].

Ions, trapped in a combination of static and oscillating electric and / or magnetic fields, arrange themselves due to their strong Coulomb repulsion, forming a so-called Coulomb crystal [Britton *et al.*, 2012; Monroe and Kim, 2013]. Both their internal and external degrees of freedom of the ions can be manipulated with high precision using lasers or microwave fields. The dynamics of the Coulomb crystal depends on the applied fields, and can be tuned such that it can be mapped to a spin Hamiltonian, with tunable, long-range interactions [Blatt and Roos, 2012; Schneider, Porras, and Schaetz, 2012; Monroe *et al.*, 2015]. Increasing the number of ions also increases the number of vibrational modes in the crystal, making the experimental control of the Coulomb crystal increasingly challenging when increasing the number of spins. However, a recent report claimed the generation of entanglement in a system of more than 200 ions [Bohnet *et al.*, 2015].

The quantum simulation of spin Hamiltonians with ultra-cold polar molecules is likewise under investigation [Ortner *et al.*, 2009; Peter *et al.*, 2015], and despite being technically challenging, large progress has been made in this field recently [Moses

et al., 2015].

Another promising platform are single neutral atoms trapped in optical lattices. The combination of tunnelling and on-site interaction of the atoms for example can be mapped on an Ising-type Hamiltonian [Simon *et al.*, 2011; Struck *et al.*, 2011]. The number of spins, i.e. single atoms, can be scaled relatively easily by increasing the size of the optical lattice, with the arrangement of the atoms being given by the underlying shape of the optical lattice. Even though complex geometries such as kagome lattices can be realised [Windpassinger and Sengstock, 2013], the flexibility of the geometry of optical lattices is somewhat limited. The generally weak interactions of neutral atoms provide a good isolation from the environment, thus limiting the effects of decoherence in the quantum system. However, the atom-atom interactions are therefore usually limited to nearest neighbours.

One possibility to generate interactions among neutral atoms that extend beyond nearest neighbours is to excite them to so-called Rydberg states, which are states where one of the electrons of the atom possesses a high principal quantum number n. In a classical picture of the atom, this corresponds to one electron orbiting far away from the ionic core on atomic length scales, thus forming an oscillating electric dipole. Two of such Rydberg atoms can show very strong dipolar interactions over distances of several tens of microns [Gallagher, 2005; Saffman, Walker, and Mølmer, 2010].

One consequence of those strong long-range interactions, and a major motivation for the study of Rydberg atoms itself, is the Rydberg blockade. It plays an important role in numerous proposals for both quantum simulation and its generalisation to any sort of computational problem [Nielsen and Chuang, 2011] in quantum information processing. The Rydberg blockade was first proposed for applications in quantum information by Jaksch *et al.* [2000] and Lukin *et al.* [2001]. The Rydberg blockade lies at the heart of many applications of Rydberg atoms, as for example for the realisation of quantum gates (see e.g. [Wilk *et al.*, 2010; Maller *et al.*, 2015; Jau *et al.*, 2015], or [Saffman, Walker, and Mølmer, 2010] for a review) highly non-classical states of light [Gorniaczyk *et al.*, 2014; Baur *et al.*, 2014], or the study of self-ordered phases of matter [Schauss *et al.*, 2015].

To picture the concept of Rydberg blockade, we consider an ideal two-level atom, made up of the ground state $|g\rangle$ and the Rydberg state $|r\rangle$, which are laser coupled with a coupling strength set by the Rabi frequency Ω. For two of those atoms, if their interatomic distance R is large, such that the van der Waals interaction V_{vdW} can be neglected compared to the laser coupling strength, i.e. $V_{\mathrm{vdW}} \ll \hbar\Omega$, the atoms can be seen as independent particles, and thus both can be excited to the Rydberg state at

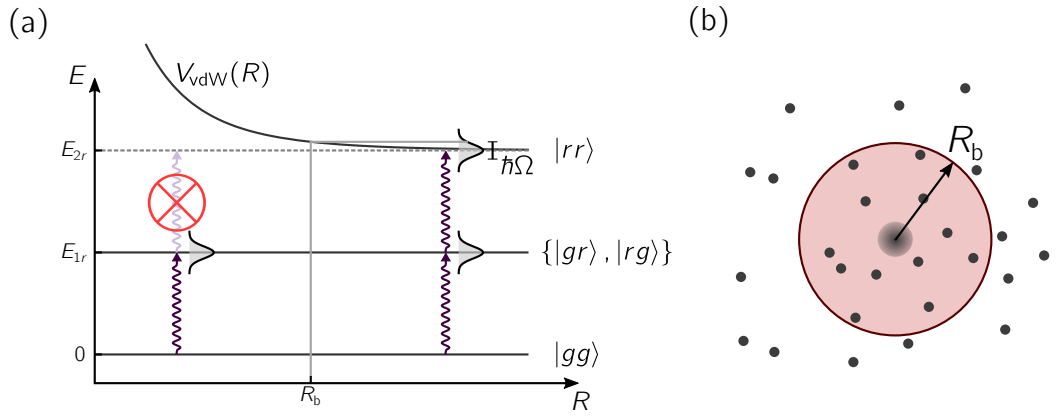

Figure 1.1: Illustration of the Rydberg blockade in the van der Waals regime. For large interatomic distances R, the energy shift $V_{vdW}(R)$ can be neglected compared to the coupling strength $\hbar\Omega$ between the ground and the Rydberg state, and the atoms behave independently from each other. For distances smaller than the blockade radius R_b, the excitation of $|rr\rangle$ is no longer resonant, leading to the blockade of a second Rydberg excitation. (b) Blockade sphere in an ensemble of atoms, for isotropic interactions.

the same time. On the other hand, for small interatomic distances, the van der Waals interaction between the Rydberg states can become very strong, and lead to an energy shift of the state $|rr\rangle$ where both atoms are in the same Rydberg state, of magnitude $V_{vdW}(R) = C_6/R^6$. If this energy shift is larger than the laser coupling strength, i.e. $V_{vdW}(R) \gg \hbar\Omega$, then the excitation of the doubly excited state is no longer possible, as depicted in Figure 1.1(a). This suppression of having more than a single excitation inside a certain volume is called Rydberg blockade. For the van der Waals interaction, the extension of the blockade volume is given by the blockade radius, the distance at which the interaction and the coupling strength are equal,

$$R_b = \sqrt[6]{\frac{C_6}{\hbar\Omega}}. \tag{1.1}$$

As the van der Waals interaction scales as $C_6 \sim n^{11}$, the blockade radius thus increases as $n^{11/6}$ with the principal quantum number n. For typical parameters of our experiment, the blockade radius is usually in a $2 - 20\,\mu$m range. The Rydberg blockade has been observed experimentally in cold atomic gases [Tong *et al.*, 2004; Singer *et al.*, 2004; Comparat and Pillet, 2010], optical lattices [Viteau *et al.*, 2011], Bose-Einstein condensates [Heidemann *et al.*, 2008; Balewski *et al.*, 2013], and for two single atoms [Urban *et al.*, 2009; Gaëtan *et al.*, 2009; Hankin *et al.*, 2014].

In this thesis, we present an original and complementary experimental approach for the quantum simulation of spin-1/2 particles, using single neutral atoms trapped in arbitrary two-dimensional arrays of microtraps, excited to Rydberg states. We holographically create 2D arrays of optical single-atom traps in arbitrary geometries, with trap separations ranging from $\sim 3\,\mu$m to a few tens of μm. In order to create strong correlations among the atoms, we coherently couple the ground-state atoms to Rydberg states. This allows us to observe the Rydberg blockade in systems of up to 15 atoms, having exact knowledge of the initially prepared number of ground state atoms. In a second set of experiments we reduce the Rydberg blockade radius to a few lattice sites. We can thereby simulate a system of spin-1/2 particles governed by the quantum Ising model, in different one- and two-dimensional arrays of up to 30 atoms. We benchmarked the measured Rydberg dynamics and correlations against a numerical simulation of an equivalent spin-1/2 system.

The results of this thesis have been realised together with Sylvain Ravets and Daniel Barredo, on an experiment built by Lucas Béguin and Aline Vernier [Béguin, 2013]. During the course of this thesis, we probed the interaction between two and three atoms, both for the regime of the van der Waals interaction and the regime of resonant dipole-dipole interaction [Ravets, 2014]. The main goal of my work was to extend the existing experimental setup to create arrays of single neutral atoms in arbitrary 2D geometries. The results presented here show that our experiment is an ideal candidate to study strongly-correlated many-body quantum systems.

This thesis is organised in the following way. In Chapter 2 we give an overview of the general experimental setup, the cooling and trapping of single atoms, and our Rydberg excitation scheme. In Chapter 3 we show how we can holographically create arbitrary arrays of optical microtraps by manipulating the spatial phase of a laser beam with a spatial light modulator. We thereafter in Chapter 4 present the spatially resolved state detection and manipulation of trapped single atoms. We present the main results obtained during this thesis, the collective Rydberg excitation of ensembles of up to 15 atoms in Chapter 5, and the observed spatial correlations of Rydberg excitation dynamics in various dimensions and geometries in Chapter 6. In Chapter 7 we probe the Rydberg blockade and the resulting collective enhancement for the case of resonant dipole-dipole interaction between two single atoms.

Parts of the results obtained during this thesis have been published in the following publications:

- **Single-atom trapping in holographic 2D arrays of microtraps with arbitrary geometries**
  Florence Nogrette, Henning Labuhn, Sylvain Ravets, Daniel Barredo, Lucas Béguin, Aline Vernier, Thierry Lahaye and Antoine Browaeys,
  Physical Review X **4**, 021034 (2014)

- **Single-atom addressing in microtraps for quantum-state engineering using Rydberg atoms**
  Henning Labuhn, Sylvain Ravets, Daniel Barredo, Lucas Béguin, Florence Nogrette, Thierry Lahaye and Antoine Browaeys,
  Physical Review A **90**, 023415 (2014)

- **Demonstration of a strong Rydberg blockade in three-atom systems with anisotropic interactions**
  Daniel Barredo, Sylvain Ravets, Henning Labuhn, Lucas Béguin, Aline Vernier, Florence Nogrette, Thierry Lahaye and Antoine Browaeys,
  Physical Review Letters **112**, 183002 (2014)

- **Coherent excitation transfer in a "spin chain" of three Rydberg atoms**
  Daniel Barredo, Henning Labuhn, Sylvain Ravets, Thierry Lahaye, Antoine Browaeys and Charles S. Adams,
  Physical Review Letters **114**, 113002 (2015)

- **Coherent dipole-dipole coupling between two single Rydberg atoms at an electrically-tuned Förster resonance**
  Sylvain Ravets, Henning Labuhn, Daniel Barredo, Lucas Béguin, Thierry Lahaye and Antoine Browaeys,
  Nature Physics **10**, 914917 (2014)

- **Measurement of the angular dependence of the dipole-dipole interaction between two individual Rydberg atoms at a Förster resonance**
  Sylvain Ravets, Henning Labuhn, Daniel Barredo, Lucas Béguin, Thierry Lahaye and Antoine Browaeys,
  Physical Review A **92**, 020701(R) (2015)

- **A highly-tunable quantum simulator of spin systems using two-dimensional arrays of single Rydberg atoms**
  Henning Labuhn, Daniel Barredo, Sylvain Ravets, Sylvain de Léséleuc, Tommaso Macrì, Thierry Lahaye and Antoine Browaeys,
  in preparation, arXiv preprint 1509.04543v2 (2015)

Chapter 2

Exciting a single atom to a Rydberg state

In recent years, research about Rydberg physics has seen an enormous revival. After the properties of Rydberg atoms had been studied extensively throughout the 20th century, its possible applications in quantum information, quantum simulation, and the study of fundamental physics re-sparked a large interest in the beginning of the 21st century [Saffman, Walker, and Mølmer, 2010].

Nowadays, the fields in which the properties of Rydberg states are used and studied, extend from cold [Mourachko *et al.*, 1998; Singer *et al.*, 2004] and ultra-cold atoms [Heidemann *et al.*, 2008; Viteau *et al.*, 2011; Schauß *et al.*, 2012] to hot vapours [Kübler *et al.*, 2010], ions [Feldker *et al.*, 2015], and even excitons in natural copper oxide crystals [Kazimierczuk *et al.*, 2014]. During the course this thesis, we have studied Rydberg excitations of arrays of single neutral atoms trapped in individual optical microtraps.

In this chapter, we will describe the characteristics of Rydberg states which are of importance for the rest of this thesis. We will then give a brief overview of the general setup of the experiment, and the mechanism which allows us to isolate a single neutral atom. We will show how we coherently couple the ground state of the single atom to a given Rydberg state using a coherent optical two-photon transition, and finally present the two regimes of the Rydberg-Rydberg interaction which are important in this thesis.

2.1 The interesting properties of Rydberg atoms

Rydberg atoms are atoms in an electronically highly excited state, meaning that one of its electrons has a large principal quantum number n, typically in the range $30 < n < 200$. They are named after Swedish physicist Johannes Rydberg, who generalised the empirical formula for the wavelengths of the spectral lines in hydrogen found by Balmer [Balmer, 1885] to other elements [Rydberg, 1890]. Building upon

the work of Rydberg, Niels Bohr later found a theoretical model [Bohr, 1913] for the binding energies in hydrogen,

$$E_n = -hc\frac{R_\infty}{n^2}, \tag{2.1}$$

which depends solely on the principal quantum number n of the atom, the Planck constant h, the speed of light c and the Rydberg constant R_∞. The Rydberg constant itself is defined only in terms of fundamental physical constants:

$$R_\infty = \frac{m_\mathrm{e}\, e^4}{8\,\varepsilon_0^2\, h^3\, c}, \tag{2.2}$$

where m_e is the rest mass of the electron, e the elementary charge and ε_0 the vacuum permittivity. One finds that, just like the binding energy, most properties of the hydrogen atom follow a characteristic scaling with n.

Alkali atoms, the elements in the first main-group of the periodic table, show a very similar behaviour, as they, just like hydrogen, posses only one valence electron. The electrons on the inner shells of the alkali atoms 'shield' all but one electric core charge. In good approximation, the single valence electron effectively only sees a single core charge, and thus behaves very similar to a hydrogen atom. However, if the valence electron is in low orbital angular momentum states $l \leq 3$, it can penetrate the inner shells of the atom, and thus see a slightly increased core charge compared to the valence electron of a hydrogen atom. One can use quantum defect theory [Jungen, 1988; Gallagher, 2005] to correct for this slight modification of the core charge. The

Table 2.1: Selection of scaling laws for properties of Rydberg atoms. The properties of Rydberg atoms follow universal scaling laws as a function of the effective principal quantum number n^* (from [Gallagher, 2005]).

property	**expression**	**scaling**	**value for** $82D$
binding energy	E_n	$(n^*)^{-2}$	500 GHz
electron orbital radius	$\langle r\rangle$	$(n^*)^{2}$	0.5 μm
lifetime (at $T = 300\,\mathrm{K}$)	τ	$(n^*)^{3}$	200 μs
polarisability	α	$(n^*)^{7}$	2500 MHZ/(V/cm)^2
transition dip. matrix element	$\langle 5P\vert\,\hat{\boldsymbol{d}}\,\vert nD\rangle$	$(n^*)^{-3/2}$	$0.01 ea_0$
energy level spacing	$E_{n+1} - E_n$	$(n^*)^{-3}$	12 GHz
resonant dipole-dipole coupling	C_3	$(n^*)^{4}$	25×10^4 MHZ μm^3
van der Waals coefficient	C_6	$(n^*)^{11}$	-9×10^6MHZ μm^6

Rydberg formula then changes to

$$E = -hc\frac{R^*}{(n^*)^2}, \tag{2.3}$$

with $n^* = n - \delta_\ell$ being the effective quantum number of the valence electron, δ_ℓ the so-called quantum defect, and the effective Rydberg constant $R^* = \frac{R_\infty}{1+m_\mathrm{e}/m_\mathrm{c}}$, where m_e and m_c are the electron and the atomic core mass respectively. The quantum defect is different for different electronic states, and depends mostly on the orbital angular quantum number ℓ and becomes small for $\ell \geq 3$. It also depends to a lesser extend to the total angular momentum quantum number j. Quantum defects for Rubidium have been measured accurately by millimetre-wave spectroscopy [Li *et al.*, 2003; Han *et al.*, 2006]. Together, one can easily compute the values of various atomic properties of different atomic species by using simple scaling laws, with a selection of them shown in Table 2.1.

We see that the strong scaling with n of both the resonant dipole-dipole interaction (scaling as $1/R^3$ with the distance) and the van der Waals interaction (scaling as $1/R^6$ with the distance) can result in interaction strengths of many MHz for atomic separations of several μm for high principal quantum numbers, making Rydberg states an ideal 'tool' for our experiment. The Rydberg-state lifetimes in the order of $100\,\mu$s are much longer than a typical duration of our experiment of $\sim 3\,\mu$s. On the other hand, the strong polarisability of Rydberg states makes them very sensitive to electric fields, so one needs to take care in the design of the experiment to keep the electric field as small as possible.

2.2 A short overview of the experimental setup

An experimental apparatus to perform Rydberg experiments with single atoms has to fulfil several requirements. We need:

- A reservoir of cold atoms, from which we eventually load atoms into the microtrap. A good loading rate of atoms into the trap is needed to ensure a fast duty cycle of the experiment.
- An optical dipole trap capable of reliably trapping a single atom.
- Both electric and magnetic field control to compensate for stray fields in the vicinity of the atoms, in order to achieve long coherence times.

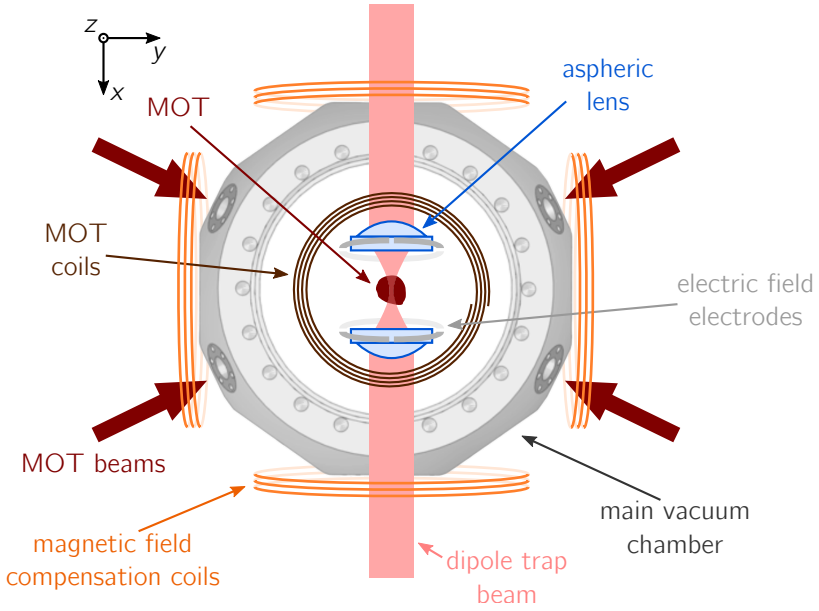

Figure 2.1: Schematics of the experimental vacuum chamber. The dipole trap beam is focused and recollimated by the pair of aspheric lenses. Its focus with a $\simeq 1\,\mu$m size is in the centre of a MOT of cold ^{87}Rb atoms. Four electrodes are placed around each aspheric lens, in order to apply arbitrary electric fields a the position of the atoms. Three pairs of magnetic field coils are used to define a quantisation axis in z-direction, and to compensate any transversal magnetic field in x- and y-direction. (The MOT beams, MOT and magnetic compensation coils in z-direction are not shown.)

- A laser system to coherently couple the ground state of the atom to Rydberg states.

- An imaging system capable of a spatially resolved state detection of the atoms.

In the following we will see how these points are realised in our experiment. An overview of the general experimental setup is given in the rest of this chapter. A more detailed description can be found in the PhD thesis of Lucas Béguin [2013]. The extension of the experiment to perform Rydberg experiments with arrays of single atoms, carried out during this thesis, will be described in the following chapters. The detailed implementation of creating arbitrary multi-trap arrays will be discussed in Chapter 3, and of the state detection of the atoms in Chapter 4.

2.2.1 The experimental apparatus

A schematic overview of the main vacuum chamber is shown in Figure 2.1. A magneto-optical trap (MOT) is loaded from a Zeeman slower to create our reservoir of cold ^{87}Rb atoms. As the interaction between Rydberg atoms is fairly independent of the atomic species, we chose to work with ^{87}Rb, since it is an element which is comparably straightforward to cool and trap. Additionally, since it is an alkali atom, its single valence electron is only weakly bound and can be excited to Rydberg states with commercially available lasers systems.

The MOT is placed between a pair of custom aspheric lenses[1] with a high numerical aperture of NA $= 0.5$ and an effective focal length of $f = 10\,\mathrm{mm}$, which focuses the dipole trap beam of wavelength 850 nm down to a waist $w_0 \simeq 1\,\mu\mathrm{m}$ [Sortais *et al.*, 2007]. The dipole trap beam is recollimated by the second aspheric lens, to image the trap intensity at the focal plane of the lenses onto a CCD camera.

As the polarisability of Rydberg states scales as n^7 with the principal quantum number, they become more and more sensitive to electric fields as one increases n. In order to avoid the mixing of Rydberg states due to electric fields, it is important to reduce the electric field at the position of the atoms as good as possible. In order to have very low stray fields in the first place, the flat side of the aspheric lenses facing the atoms is coated with a $\simeq 200\,\mathrm{nm}$ thick conductive layer of indium tin oxide (ITO) which is connected to ground.

In order to null any remaining electric fields, or to apply a specific electric field in any direction if needed, a set of eight electrodes is placed around the two aspheric lenses. This configuration allows to easily control the amplitude and the direction of the electric field at the position of the atoms. By performing Stark spectroscopy on Rydberg states we can compensate for stray electric fields, and achieve residual fields well below $\simeq 5\,\mathrm{mV/cm}$. A more detailed description of the electric field control can be found in the PhD theses of Lucas Béguin [2013] and Sylvain Ravets [2014].

Three independent pairs of Helmholtz coils, centred on the main axis of the vacuum chamber as shown in Figure 2.1, are used to apply a $+6\,\mathrm{G}$ quantisation field along the z-direction, while at the same time minimising stray transversal magnetic fields at the position of the single atoms. The calibration of the magnetic fields was done using Raman spectroscopy with Rydberg states, as was explained in [Béguin, 2013].

[1] The aspheric lenses were fabricated by LightPath Technologies.

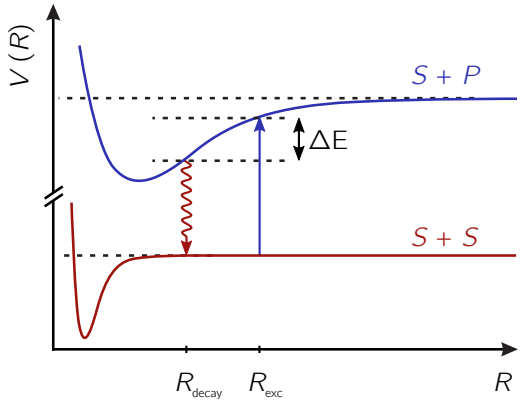

Figure 2.2: Schematics of the light-assisted collisions. The light from the collision beam (in our case the MOT beams) creates a loosely bound pair of an S- and P-state Rb atom. After a some time the pair decays back to ground state, with a kinetic energy ΔE acquired by the atoms.

2.2.2 Trapping a single atom in an optical microtrap

The core of our experimental apparatus is the possibility to trap an individual neutral ^{87}Rb atom in an optical microtrap. This technique was pioneered by Schlosser *et al.* [2001] at the Institut d'Optique more than a decade ago.

The optical microtraps are produced by focusing a far red-detuned dipole trap beam down to a $1/e^2$-radius of $w_0 \simeq 1\,\mu$m, approximately at the centre of our MOT. The light exerts a dipole force on the atoms, creating a conservative potential

$$U(\boldsymbol{R}) \propto \frac{I(\boldsymbol{R})}{\Delta} \tag{2.4}$$

for the atoms, with the dipole trap intensity $I(\boldsymbol{r})$ and the detuning Δ from the atomic transition [Grimm, Weidemüller, and Ovchinnikov, 2000]. With a typical total power of $P_0 \simeq 3.5\,$mW in the trap beam we measure a trap depth of $U_0 \simeq h \times 20\,$MHz $\simeq k_\mathrm{B} \times 1\,$mK.

Atoms will continuously enter the trap at random times from the reservoir of atoms in the MOT around the microtrap. The small volume of our trap, on the order of $\sim 1\,\mu\mathrm{m}^3$, allows us to work in a regime where, in timescales relevant to our experiment, at most one atom is present in the trap at the same time. This is due to inelastic light-assisted collisions between pairs of atoms in the microtrap. The principle of these collisions is depicted in Figure 2.2. When a pair of atoms in the $5S$ ground state is present in the trap, the MOT cooling light, which is slightly red-detuned from the

$5S \leftrightarrow 5P$ transition, will photo-associate the atoms to a loosely bound pair, with one atom in the $5S$ and the other atom in the $5P$ state. The pair will pick up kinetic energy ΔE by approaching the minimum of the potential curve, before radiatively decaying back to the ground state, after a time given by the lifetime of the bound state. As $\Delta E > U_0$, the two atoms are expelled from the trap[2], on a timescale of $\sim 1\,\mathrm{ms}$ [Fuhrmanek *et al.*, 2012].

In order to have at most one atom in the trap, the two-body loss rate must be larger than the rate with which the atoms are loaded into the microtrap from the MOT. This can easily be achieved by adjusting the density of atoms in the MOT [Schlosser, Reymond, and Grangier, 2002].

2.3 Atom-light interaction

All of the manipulations of our atoms are purely done by optical means. Moreover, the excitation of the atom to a Rydberg state is done in a coherent way using optical pulses. We can see the atoms as a two-level system consisting of the ground state $|g\rangle$ and a Rydberg state $|r\rangle$, which is coherently driven by the excitation light field. Such systems have been studied extensively (see e.g. [Cohen-Tannoudji, Dupont-Roc, and Grynberg, 1998]). Its dynamics can be described by the optical Bloch equations

$$\dot{\rho} = -\frac{i}{\hbar}\left[\hat{H}, \hat{\rho}\right] + \hat{\mathcal{L}}[\hat{\rho}], \tag{2.5}$$

with the Hamiltonian

$$\hat{H} = \begin{pmatrix} 0 & \Omega/2 \\ \Omega/2 & \delta \end{pmatrix}. \tag{2.6}$$

Here Ω and δ are the two-level Rabi frequency and the detuning from the atomic resonance. Dissipation, in our case mainly due to off-resonant spontaneous emission through the intermediate state, is taken into account by the Lindblad superoperator

$$\hat{\mathcal{L}}[\hat{\rho}] = \frac{\gamma}{2}(2\hat{\sigma}_{gr}\hat{\rho}\hat{\sigma}_{rg} - \hat{\sigma}_{rr}\hat{\rho} - \hat{\rho}\hat{\sigma}_{rr}), \tag{2.7}$$

with σ_{rg}, σ_{gr} being the transition operators between the ground and Rydberg state, σ_{rr} the projection operator on the Rydberg state, and γ a phenomenological damping rate.

[2] If the kinetic energy ΔE is shared unevenly among the atoms, it can happen that only one of the two atoms leaves the trap. We typically observe a probability of one atom remaining in the trap of $\sim 5\,\%$

One finds that, assuming that at $t = 0$ the entire population of the atom is in $|g\rangle$, the probability of a resonantly driven atom ($\delta = 0$) to be in the Rydberg state as a function of time is given by [Loudon, 2000]

$$P_r(t) = 1 - \frac{\Omega^2}{2\Omega^2 + \gamma^2}\left[1 + e^{-3\gamma t/4}\left(\cos(\tilde{\Omega}t) + \frac{3\gamma}{4\tilde{\Omega}}\sin(\tilde{\Omega}t)\right)\right], \tag{2.8}$$

with $\tilde{\Omega} = \sqrt{\Omega^2 + \gamma^2/4}$. For $\Omega \gg \gamma$, the population will thus undergo Rabi oscillations between the two states $|g\rangle$ and $|r\rangle$, with Rabi frequency Ω.

2.4 Driving coherent optical ground-Rydberg transitions

As soon as a single atom has been detected in the microtrap (for a description of the state detection of the atoms, see Chapter 4), we dispose of the atomic reservoir by turning off the MOT light for a few milliseconds, ending up with a single atom in the microtrap surrounded by vacuum. In this section we will describe how we coherently excite this isolated single ground state atom to a Rydberg state.

2.4.1 Ground state preparation

In order to coherently excite the trapped atom to a given Rydberg state with high efficiency, we need to prepare the atom in a well-defined initial ground state. After the MOT cooling light has been switched off, the MOT repumping light, driving the $\left|5S_{1/2}, F = 1\right\rangle \leftrightarrow \left|5P_{3/2}, F' = 2\right\rangle$ transition, is left on to trap the atomic state in the $F = 2$ hyperfine manifold of the $5S_{1/2}$ state. We then apply a $|\boldsymbol{B}| = +6.6\,\mathrm{G}$ magnetic field along the z-axis to have a well-defined quantisation axis, and optically pump the atom in the $|g\rangle = \left|5S_{1/2}, F = 2, m_F = 2\right\rangle$ stretched state, by a σ^+-polarised laser beam near-resonant with the $\left|5S_{1/2}, F = 2\right\rangle \leftrightarrow \left|5P_{3/2}, F' = 2\right\rangle$ transition.

2.4.2 Coherent two-photon excitation

The transition frequencies between the ground state and Rydberg states are typically in the ultraviolet. For Rubidium the transition frequency corresponds to a wavelength of $\sim 297\,\mathrm{nm}$. Coherent Rydberg excitations using single photon transition have been demonstrated recently [Hankin *et al.*, 2014], but the operation of laser systems with the appropriate wavelength is not an easy task, which is why we chose to use an

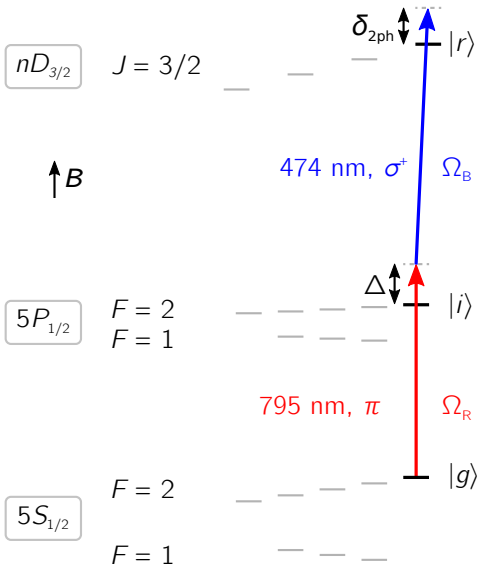

Figure 2.3: Relevant atomic states involved in the Rydberg excitation. The atoms are initially prepared in the ground state $|g\rangle = |5S_{1/2}, F = 2, m_F = 2\rangle$. A two-photon transition, off-resonant from the intermediate state $|i\rangle = |5P_{1/2}, F = 2, m_F = 2\rangle$ by $\Delta = 2\pi \times 740\,\text{MHz}$, couples to the Rydberg state $|r\rangle = |nD_{3/2}, m_j = 3/2\rangle$. As the hyperfine structure of Rydberg states is smaller than the linewidth of the laser excitation, we express the Rydberg state in the fine structure basis (level spacings are not to scale).

off-resonant two-photon excitation scheme instead (see Figure 2.3).

We couple the ground state $|g\rangle$ to the Rydberg state $|r\rangle = |nD_{3/2}, m_j = 3/2\rangle$, with a detuning from the intermediate state $|i\rangle = |5P_{1/2}, F = 2, m_F = 2\rangle$ of $\Delta = 2\pi \times 740\,\text{MHz}$, and single photon Rabi-frequencies Ω_R and Ω_B for the lower (red) and upper (blue) transition respectively.

We choose to work with Rydberg D- instead of S-states, since they show stronger optical coupling strengths, and larger Rydberg-Rydberg interactions, and the anisotropy in the van der Waals interaction of D states can lead to interesting physics in itself [Glaetzle *et al.*, 2014]. In addition, we experimentally observe a strongly increased dephasing of the Rydberg excitation when using S Rydberg state, that we so far cannot explain.

Since for our laser parameters $\Omega_\text{R}, \Omega_\text{B} \ll \Delta$, we can describe our two-photon excitation scheme as an effective one photon excitation of a two-level system, comprising the ground state $|g\rangle$ and the Rydberg state $|r\rangle$, with an effective two-level Rabi

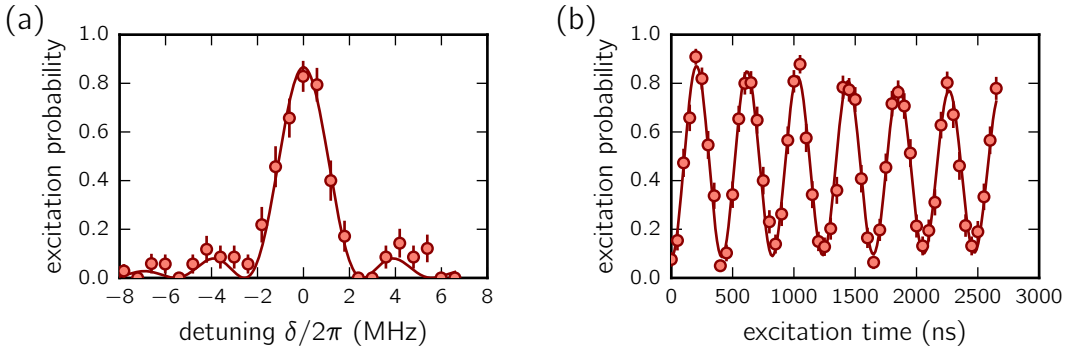

Figure 2.4: Rydberg excitation spectrum and Rabi oscillation. The plots show typical measurements for a Rydberg excitation, in this case of the $|55D_{3/2}\rangle$ state. (a) Rydberg excitation probability when scanning the laser detuning from the two-photon ground-Rydberg resonance. (b) The Rydberg excitation probability as a function of the excitation time for $\delta = 0$, showing the typical Rabi oscillation between the ground and Rydberg state. For each data point, the experiment was repeated ~ 100 times.

frequency and detuning given by

$$\begin{aligned} \Omega &= \frac{\Omega_{\mathrm{R}}\Omega_{\mathrm{B}}}{2\Delta} \\ \delta &= \delta_{2\mathrm{ph}} - \left(\frac{\Omega_{\mathrm{R}}^2}{4\Delta} - \frac{\Omega_{\mathrm{B}}^2}{4\Delta}\right). \end{aligned} \tag{2.9}$$

Two typical experiments to measure the parameters of the light-atom interaction with Rydberg states on a single atom are shown in Figure 2.4. We usually perform an experiment ~ 100 times for each data point to reconstruct the populations in the ground and Rydberg state. We can discriminate between ground and Rydberg atoms, since an atom is lost from the experiment if it was in the Rydberg state at the end of the excitation pulse, while it remains in its trap if it was in the ground state. A detailed description of our Rydberg detection scheme is given in Chapter 4. For both experiments, we start out with the atom in the ground state. Panel (a) shows the probability of the atom to be excited to the $|55D_{3/2}\rangle$ Rydberg state, as a function of the laser detuning δ from the effective two-photon resonance defined in Equation 2.9. The solid line shows a fit to the data of the function

$$P_r(\delta) = A + B\frac{\Omega^2}{\Omega^2+\delta^2}\sin\left(\frac{\tau}{2}\sqrt{\Omega^2+\delta^2}\right)^2, \tag{2.10}$$

with A and B being empirical fit parameters to incorporate the small detection error and the finite excitation efficiency (see Section 4.1.3 for details). Panel (b) again shows

the Rydberg excitation probability, this time for a resonant excitation ($\delta = 0$), as a function of the excitation time. As one expects, the atom undergoes Rabi oscillations between the ground and the Rydberg state. We typically work with optical Rabi frequencies between 0.5 MHz and 10 MHz. Smaller frequencies are limited by the maximum duration of our experiments of a few μs before we lose too many ground state atoms (see Section 4.1.3), for larger frequencies the decay from the intermediate state $|i\rangle$ in the two-photon excitation gets too large.

We observe single atom Rydberg excitation efficiencies of more than 95 %, which is the highest contrast of the Rabi oscillations that we measure on our experiment. The missing few percent in the contrast are due to an imperfect optical pumping to the ground state $|g\rangle$, and the spontaneous decay from the intermediate state in the two-photon excitation, which depends on the detuning Δ (which is fixed throughout this thesis), and the single photon Rabi frequency Ω_R of the first excitation step.

2.4.3 Excitation lasers

The light for the two-photon excitation is provided by two commercial lasers systems. For the 795 nm light we use a TOPTICA DL100, giving a total power of $\simeq 12$ mW at the position of the atoms, for the 474 nm light we use a frequency doubling TOPTICA TA-SHG-110 laser system, with $\simeq 90$ mW seen by the atoms. Both laser systems are frequency locked to a commercial ultra-stable ULE reference cavity from Stable Laser Systems, with a specified finesse of $\geq 20\,000$ and a free spectral range of 1.5 GHz.

By analysing the light reflected from the reference cavity we estimate laser linewidths of < 10 kHz for both the red and the blue excitation laser on the timescale of a few milliseconds. A linear drift of the cavity resonance was measured elsewhere to be ~ 10 kHz/day [Schauß, 2014], which is compatible with what we observe on our experiment. A more detailed description of the laser lock can be found in the thesis of Sylvain Ravets [2014], and a description of the laser optics and pulse shaping in the thesis of Lucas Béguin [2013].

Since according to Equation 2.9 both the effective Rabi frequency and detuning are dependent on the red and blue single photon Rabi frequencies, it is desirable to have the excitation light intensities as homogeneous as possible over a 2D array of atoms. We therefore use concave-convex cylindrical telescopes to magnify both beams by a factor ~ 4 in the axis which is parallel to the atomic plane, before focusing the red beam with an $f = 750$ mm plano-convex lens, and the blue beam with an $f = 300$ mm lens doublet (see Figure 2.5).

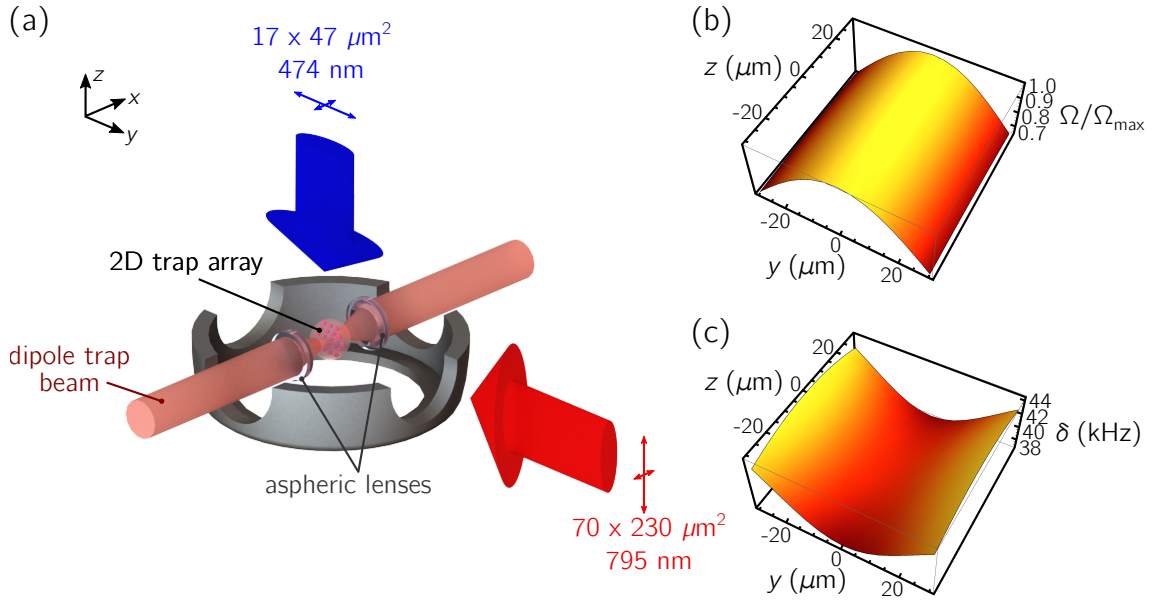

Figure 2.5: Shape of the excitation beams. (a) Sketch of the elliptical Rydberg excitation beams to ensure a homogeneous light intensity of both the 795 nm and the 474 nm beam even over large 2D arrays of single atoms in the yz-plane. For a typical Rydberg excitation experiment, with $n = 80$ and single photon Rabi frequencies $\Omega_R = 146\,\text{MHz}$ and $\Omega_B = 32\,\text{MHz}$, the expected variations of Rabi frequency (b) and light shift (c) are shown for a $50 \times 50\,\mu\text{m}^2$ area in the atom plane.

By measuring the two-photon Rabi frequency between the ground and a Rydberg state for different positions of a single atom in the focal plane of the aspheric lens, we determined $1/e^2$-radii of $w_R^{(x,z)} = (70, 230)\,\mu\text{m}$ for the red and $w_B^{(x,y)} = (17, 47)\,\mu\text{m}$ for the blue beam. With these measured beam parameters we expect variations of the effective Rabi frequency below 30 %, and variations of the light shift below 10 kHz, in a $25 \times 25\,\mu\text{m}^2$ square in the atomic plane (see Figure 2.5(b,c)). These remaining inhomogeneities, especially in the Rabi frequency, are due to the still relatively small waist w_B^y of the blue beam. Having chosen a larger waist would have meant a lower overall intensity of the blue light, thus smaller achievable Rabi frequencies. Choosing a higher aspect ratio while keeping the same peak intensity would have led to a very small w_B^x, which would be difficult to achieve due to possible aberrations when focusing the beam through the viewport. In addition, the beam would be difficult to align on the atoms and its position would have to be kept stable on a μm scale over several days.

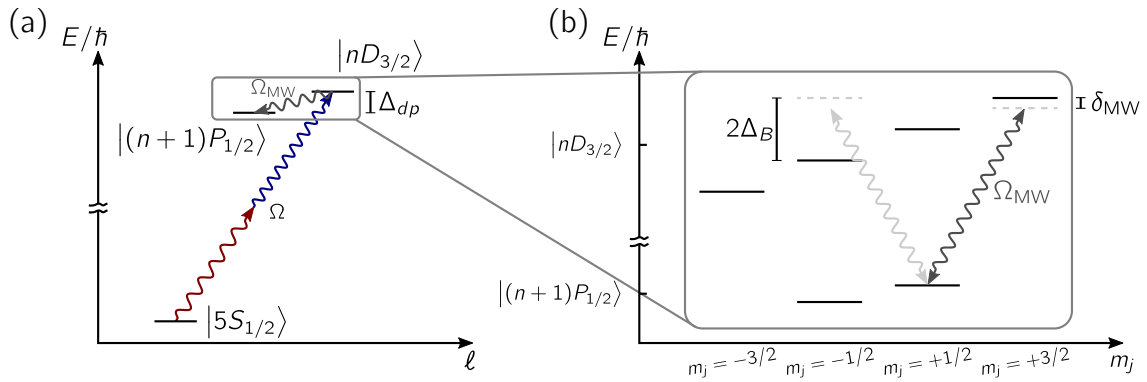

Figure 2.6: Realisation of Rydberg-Rydberg microwave transitions. (a) We first optically excite a ground state atom to a $|d\rangle = |nD_{3/2}\rangle$ Rydberg state. We turn off the optical light field, and use microwave radiation to drive transitions e.g. to a $|p\rangle = |(n+1)P_{1/2}\rangle$ state. (b) As our microwave field is unpolarised, we need the microwave coupling Ω_{MW} to be smaller than the Zeeman splitting Δ in order to be in the two-level regime.

2.5 Driving coherent microwave Rydberg-Rydberg transitions

In addition to driving coherent ground-Rydberg transition, it is also possible to drive coherent population transfers in the Rydberg manifold itself. The frequencies of these Rydberg-Rydberg transitions are typically a few to a few tens of GHz, making them convenient to drive with microwave fields from a standard microwave synthesiser. In our setup, we use a Rohde & Schwartz SMA100A microwave generator, connected to a simple antenna consisting of a 5 mm long end of a wire, positioned outside the vacuum chamber, just above a large viewport and about 20 cm away from the atoms. Due to the metallic parts of the aspheric lens mounts close to the atoms, which have spacings comparable to the microwave wavelength, the polarisation of the microwave field at the position of the atoms is unknown and is likely to have both circular and linear components.

To drive a single atom Rydberg-Rydberg transition, we first coherently excite the atom to a $|d\rangle = |nD_{3/2}\rangle$ Rydberg state by sending an optical π-pulse as described in Section 2.4.2. We then send in a coherent microwave pulse to transfer the population to another Rydberg state. Since we want to restrict the microwave transfer to a two-level process, it is convenient to drive microwave transitions to P states (see Figure 2.6(a)), which have a fine-structure splitting of a few hundred MHz, compared to a fine-structure splitting of around one MHz for F states. As we assume the microwave field to be unpolarised, we need the Zeeman splitting of the $|nD_{3/2}\rangle$ state Δ_B to

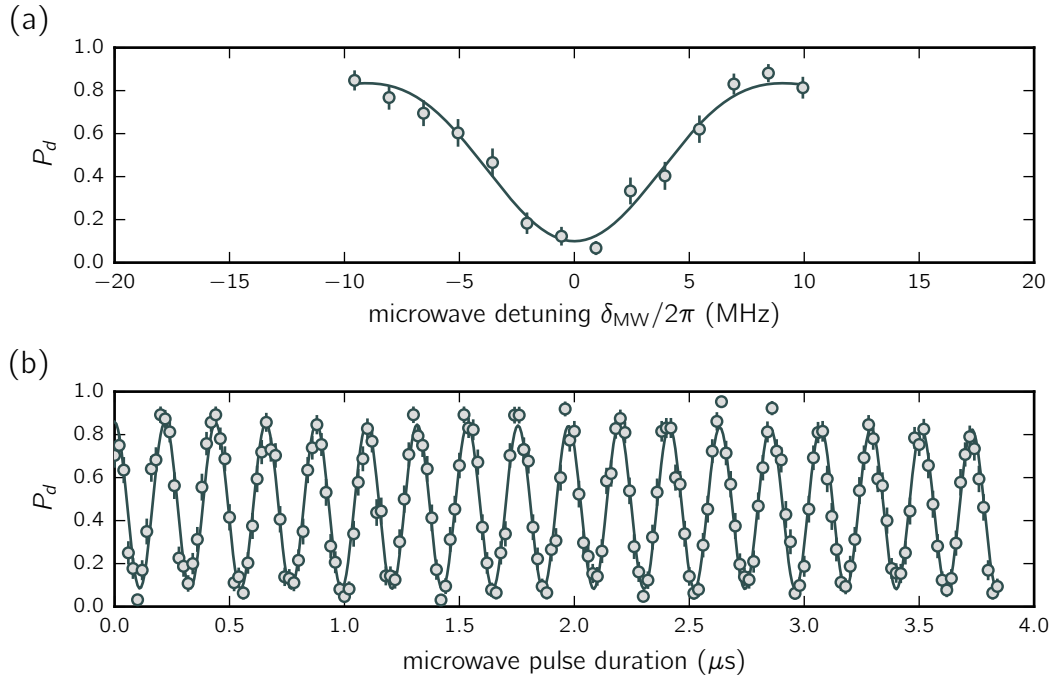

Figure 2.7: Microwave excitation spectrum and Rabi oscillation. We probe the microwave transition between the $|d\rangle = |62D_{3/2}\rangle$ and the $|p\rangle = |63P_{1/2}\rangle$ states. The atom is initially prepared in the $|d\rangle$ state. Probability P_d to find the atom in $|d\rangle$ as a function of (a) the detuning from resonance δ_{MW} after sending a $0.1\,\mu$s microwave pulse (the absolute transition frequency is $9\,131.6\,$MHz), and (b) the microwave pulse length at $\delta_{\mathrm{MW}} = 0$. We measure a Rabi frequency of $\Omega_{\mathrm{MW}} \simeq 2\pi \times 4.5\,$MHz without seeing any noticeable damping of the oscillation.

be larger than the microwave coupling strength Ω_{MW}, in order not to transfer any population into other Zeeman-sublevels of the D-state, as depicted in Figure 2.6(b).

To detect whether the atom was in the $|d\rangle$ or in another Rydberg state at the end of the experiment, we again shine in another optical π-pulse which transfers all population in $|d\rangle$ back to the ground state $|g\rangle$. If the optical down-transfer were perfect, measuring the population in $|g\rangle$ would give the population in $|d\rangle$ at the end of the experiment.

Figure 2.7 shows an experiment probing the microwave transition between the $|d\rangle = |62D_{3/2}\rangle$ and the $|p\rangle = |63P_{1/2}\rangle$ state. In this case we have a Zeeman splitting of $\Delta_B \approx 7.5\,$MHz for the D-state for our magnetic field of $|\boldsymbol{B}| = 6.6\,$G. We use an output power of the microwave synthesiser of about $-15\,$dBm, with which we expect a Rabi frequency of about $2\pi \times 5\,$MHz for the chosen states. Panel (a) shows the final population in $|g\rangle$ after having shone in a microwave pulse with a $0.1\,\mu$s duration, as a function of the detuning δ_{MW} from the $|62D_{3/2}\rangle \leftrightarrow |63P_{1/2}\rangle$ resonance. We

find an absolute value of $\Delta_{dp} \simeq 2\pi \times 9\,131.6\,\mathrm{MHz}$, close to the calculated value of $2\pi \times 9\,131.5\,\mathrm{MHz}$ using quantum defect theory.

For the same experimental parameters, we tune the microwave frequency to resonance, i.e $\delta_{\mathrm{MW}} = 0$, and measure the final population in $|d\rangle$ as a function of the microwave pulse length. We fit the data by a damped sine, and find a Rabi frequency $\Omega_{\mathrm{MW}} \simeq 4.558\,\mathrm{MHz}$. In contrast to the optical Rabi oscillation, we do not see any measurable damping in the microwave driven Rabi oscillation. This is because we do not suffer from the same sources of decoherence, namely that there is no short-lived intermediate state involved in the transition, and the microwave synthesiser is extremely stable both in frequency and in power. In addition, we can conclude that the microwave field is mainly a combination of σ_+ and σ_- polarisation, as we do not seem to couple to the $\left|62D_{3/2}, m_j = +1/2\right\rangle$ state. If we increase the Rabi frequency such that $\Omega_{\mathrm{MW}} \approx 2\Delta_B \approx 2\pi \times 15\,\mathrm{MHz}$, we indeed do see a strong damping of the Rabi oscillation as we now start to transfer a significant amount of the population into different Zeeman-sublevels of the $|d\rangle$ state as described above. The finite contrast of the oscillation is fully attributed to the finite optical excitation and de-excitation probability.

2.6 Rydberg-Rydberg interactions

The principal motivation to use Rydberg states are their large interaction strengths. For two Rydberg atoms separated by a few μm, which is the typical interatomic separation in the experiments in this thesis, the Rydberg-Rydberg interaction is usually in the order of MHz and thus more than 10 orders of magnitude larger than the interaction between two ground state atoms at the same distance [Saffman, Walker, and Mølmer, 2010]. Moreover, one can easily tune the strength of the interaction by choosing Rydberg states with different principal quantum numbers, or by changing the distance between the atoms.

Due to the large transition dipole matrix element between Rydberg states, the dominant interaction between two Rydberg atoms is by far the dipole-dipole interaction, as long as the atomic separation is larger than the extend of the electronic wave function, i.e. $|\boldsymbol{R}| \gg n^2 a_0$. In a quantum mechanical picture, the interaction between two Rydberg atoms is described by the dipole-dipole interaction operator

$$\hat{V}_{\mathrm{dd}}(\boldsymbol{R}) = \frac{1}{4\pi\epsilon_0}\left(\frac{\hat{\boldsymbol{d}}_1 \cdot \hat{\boldsymbol{d}}_2}{R^3} - \frac{3(\hat{\boldsymbol{d}}_1 \cdot \boldsymbol{R})(\hat{\boldsymbol{d}}_2 \cdot \boldsymbol{R})}{R^5}\right), \tag{2.11}$$

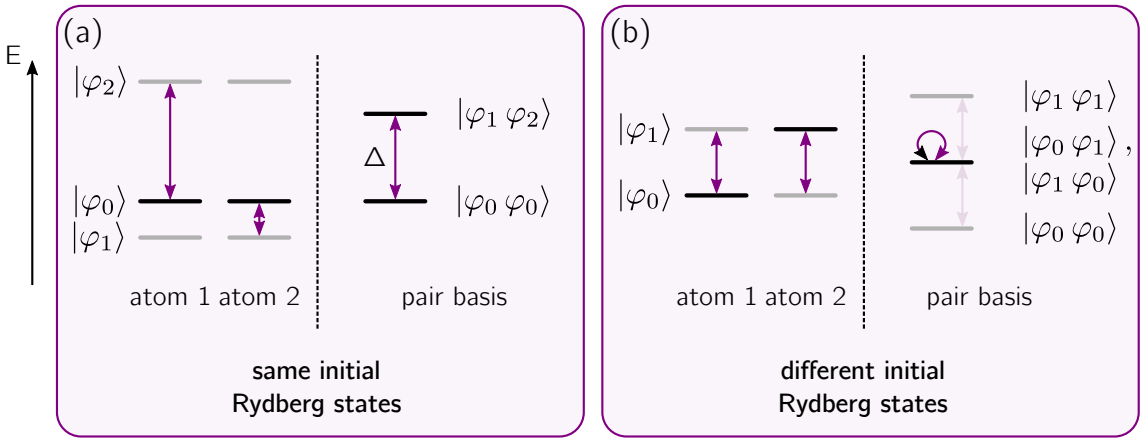

Figure 2.8: Schematic energy levels of atomic pair states. (a) Both atoms prepared in the state same state $|\Phi_0\rangle = |\varphi_0\varphi_0\rangle$, which is coupled by the dipole-dipole interaction to a state $|\Phi_1\rangle = |\varphi_1\varphi_2\rangle$ with an energy difference Δ. (b) The atoms are prepared in two different Rydberg states, $|\Phi_0\rangle = |\varphi_0\varphi_1\rangle$, which is degenerate and thus resonantly coupled to $|\Phi_1\rangle = |\varphi_1\varphi_0\rangle$, where the atoms have exchanged their Rydberg states.

where $\hat{\boldsymbol{d}}_1$ and $\hat{\boldsymbol{d}}_2$ are the electric dipole moment operators of atom one and two respectively, $\boldsymbol{R}$ the vector connecting the two atoms and $R = |\boldsymbol{R}|$.

Since the internal electronic dynamics of Rydberg atoms typically happens much faster than their external dynamics, i.e their motion, we can treat the atomic cores as fixed in space when calculating the eigenenergies of the interacting system. When the atomic separation is larger than the spatial extend of the electron wave function, which is always the case in the experiments presented in this thesis, the two-atom Hamiltonian can be written as

$$\hat{H} = \hat{H}_1 \otimes \mathbb{1} + \mathbb{1} \otimes \hat{H}_2 + \hat{V}_{\mathrm{dd}}(\boldsymbol{R}), \tag{2.12}$$

where $\hat{H}_1$ and $\hat{H}_2$ are the free atom Hamiltonians of the two atoms.

In order to find the eigenenergies of the interacting two-atom system, one can diagonalise the Hamiltonian numerically. In theory one needs to take into account all possible atomic pair states for the interaction. However, only pair states that are energetically close to the original state contribute significantly to the interaction.

Here, in order to gain qualitative insight into the different regimes of the dipole-dipole interaction, we will consider a simple model system of two atoms with only two possible pair states $|\Phi_0\rangle$ and $|\Phi_1\rangle$, as shown in Figure 2.8. In the pair basis $\{|\Phi_0\rangle, |\Phi_1\rangle\}$, the

Hamiltonian of the system is given by

$$\hat{H} = \begin{pmatrix} 0 & V_0/R^3 \\ V_0/R^3 & \Delta \end{pmatrix}, \tag{2.13}$$

with $V_0/R^3 = \langle \Phi_1 | \hat{V}_{\mathrm{dd}}(\boldsymbol{R}) | \Phi_0 \rangle$ being the dipole-dipole coupling strength between the two pair states, and Δ their energy difference. The eigenenergies of the system are given by

$$E_{\pm} = \frac{1}{2}\left(\Delta \pm \sqrt{\Delta^2 + 4V_0^2/R^6}\right). \tag{2.14}$$

We see that the eigenenergies depend strongly on the distance R between the atoms, and one can identify two very distinct regimes of the interaction.

- **van der Waals interaction ($V_0/R^3 \ll \Delta$):**

  Let us first consider the case where both Rydberg atoms are initially in the same state, e.g. $|\Phi_0\rangle = |\varphi_0\varphi_0\rangle$, where φ_i are the atomic states in the single atom basis, as shown in Figure 2.8(a). In most cases, the dipole-dipole coupling strength V_0/R^3 for interatomic distances presented in this thesis is much smaller than the energy difference Δ between the different atomic pair states, so the interaction can be treated as a small perturbation on the eigenenergies of the non-interacting pair states. The eigenenergies of Equation 2.14 can therefore be approximated by

  $$E_+ \simeq \Delta + \frac{C_6}{R^6} \quad \text{and} \quad E_- \simeq -\frac{C_6}{R^6},$$

  with $C_6 = V_0^2/\Delta$, leading to the well-known van der Waals interaction with its R^{-6} scaling, and increasing with the principal quantum number as $C_6 \sim n^{11}$.

  For typical experimental parameters in our experiment, with the principal quantum number n ranging between 50 and 100, and interatomic distances between 3 and 10 μm, the interaction strengths in the van der Waals regime can range from a few kHz to hundreds of MHz. This demonstrates the versatility of Rydberg atoms, as it is easily possible for us to tune the interaction strength between the atoms by a few orders of magnitude only by changing the position of the atoms or their principal quantum number[3]. The van der Waals interaction

[3] For lower principal quantum numbers the finite lifetime of the Rydberg atoms becomes non-negligible for the timescales of our experiments, whereas for higher ones it gets more and more difficult to compensate stray electric fields to a satisfactory level, as the polarisability of the Rydberg states grows with $(n^*)^7$ and gets very large for high lying Rydberg states.

is the only relevant interaction in the experiments presented in this thesis except for Chapter 7, as we always couple all the atoms to the same Rydberg state.

- **Resonant dipole-dipole interaction** ($V_0/R^3 \gg \Delta$):

  The second interaction regime occurs when the dipole-dipole interaction couples two pair states resonantly, i.e. the energy difference Δ is zero or negligible compared to the dipole-dipole coupling strength V_0/R^3. The eigenenergies of the pair state from Equation 2.14 then simplify to

$$E_{\pm} \simeq \pm\frac{V_0}{R^3} = \pm\frac{C_3}{R^3}, \tag{2.15}$$

  with $V_0 = C_3$, showing the typical R^{-3} scaling of the resonant dipole-dipole interaction. The condition $\Delta \simeq 0$ can be achieved in two different ways.

  Förster resonance: If both atoms are initially in the same Rydberg states, as shown in Figure 2.8(a), it is still possible to find cases where the interaction is dominated by the resonant dipole-dipole interaction. This is the case if the initial pair state is near-degenerate with a second pair state where both atoms have a different Rydberg state, and both states are coupled via the dipole-dipole interaction. In general, there exist very few pair states in nature that fulfil this condition. One can, however, tune two quasi-degenerate pair states into resonance, for example by applying an electric field [Walker and Saffman, 2005; Anderson, Veale, and Gallagher, 1998; Mudrich *et al.*, 2005], as we have demonstrated in [Ravets *et al.*, 2014, 2015]. Using electric fields, it is even possible to find degenerate triple-states, as was demonstrate recently by Faoro *et al.* [2015].

  Excitation transfer: If the two atoms are in two different Rydberg states, i.e. $|\Phi_0\rangle = |\varphi_0\varphi_1\rangle$, there exists another degenerate[4] pair state $|\Phi_1\rangle = |\varphi_1\varphi_0\rangle$ where the atoms have exchanged their states, depicted in Figure 2.8(b).

  The two states are thus coupled resonantly by the dipole-dipole interaction, as now $\Delta = 0$, and the system will oscillate between $|\Phi_0\rangle$ and $|\Phi_1\rangle$ with a frequency $C_3/(hR^3)$, as we have shown in [Barredo *et al.*, 2015]. The pair state $|\Phi_0\rangle$ is naturally still coupled to other off-resonant states by the van der Waals interaction, but if $\Delta n = |n_1 - n_0| \approx 0$ then the resonantly coupled state completely dominates the interaction and the van der Waals interaction can usually be neglected.

[4] Assuming the absence of spatially varying electric or magnetic fields.

The effect of the resonant dipole-dipole interaction will be discussed briefly in Chapter 7.

2.7 Conclusion

In this chapter we presented the setup to trap a single atom in a microtrap created by the focus of an optical dipole trap beam, and coherent excitation scheme to couple the atom to a Rydberg state. The strong interaction between Rydberg atoms make them an ideal tool to engineer strongly interacting many-body quantum systems in the laboratory. In order to achieve this goal, we need to create not only one, but large arrays of single-atoms traps. In the following chapter we will see how we can create arrays of microtraps in arbitrary 2D configurations by manipulating the phase of our dipole trap beam.

Chapter 3

Generation of arbitrary 2D arrays of optical dipole traps

In order to study the many-body physics of interacting Rydberg atoms, it is necessary to multiply the number of microtraps. In the Rydberg physics community, multiple approaches have been taken to create arrays of atomic traps containing either one or an ensemble of atoms. The techniques used range from simply using multiple dipole trap beams [Béguin *et al.*, 2013; Hankin *et al.*, 2014; Ebert *et al.*, 2015] to optical lattices [Schauß *et al.*, 2012] and arrays of microtraps created by fixed optics [Maller *et al.*, 2015].

A drawback of those approaches is the lack of flexibility in the arrangement of the atoms. One possibility to overcome this limitation is the use of a spatial light modulator (SLM) to either imprint an intensity pattern on the Rydberg excitation light [van Bijnen *et al.*, 2015], or to create reconfigurable arrays of microtraps [Bergamini *et al.*, 2004; Kruse *et al.*, 2010; Schlosser *et al.*, 2011; Nogrette *et al.*, 2014].

For the work of this thesis we chose the latter approach, 'cloning' the single microtrap by imprinting an appropriate spatial phase on the dipole trap beam, allowing us to create up to ~ 100 traps in easily reconfigurable 2D geometries.

This chapter is based on our publication [Nogrette *et al.*, 2014]. We will first discuss the principle of manipulating the spatial phase of a Gaussian beam to change its intensity distribution in the focal plane of a lens in Section 3.1. In Section 3.2 we present the actual implementation in the experiment. Finally, we will see how we use the SLM to correct for aberrations of the trapping beam in Section 3.3, and the use of a closed feedback loop to achieve uniform trap intensities in Section 3.4.

3.1 Spatial phase manipulation of a Gaussian beam

Holography was originally intended to record both the intensity and the spatial phase information of a light field [Gabor, 1948]. Only later the technique was used to actively

manipulate the light-intensity distribution, typically by using a transparent optical element with a spatially varying index of refraction, and uniform absorption. Such elements have to be specifically fabricated for a certain desired intensity pattern.

A major evolution of the field was thus the emergence of digital holography and the use of liquid crystal devices called spatial light modulators (SLMs) [Osten, 2006], allowing the dynamic manipulation of the spatial phase of the light field. SLMs are arrays of pixels consisting of bi-refringent liquid crystals, similar to those found in liquid crystal displays. Each pixel can introduce a polarisation-dependent phase shift to either a reflected or transmitted light field, depending on the type of SLM, with a magnitude that can be controlled for each pixel independently. It is therefore possible to control the local phase of the light field with a resolution equal to that of the pixel array of the SLM.

There are two different types of SLMs, *optically*-addressed spatial light modulators (OASLMs) and *electrically*-addressed spatial light modulators (EASLMs), the difference being that the former one uses a control light field to imprint the phase information on the pixel array, the latter one by applying a computer controlled electric field to each pixel. For our experiment we use an EASLM, which we will from now on only refer to simply as SLM. Nowadays SLMs are commercially available with resolutions up to several megapixels, with a resolution of the phase shift better than $2\pi/100$ on each pixel and refresh rates of up to more than 100 Hz.

SLMs have seen various applications in physics research, ranging from the manipulation of angular momentum states of light [Curtis and Grier, 2003; Gibson *et al.*, 2004; Bozinovic *et al.*, 2013], trapping of polarisable particles [Grier, 2003], aberration correction in astronomy [Hardy, 1998], laser pulse shaping [Weiner, 2000], to the manipulation of degenerate quantum gases [Boyer *et al.*, 2006; Becker *et al.*, 2008] and creating exotic trap potentials for them [Gaunt and Hadzibabic, 2012].

For all above mentioned applications it is crucial to find an appropriate phase to imprint on the light field in order to create the desired intensity distribution. One way this can be achieved will be detailed in the following two subsections.

3.1.1 Optical phase modulation using a spatial light modulator

We will now discuss the working principle to create a desired intensity distribution of a light field in the focal plane of a lens by altering the spatial phase of a Gaussian beam. The most simple use of an SLM is shown schematically in Figure 3.1. Note that the coordinate system (x, y, z) used to describe the light field for the SLM is different

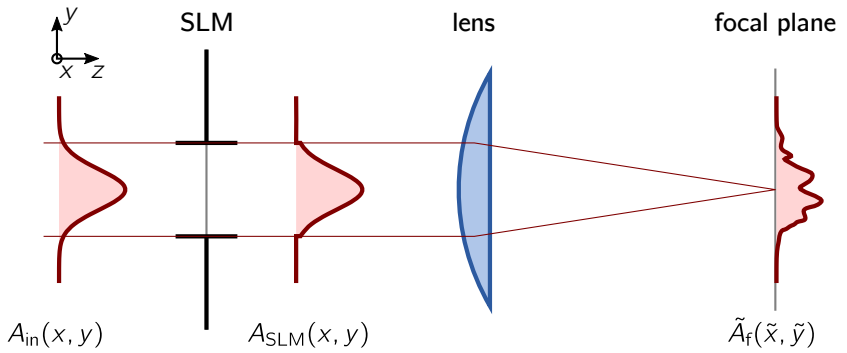

Figure 3.1: Principle of the phase manipulation with an SLM. The SLM imprints a chosen phase $\varphi(x, y)$ onto the light field. Due to its finite size, the SLM effectively acts as an aperture, but besides that does not alter the intensity of the light field. The intensity distribution in the focal plane of a lens depends strongly on the spatial phase of the collimated beam.

from the coordinate system of the actual experiment. A collimated Gaussian beam with a uniform spatial phase and a real-valued amplitude $A_{\text{in}}(x, y) = |A_{\text{in}}(x, y)|$ is incident on the SLM. We assume the SLM to act as a rectangular aperture, with the size $L_x \times L_y$ of the SLM, which modifies the phase of the beam at position (x, y) by an amount $\varphi\,(x, y)$. Immediately after the SLM the complex amplitude of the beam is then given by

$$A_{\text{SLM}}(x, y) = A_{\text{in}}(x, y) e^{i\varphi(x,y)} \,\text{rect}\left(\frac{x}{2L_x}, \frac{y}{2L_y}\right), \tag{3.1}$$

with rect$(\cdot)$ being the rectangular function making up for the finite aperture of the SLM. When the beam is now focused by a lens of focal length f, its amplitude in the focal plane is given by

$$\tilde{A}_{\text{f}}(\tilde{x}, \tilde{y}) = \mathcal{F}\left[A_{\text{SLM}}(x, y)\right]_{\frac{\tilde{x}}{\lambda f}, \frac{\tilde{y}}{\lambda f}}. \tag{3.2}$$

Here λ is the wavelength of the light field and $\mathcal{F}\left[\cdot\right]_{\mu,\nu}$ the Fourier transform at frequencies μ, ν.

Since the result of the Fourier transform in Equation 3.2 can depend strongly on the phase $\varphi(x, y)$, we can drastically change the intensity distribution $I_{\text{f}} = |\tilde{A}_{\text{f}}|^2$ in the focal plane of the lens by changing $\varphi(x, y)$. The easiest way to achieve any arbitrary intensity distribution in the focal plane would be to take the inverse Fourier transform of $\sqrt{I_{\text{f}}}$, and modify the phase and the amplitude of the light field accordingly. This is not applicable here since the SLM which we use in the experiment only allows the manipulation of the phase φ, not the amplitude $|A_0|$. It is therefore not possible,

except for some trivial cases, to find a phase φ which will exactly give a desired target intensity distribution I_t such that $|\tilde{A}_\mathrm{f}|^2 = I_\mathrm{t}$. However, it is possible to find phases φ which will give a good approximation for any given desired intensity distribution in the focal plane. A trivial case to manipulate the light field will be given in the following, namely displacing the trap transversally with respect to the optical axis, before detailing the Gerchberg-Saxton algorithm to find appropriate phases for arbitrary target intensity distributions.

The most simple manipulation of the phase of the light field is to move a single trap transversally in the focal plane. This is achieved in general by adding a tilt to the wavefront of the laser beam, which can be achieved by adding with the SLM a phase shaped as a blazed grating of the form

$$\varphi(x, y) = \left(\frac{2\pi}{\Lambda_x}x + \frac{2\pi}{\Lambda_y}y\right) \mod 2\pi, \tag{3.3}$$

where Λ_x and Λ_y are the fringe periods of the grating in x- and y-direction. Such a grating can be superimposed on any phase on the SLM in order to shift the intensity distribution as a whole transversally in the focal plane of the lens by a quantity $(\Delta x, \Delta y) = (f\lambda/\Lambda_x, 1/f\lambda/\Lambda_y)$, f being the focal length of the lens and λ the wavelength of the light.

Furthermore, we can display any analytically calculable phase on the SLM. A simple example is to display two areas of constant phase with a π phase jump between them, changing the Gaussian beam from a TEM_{00} to a TEM_{01} mode. In the focal plane, this will lead to two sharply separated traps with a peak-to-peak distance of $\sim 1.6\,\mu$m. This is the fundamental limit of how close we can bring two traps together. Preliminary experiments showed that the atom-loss probability is significantly increase for such a small distance, but nevertheless allowed us to perform a two-atom Rydberg experiment.

3.1.2 The Gerchberg-Saxton phase retrieval algorithm

In order to create arbitrary intensity distributions in the focal plane of a lens with a phase-only SLM, the algorithm of choice is usually the Gerchberg-Saxton algorithm [Gerchberg and Saxton, 1972], which is explained schematically in Figure 3.2. It was originally developed to retrieve the phase information of an electron beam from its intensity distribution. It can however also be used to find an approximate phase for a laser beam to generate a desired light intensity in the focal plane of a lens, which is

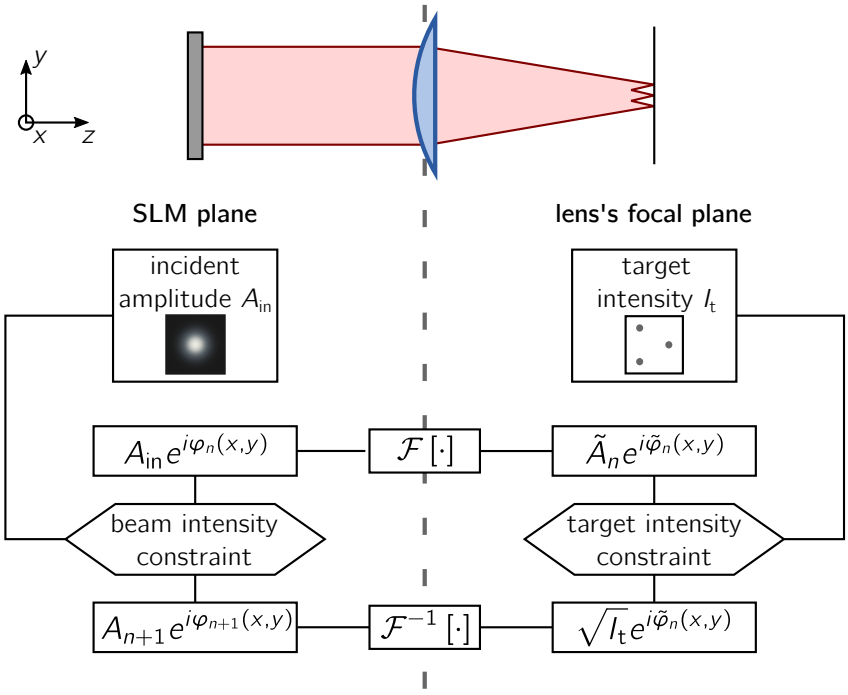

Figure 3.2: Principle of the Gerchberg-Saxton algorithm. In the algorithm, the light field is repeatedly propagated back and forth between the SLM plane and the focal plane by Fourier and inverse Fourier transform. In each iteration n of the algorithm, the amplitude in the SLM plane is replaced by the real incident amplitude A_0, and the amplitude in the focal by the target amplitude $\sqrt{I_t}$, keeping only the complex phase.

exactly what we are looking for to create arbitrary trap geometries with our SLM.

The principle of the GS algorithm is to virtually propagate the light field back and forth between the plane of the SLM and the focal plane of the lens, iteratively converging towards an appropriate phase to create a given intensity distribution. Since we work in the far field regime, the light field propagation can be done by Fourier and inverse Fourier transform [Goodman, 1996]. One iteration of the algorithm looks as follows:

- We start out with the actual real amplitude of the light field A_{in}, which in our case is a Gaussian beam having passed through an aperture the size of the SLM.
- The light field is propagated to the focal plane of the lens by Fourier transform, giving us the amplitude $\tilde{A}$ and the phase $\tilde{\varphi}$ of the focused beam.
- In the focal plane, we replace the calculated amplitude $\tilde{A}$ by the amplitude of the target intensity distribution $\sqrt{I_t}$, while keeping the calculated phase $\tilde{\varphi}$.

- We propagate the light field back to the SLM plane by inverse Fourier transform.
- The calculated amplitude in the SLM plane is now replaced by the actual real amplitude A_{in} of the incident light field, while keeping again the calculated phase φ.
- We repeat the algorithm until the calculated amplitude in the SLM plane $|\tilde{A}e^{i\tilde{\varphi}}|^2$ does not evolve anymore, usually after a few tens of iterations.

Note that this algorithm only converges to an *approximation* of the targeted intensity distribution I_{t}, as we are not able to manipulate the amplitude of the light field. In fact, there exist a large number of different phases that lead to equally good approximations of I_{t}. As the algorithm is completely deterministic, the phase which is finally found only depends on the initial implementation of the algorithm[1]. The numerical implementation of the Gerchberg-Saxton algorithm will be detailed in the following Section.

3.1.3 Phase retrieval on a discrete grid

In order to calculate an appropriate phase pattern to create a specific microtrap array, we need to implement numerically the Gerchberg-Saxton algorithm presented in the last subsection. For this we first have to discretise the light field, as depicted in Figure 3.3, by describing its complex amplitude $A(x,y)e^{i\varphi(x,y)}$ in the SLM plane by a matrix, of dimension $N_x \times N_y$, with each entry of the matrix standing for the complex amplitude of the light field in a region of size $\Delta_x \times \Delta_y$, giving a total physical size of the discretised light field of $L_x \times L_y = N_x\Delta_x \times N_y\Delta_y$. Likewise, we describe the field in the focal plane by a matrix of the same dimension $N_x \times N_y$, but with different sizes $\tilde{\Delta}_x \times \tilde{\Delta}_y$ of the matrix entries and a total physical size $\tilde{L}_x \times \tilde{L}_y = N_x\tilde{\Delta}_x \times N_y\tilde{\Delta}_y$.

Following the thesis of van Bijnen [2013], we will call $\Delta_x \times \Delta_y$ an *SLM unit* and $\tilde{\Delta}_x \times \tilde{\Delta}_y$ a *focal unit*. They are important dimensions in the numerical treatment of the light field, and are related by

$$\tilde{\Delta}_x \times \tilde{\Delta}_y = \frac{\lambda f}{L_x} \times \frac{\lambda f}{L_y} \tag{3.4}$$

$$\tilde{L}_x \times \tilde{L}_y = \frac{\lambda f}{\Delta_x} \times \frac{\lambda f}{\Delta_y}, \tag{3.5}$$

[1] We initialise the algorithm with an initial random phase φ_{in} of the light field in the SLM plane. The finally obtained phase is thus slightly different for each initial phase.

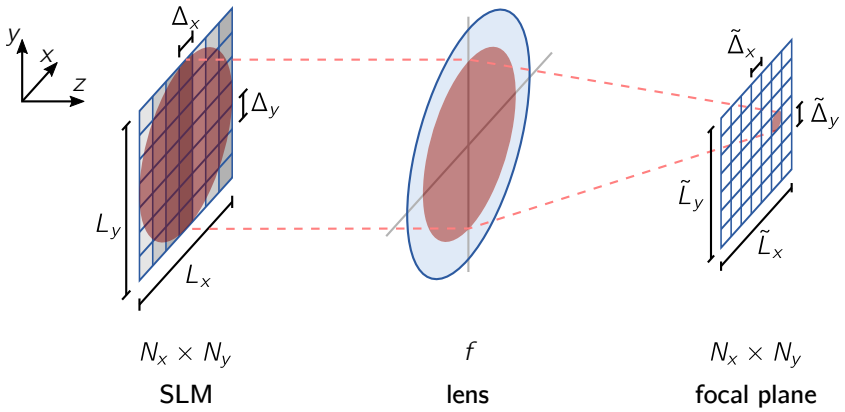

Figure 3.3: Illustration of the spatial dimensions in the SLM and focal plane. When treated numerically, the amplitude $A_{\mathrm{SLM}}(x,y)e^{\varphi(x,y)}$ is described by a $N_x \times N_y$ matrix, with each entry giving the amplitude for a region of size $\Delta_x \times \Delta_y$, so that the entire array has the size $L_x \times L_y = N_x\Delta_x \times N_y\Delta_y$. In the focal plane of a lens with focal length f, the matrix has the same number of entries, but now each entry stands for a region of different physical size $\tilde{\Delta}_x \times \tilde{\Delta}_y$, with $\tilde{\Delta}_{x,y} = \lambda f / L_{x,y}$, λ being the wavelength of the light field.

with λ the wavelength of the light field and f the focal length of the lens.

To understand the effect of the pixelation, we first approximate the continuous light field in the SLM plane as a sum of delta-peaks,

$$A_{\mathrm{SLM}}(x,y) \simeq \sum_{k}^{N_x-1} \sum_{l}^{N_y-1} \delta(x - k\Delta_x)\delta(y - l\Delta_y) A_{\mathrm{in}}(k\Delta_x, l\Delta_y) e^{i\varphi_{kl}}. \tag{3.6}$$

Here A_{in} is the amplitude in the SLM plane, $(k\Delta_x, l\Delta_y)$ the physical coordinates of pixel (k,l) and φ_{kl} the phase delay of that pixel which is imprinted on the incoming light field $A_{\mathrm{in}}(x,y)$. We now propagate the light field by Fourier transforming the above equation according to Equation 3.2. The amplitude of the light field in the focal plane of the lens, on a grid of focal units $\tilde{\Delta}_x, \tilde{\Delta}_y$, is then given by

$$\tilde{A}_{\mathrm{f}}(m\tilde{\Delta}_x, n\tilde{\Delta}_y) = \sum_{k}^{N_x-1} \sum_{l}^{N_y-1} A_{\mathrm{in}}(k\Delta_x, l\Delta_y) e^{i\varphi_{kl}} e^{-2\pi i(km/N_x + ln/N_y)}, \tag{3.7}$$

with $m \in [0, N_x - 1]$ and with $n \in [0, N_y - 1]$. This shows that the amplitudes of the

light fields are related by discrete Fourier transform (DFT):

$$\tilde{A}_{\mathrm{f},nm} = \left[\mathrm{DFT}[A_{\mathrm{SLM}}]\right]_{nm} = \sum_{k}^{N_x-1}\sum_{l}^{N_y-1} A_{\mathrm{SLM},kl} e^{-2\pi i(km/N_x + ln/N_y)}, \tag{3.8}$$

with the amplitude just after the SLM being

$$A_{\mathrm{SLM},kl} := A_{\mathrm{in}}(k\Delta_x, l\Delta_y)e^{i\varphi_{kl}}, \tag{3.9}$$

and the amplitude in the focal plane

$$\tilde{A}_{\mathrm{f},nm} := \tilde{A}_{\mathrm{f}}(m\tilde{\Delta}_x, n\tilde{\Delta}_y). \tag{3.10}$$

We see that the pixel size of the discretised amplitudes are the SLM unit and the focal unit respectively when taking the definition of Equation 3.4. This has two important implications: (i) To increase the accessible region size in the focal plane $\tilde{L}_x \times \tilde{L}_x$, one needs to increase the resolution in the SLM plane, i.e. decrease $\Delta_x \times \Delta_y$ while keeping $L_x \times L_y$ constant. (ii) To increase the spatial resolution in the focal plane, one needs to increase the SLM size $L_x \times L_y$, while keeping its resolution constant.

3.2 Implementation of the SLM in the experiment

In the previous section we saw how it is possible to achieve arbitrary intensity distributions of a Gaussian beam in the focal plane of the lens by only manipulating its phase before focusing the beam with a lens of focal length f. In this section, we will show how we implemented the SLM in our experiment, with the goal of creating arbitrary 2D arrays of microtraps for single-atom trapping.

We use a Hamamatsu X10468-02 liquid crystal on silicon (LCOS) SLM. It has a 792×600 pixel resolution controlled by a computer via an 800×600 DVI signal (in the longer direction, the outer 4 pixels of the signal on each side are not used), with an 8 bit 'dynamic phase range' and a pixel size of $20 \times 20\,\mu\mathrm{m}^2$. The effective size of the SLM chip is $15.8 \times 12\,\mathrm{mm}^2$, with a fill factor of the pixels of 98 %.

The pixel value to achieve a 2π phase shift compared to a pixel value of 0 depends on the wavelength of the light field. For our 850 nm trapping light, a 2π phase shift is achieved with a pixel integer value of 223 (see Figure 3.4(a)). We can thus manipulate the phase with a $2\pi/223$ resolution.

As the SLM diffraction efficiency depends strongly on the polarisation of the incident

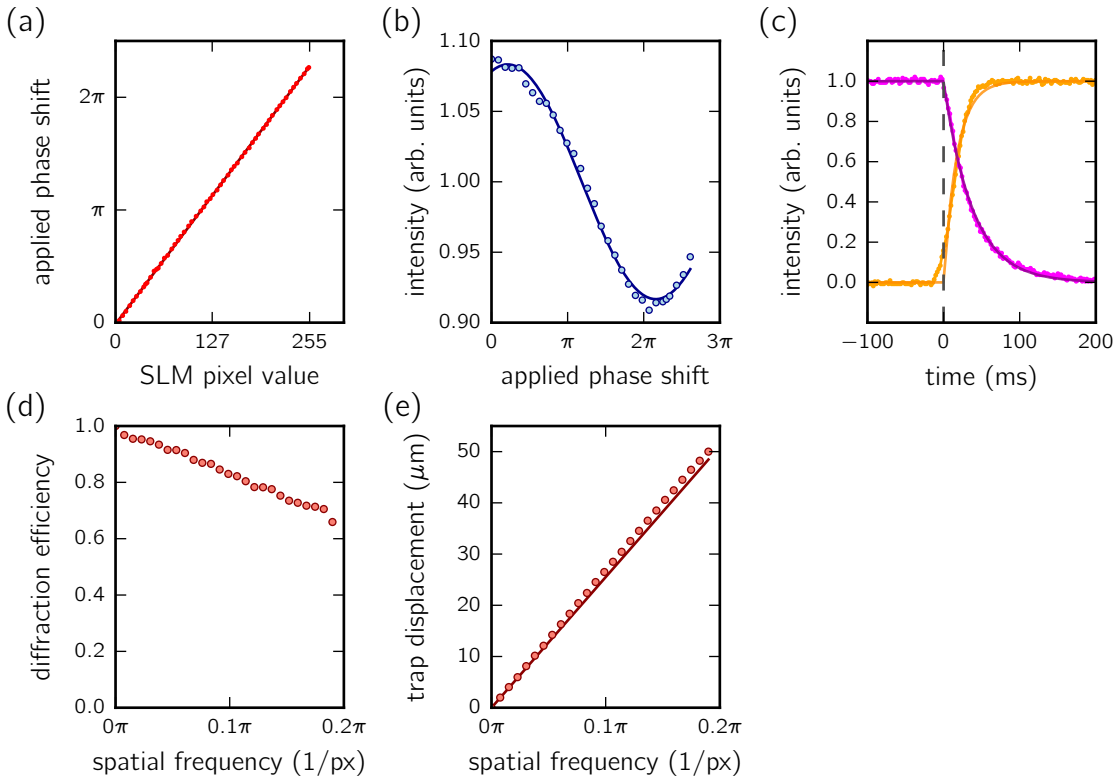

Figure 3.4: Characteristics of our Hamamatsu X10468-02 SLM. (a) The phase shift on the light field as a function of the grey level value displayed on the SLM (data from Hamamatsu). (b) Intensity modulation of a light field with a misaligned polarisation when applying a uniform phase shift on the SLM (the fit gives a $(3.9 \pm 0.1)\pi$ applied phase shift period). (c) Response of the light field when using the SLM to hide ($\tau_{\text{off}} = 37.7\,\text{ms}$) and unhide ($\tau_{\text{on}} = 17.7\,\text{ms}$) the light, by displaying and hiding a blazed grating which moves the sp. (d) Diffraction efficiency of the SLM vs. the spatial frequency of an displayed blazed grating which moves the focus such that it is blocked by an aperture. (e) Displacement of the focal spot as a function of the spatial phase frequency of a displayed blazed grating (points) and the expected displacement (line).

light field, the SLM can act as a waveplate, with a polarisation rotation depending on the displayed phase, thus distorting the polarisation of the diffracted light field. For a misaligned polarisation, the intensity of the diffracted light field measured after a polarisation analyser will thus depend on the phase displayed on the SLM. For an incident light field with slightly misaligned linear polarisation we detect an amplitude modulation of $\pm 10\,\%$, with a period equalling a phase shift of about 4π displayed on the SLM (see Figure 3.4(b)). After proper alignment of the polarisation the amplitude modulation is $< 2\,\%$.

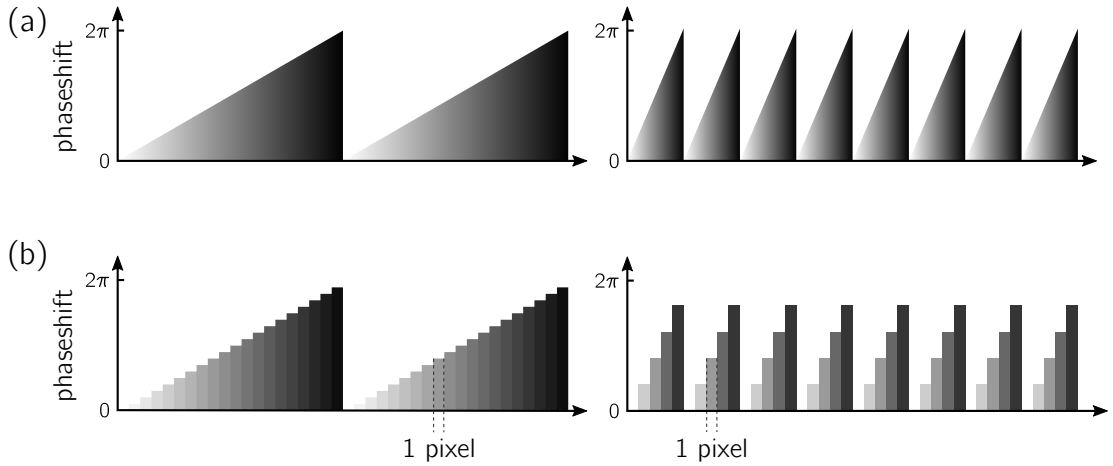

Figure 3.5: Visualisation of the pixelation. (a) A given continuous phase, as the blazed grating here, can only be approximated on the SLM due to the finite size of the SLM pixels. (b) Discretised phase patterns with a low spatial frequency (left) resemble the continuous phase more closely than one with a high spatial frequency (right). The SLM therefore shows a higher diffraction efficiency for low-frequency phase patterns.

The response time of the SLM is limited by the 60 Hz refresh rate of DVI protocol used to control the SLM. To quantify the switching times of the SLM we alternatingly display a blazed grating which displaces the diffracted beam such that it is blocked by an aperture (see Figure 3.6), and another blazed grating grating which lets it pass the aperture. The measured power of the light field right after the aperture is displayed in Figure 3.4(c), showing that the switching times are close to the expected $(60\,\mathrm{Hz})^{-1} = 17\,\mathrm{ms}$ (see Figure 3.4(c)). However, these switching times are far too slow to dynamically change the SLM generated trap pattern during our Rydberg experiments, which have a timescale of a few microseconds.

Finally, we also analyse the effect of the spatial frequency of the displayed phase pattern on the reflected light field, by displaying blazed gratings with different frequencies on the SLM and measuring the diffraction efficiency, shown in Figure 3.4(d-e). The diffraction efficiency decreases with the displayed spatial frequency, because a rapidly-varying continuous phase can no longer be well approximated by the pixelated SLM, as depicted in Figure 3.5. The measured diffraction efficiency decreases roughly linearly with the spatial frequency, being about 66 % for a spatial frequency of $0.1 \times 2\pi$/pixel. For comparison, the typical spatial frequency of a phase pattern to create a 10×10 trap array with a $4\,\mu$m trap spacing is about $0.03 \times 2\pi$/pixel, which would correspond to a diffraction efficiency of still about 90 %.

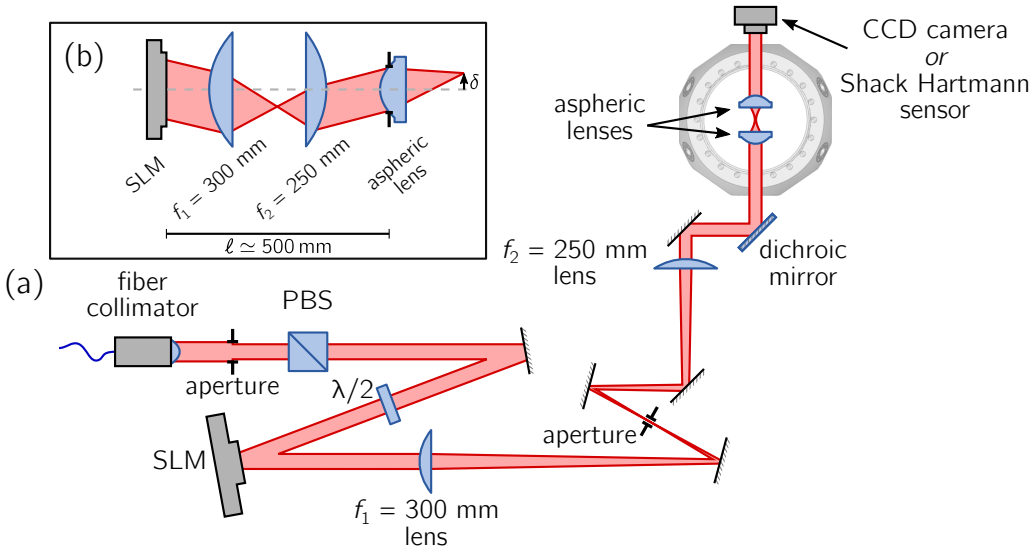

Figure 3.6: Optics setup for the SLM. (a) The Gaussian laser beam, coming from a single mode fiber, is reflected off the SLM, after which it passes through a telescope, reducing the beam from a 6 mm to a 5 mm $1/e^2$-radius. The inset (b) illustrates the use of the telescope, imaging the SLM plane onto the aspheric lens aperture, reducing the effect of clipping on the lens for traps that are not lying on the optical axis (distances not to scale).

3.2.1 Optics setup

The setup of the optics used to manipulate the phase and focus the dipole trap beam in order to create 2D arrays of microtraps is shown in Figure 3.6. For the experiments presented in this thesis we used a Toptica TA Pro diode laser with a tapered amplifier at a wavelength of 850 nm as a light source. By now the laser has been replaced by a Ti:sapphire laser to achieve a higher output power, thus allowing larger number of microtraps in the arrays.

We start out with a beam coming from a single mode, polarisation maintaining optical fiber, with a 6.7 mm $1/e^2$ radius, clipped by a circular iris with a 12 mm diameter to adapt the beam size to the size of the SLM aperture. We then use a polarising beamsplitting cube (PBS) to have a clean polarisation of the beam, and a half-wave plate ($\lambda/2$) to adapt the polarisation of the light field to the SLM, as its diffraction efficiency depends strongly on the polarisation of the incident light field.

After the SLM we use an achromatic telescope with an $m = -10/12$ transverse magnification to adapt the beam size to the $D = 10$ mm aperture of the aspheric lens used to focus the beam in the vacuum chamber. The distances between the SLM and

the telescope and the aspheric lens were chosen such that the telescope conjugates the plane of the SLM with aperture of the aspheric lens, as shown in Figure 3.6(b). This avoids that light which creates off-axis traps is clipped by the aperture of the aspheric lens. For example, due to the relatively long distance between the SLM and the aspheric lens of $\ell \simeq 500\,\mathrm{mm}$, a beam that focuses $\delta = 20\,\mu\mathrm{m}$ off the optical axis would hit the aspheric lens about 1 mm off-axis. In the implementation of the Gerchberg-Saxton algorithm the telescope can be omitted, if we replace the focal length f of the lens by a lens with an effective focal length $f_{\mathrm{eff}} = f/|m| = 12\,\mathrm{mm}$.

An aperture placed in the focus of the telescope allows to block certain parts of a trap array, as well as all the non-diffracted light.

A Zemax calculation, with a flat mirror replacing the SLM, has been performed to check the quality of the optical setup, giving a Strehl ratio, i.e. the calculated peak intensity in the focus of the aspheric lens over the theoretical peak intensity for a diffraction-limited system, of $S \geq 0.88$ over a $20 \times 20\,\mu\mathrm{m}^2$ field in the focal plane.

3.2.2 Numerical implementation

We now describe how we implemented the Gerchberg-Saxton algorithm to calculate phase patterns for the experiment using Matlab, discretising the light field as a matrix, as described in Section 3.1.3. The physical size $\Delta_x \times \Delta_y$ of each entry in the matrix is given by the actual SLM pixel size $\Delta_x = \Delta_y = 20\,\mu\mathrm{m}$. The number of entries in the matrix can be chosen freely, as long as it is larger than the 600×792 pixel resolution of the SLM. Note that calculating fast Fourier transforms (FFTs) is much faster with array sizes of a powers of two [Cooley and Tukey, 1965; MathWorks, 2015].

As the target image, i.e. the desired intensity distribution in the focal plane I_{t} in Figure 3.2, we use an empty matrix, and add traps by setting the pixel which is closest to the trap maximum to a value corresponding to its relative intensity, and normalise the matrix such that the sum of all pixels equals 1. From the calculated $N_x \times N_y$ phase matrix, we take the central 600×792 pixels that correspond to the actual pixels on the SLM, and use this a the phase pattern φ_{array} to be displayed on the SLM.

According to Equation 3.4, taking a matrix with dimension $N_x \times N_y = 2^{10} \times 2^{10} = 1024 \times 1024$ to describe the light field would correspond to a focal unit size of $\tilde{\Delta}_x \times \tilde{\Delta}_y \simeq 0.4 \times 0.4\,\mu\mathrm{m}^2$. We noticed that with such a large focal unit, the spread of distances between the traps in a given trap array, measured on the CCD camera, can be relatively high (see Figure 3.7, left panels). We thus increase the matrix size in the numerical implementation of the Gerchberg-Saxton algorithm to

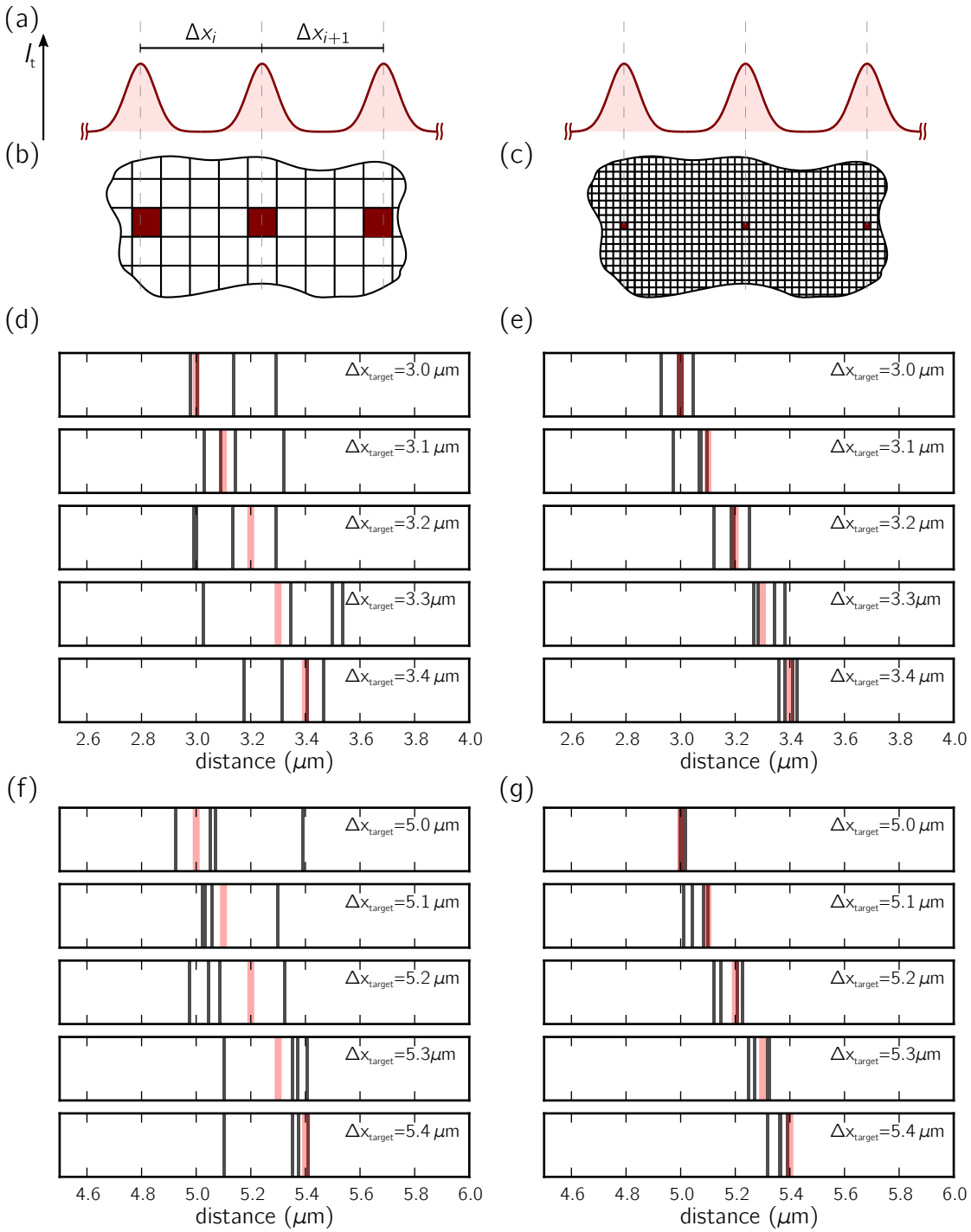

Figure 3.7: Effect of the SLM focal unit size on a 5×1 trap array. (a) We set a 5×1 trap array with equal inter-trap spacings $\Delta x = \Delta x_1 = \Delta x_2 = \Delta x_3 = \Delta x_4$ as the target image. For various target trap-spacings Δx_{target} (light red vertical lines in d-g) we measure the obtained trap spacings (black vertical lines in d-g), with the Gerchberg-Saxton loop run for 40 iterations. We once use a 1024×1024 matrix (b,d,f), and once a 4096×4096 matrix (c,e,g) in the calculation, while keeping the physical size of the matrix entries $\Delta_x \times \Delta_y$ in the SLM plane constant, thus increasing the resolution of the target image by a factor 4, as shown in the sketch in (b,c).

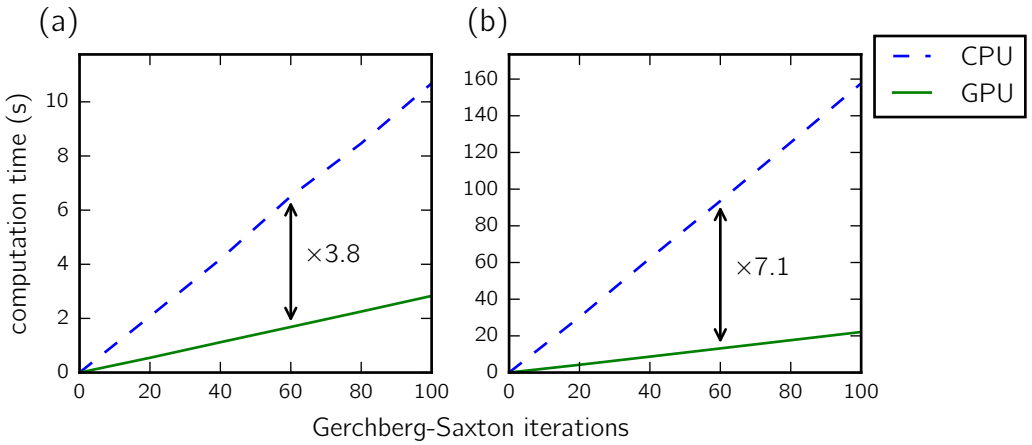

Figure 3.8: Computation times of the Gerchberg-Saxton algorithm. The timings to run the Gerchberg-Saxton algorithm for 100 iterations decrease significantly when running the code on a NVIDIA Quadro K2000 GPU (green lines) instead of an Intel i5 4570 3.20 GHz CPU (blue lines). The increase in calculation speed is even larger for a 4096×4096 matrix size (b) than for a 1024×1024 matrix size (a).

$N_x \times N_y = 2^{12} \times 2^{12} = 4096 \times 4096$ entries, corresponding to a focal unit size of $\tilde{\Delta}_x \times \tilde{\Delta}_y \simeq 0.1 \times 0.1\,\mu\text{m}^2$, With this higher resolution for the target image, the created trap arrays are closer to the given target image, with a smaller distance spread between the individual traps (Figure 3.7, right panels).

The advantage of the increased focal plane resolution due to the larger matrices used in the numerical calculation comes at the cost of an increased computation time, which scales roughly with the number of entries in the matrices, from a few seconds for a $2^{10} \times 2^{10}$ grid to more than a minute for a $2^{12} \times 2^{12}$ grid. To keep the computation time at a feasible length for everyday use in the lab, in particular when using the trap intensity feedback loop (described in Section 3.4), it is possible to run the Gerchberg-Saxton algorithm on a graphics card (GPU), instead of the main processor (CPU). The difference between the two processing units is that CPUs are elaborate general purpose processors, optimised for running linear sets of instructions very fast. GPUs on the other hand contain up to a few thousand simple processing units, and are optimised to perform computations on these units in parallel [Texas Advanced Computing Center, 2010].

As the FFT of a large matrix can be computed very efficiently in parallel, and MATLAB offers a toolbox to conveniently run code on certain graphics cards, we could reduce the computation time for calculating phase arrays by up to a factor

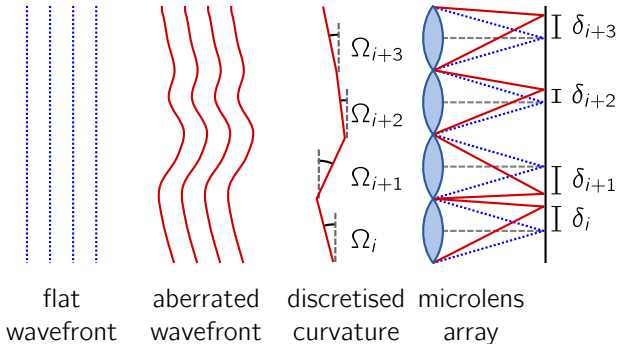

Figure 3.9: Principle of a Shack-Hartmann sensor A Shack-Hartmann sensor consists of a microlens array and a photon sensor (typically a CCD or CMOS chip). For a laser beam with a flat wavefront (blue dotted lines), the foci of the individual microlenses lie on their respective optical axis (grey dashed lines). The wavefront of an aberrated laser beam (red solid lines) can locally be approximated by a plane wave with a tilted wavefront with an angle Ω_i. Each of the foci of the lens array is then displaced by $\delta_i = f\Omega_i$ with respect to the optical axis, f being the focal length of the lenses. One can therefore reconstruct the wavefront by measuring the foci displacements δ_i.

seven when running the calculation on our GPU[2] (see Figure 3.8). The 2 GB memory of the GPU limits us to a maximum matrix size of $2^{12} \times 2^{12}$, which is sufficient for our purposes, as larger matrices do not seem to further improve the quality of the produced trap arrays.

3.3 Aberration correction

Even with a careful implementation of the SLM and the optical components to bring the trapping light to the trapping region inside the vacuum chamber, the trap quality in large trap arrays with a number of traps $N_{\text{traps}} \gtrsim 10$ is no longer satisfactory (see Figure 3.11(c)). This is due to aberrations of the trap beam introduced by the optical components in the setup. These aberrations not only decrease the Strehl ratio of the focused beam, thus decreasing the achievable trap depth for a given laser power. They also invalidate the assumption in the calculation of the phase pattern of having an ideal Gaussian beam with a flat wavefront, thereby reducing the quality of the generated hologram. Especially for large trap arrays, which require more complex phase patterns with higher spatial frequencies, the latter effect becomes critical.

[2]The computer to calculate the phase patterns has an Intel i5 4570 four-core 3.20 GHz CPU and a NVIDIA Quadro K2000 graphics card.

However, as aberrations are solely the deviations of the actual wavefront from the ideal wavefront of a laser beam, we can easily correct for the aberrations using the SLM, as soon as we know the deformation of the wavefront [López-Quesada, Andilla, and Martín-Badosa, 2009].

Correcting the non-flatness SLM chip surface

The most drastic aberration in the optical setup is introduced by the SLM itself. In the calculation of the phase patterns, we consider the SLM as a perfect mirror. Due to the manufacturing process though, its surface is slightly uneven. The SLM manufacturer provided us with a phase pattern (which we will call φ_{factory}, shown in Figure 3.12), which corrects for this non-flatness. The SLM chip surface appears to be slightly curved, with a peak-to-valley deviation of $2.4\,\lambda$, with $\lambda = 850\,\text{nm}$ being the wavelength of our trap laser.

This factory correction phase pattern φ_{factory} is always added to the phase patterns that we display on the SLM.

3.3.1 Correcting the aberrations of the optical components

Additional aberrations can be introduced to the trap beam by the remaining optical components of our setup, whose arrangement is shown in Figure 3.6. In order to measure the aberrations of the beam (with the factory correction phase pattern φ_{factory} already applied), we used a Shack-Hartmann sensor [Platt and Shack, 2001]. Such a device can reconstruct the wavefront of an incident laser beam by using a microlens array and measuring the focus displacement of each microlens due to local tilts of the wavefront (see Figure 3.9 for further explanations). In our case, we used a commercial Imagine Optics HASO4 FIRST Shack-Hartmann sensor, with an aperture of $3.6 \times 4.6\,\text{mm}^2$ and an array of 32×40 lenses.

We analyse the wavefront aberrations by using a single trap, centred on the optical axis of the aspheric lenses. For this the only phase displayed on the SLM is the phase correction pattern φ_{factory} to make up for the non-flatness of the SLM chip, superimposed on a blazed grating φ_{grating} to centre the trap on the optical axis of the aspheric lens pair. We use an $f = 200\,\text{mm}$ achromatic doublet lens between the vacuum chamber and the Shack-Hartmann, to slightly focusing the beam to adapt its size to the aperture of the latter (see sketch in Figure 3.10). The quadratic phase introduced by the lens can be removed from the detected wavefront after the measurement.

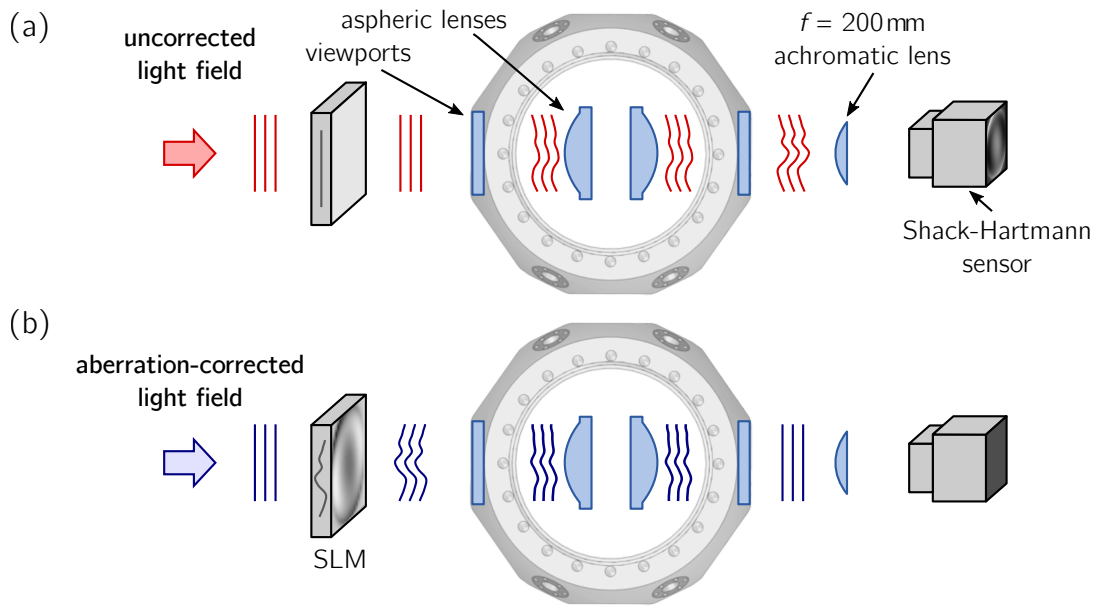

Figure 3.10: Measurement of the aberrations with the Shack-Hartmann sensor. (Note: in this sketch we assume that only the two viewports introduce aberrations) (a) The wavefront of the trap beam was measured with a Shack-Hartmann sensor behind the vacuum chamber, using an $f = 200\,\mathrm{mm}$ doublet to adapt the beam size to the Shack-Hartmann aperture. This measurement may introduce the following error: (b) if significant aberrations are introduced by the second lens or viewport, they are also taken into account when correcting them with the SLM. We might thus *overcorrect* the aberrations at the position of the atoms.

It is convenient to express aberrations in the form of Zernike polynomials [Zernike, 1934; Born *et al.*, 1999], a set of orthogonal functions on the unit disk[3]. The first terms of the Zernike polynomials correspond to aberrations often observed in optical tests, such as astigmatism, coma, etc. By fitting the Zernike polynomials to the measured wavefront, one can therefore deduce the types of aberration present in the optical path by looking at the coefficients of the respective terms. The measured aberrations are shown in Figure 3.11(a) in terms of Zernike coefficients, giving a total rms deviation from a flat wavefront of $\delta_{\mathrm{rms}} = 0.15\,\lambda$. Here we ignore the tilt and focus terms, as they are only introduced by a tilt of the Shack-Hartmann itself and the achromatic lens doublet before the Shack-Hartmann respectively[4]. Figure 3.11(b)

[3] The measured aberrations are discontinuous at the edge of the disk In order to avoid a phase-discontinuity on the SLM, we run a Gaussian filter over the edge of the aberration correction phase pattern, without altering the correction pattern itself.

[4] When using with the Shack-Hartmann without the achromatic doublet lens focus term is indeed negligible.

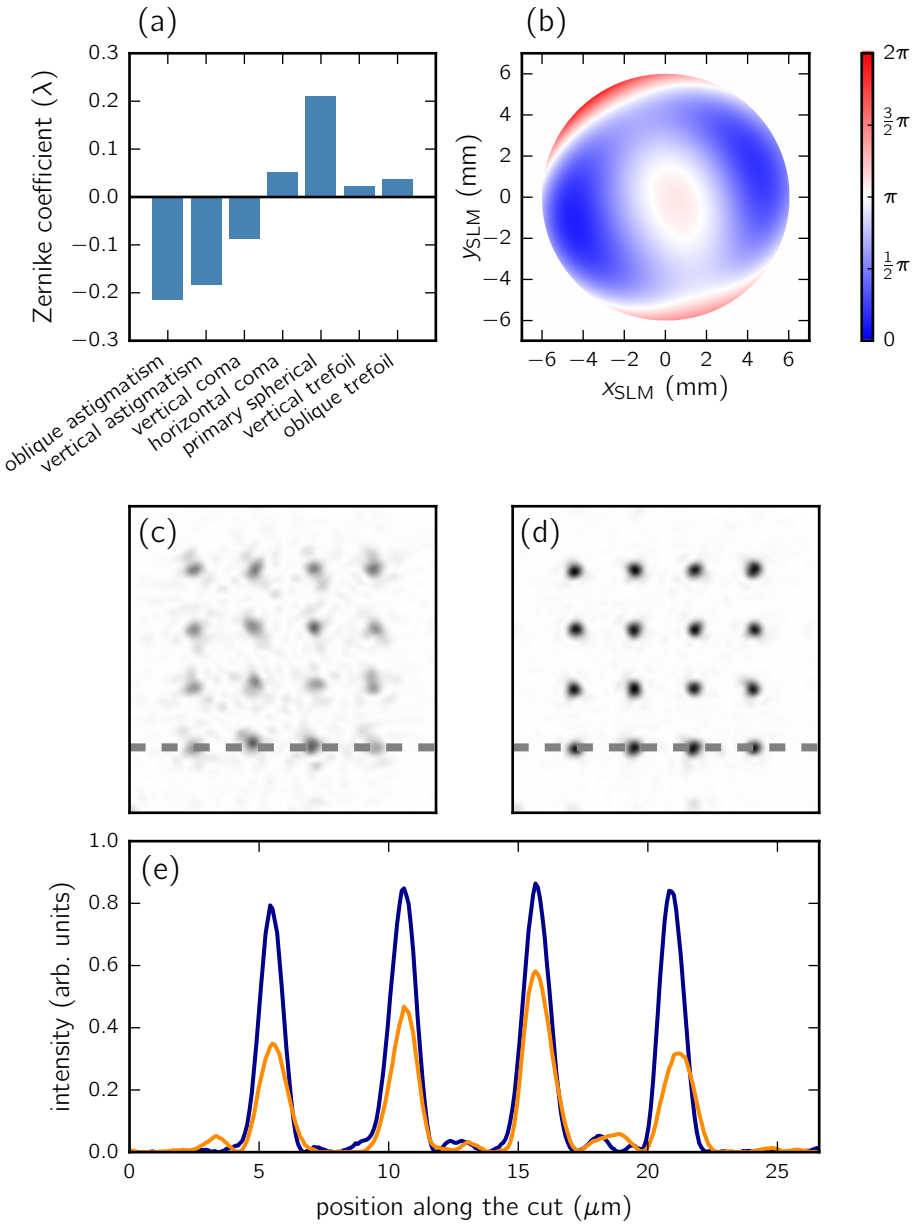

Figure 3.11: Aberration correction with the Shack-Hartmann. (a) The Zernike coefficients of the wavefront of the trap beam as measured with the Shack-Hartmann. Tilt and focus are ignored; higher-order coefficients are not shown, as they are much smaller than the ones that are shown. (b) The aberrations of the trap beam, reconstructed from the Zernike coefficients, with the beam dimension at the SLM. (c,d) Images of a 4×4 trap array taken with a CCD camera placed after the vacuum chamber, without (c) and with (d) the aberration correction phase pattern $\varphi_{\text{aberration}}$ displayed on the SLM. (e) Intensity profile along the bottom row of traps, integrated over a width of 3 pixels, as indicated by the grey dashed lines in (c,d), without (orange) and with (blue) the aberration correction. At the position of the Shack-Hartman, the rms deviation from a flat wavefront is reduced from $\delta_{\text{rms}} = 0.15\,\lambda$ to $\delta_{\text{rms}} = 0.014\,\lambda$.

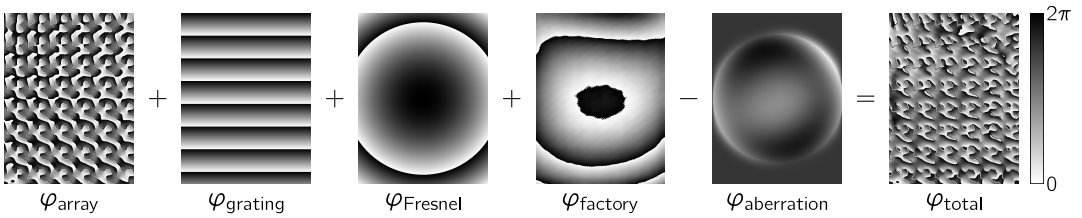

Figure 3.12: Composition of the final phase displayed on the SLM. The combined phase φ_{total} displayed on the SLM is made up of the phase patterns φ_{array} creating the actual array of traps, φ_{grating} and φ_{Fresnel} to move the pattern transversally and longitudinally respectively if needed, φ_{factory} to correct for the non-flatness of the SLM chip, and the measured $\varphi_{\text{aberration}}$ to correct for aberrations introduced by our optical elements. The sum is calculated modulo 2π.

shows the reconstructed wavefront using the Zernike polynomials, for a beam size corresponding to that at the SLM. We see that the main aberrations are astigmatism and spherical aberration, which we attribute to the viewports of the vacuum chamber.

When subtracting the correction pattern (from now on called $\varphi_{\text{aberration}}$) from the phase pattern displayed on the SLM the rms deviation from a flat wavefront after the vacuum chamber is reduced by about a factor ten to $\delta_{\text{rms}} = 0.014\,\lambda$.

Ideally, we would like to correct the aberrations at the position of the atoms, in order to achieve the best trap quality. Unfortunately, we cannot access this position without opening the vacuum chamber and removing the second aspheric lens. We therefore place the Shack-Hartmann sensor and measure the wavefront directly after the beam has passed through the vacuum chamber.

However, correcting the aberrations that we measure *after* the vacuum chamber might *overcorrect* the aberrations at the focus of the aspheric lens, if significant aberrations are introduced by the optical elements after the focus. This is illustrated in the sketch shown in Figure 3.10: the aberration-correction phase pattern displayed on the SLM subtracts the aberrations detected by the Shack-Hartmann from the trap beam. The beam will therefore have a perfectly flat wavefront at the position of the Shack-Hartmann, but may still have aberrations in the focus of the aspheric lens. As we will see later, the aberration correction nevertheless improves the quality of the traps significantly. The final composition of the various phase patterns to create the trap array and correct for the aberrations is depicted in Figure 3.12.

We then replace the Shack-Hartmann sensor with a CCD camera in order to see the effect of subtracting $\varphi_{\text{aberration}}$ from a phase pattern creating a 4×4 trap array. We see that the quality of the trap array increases significantly (see Figure 3.11(c-e)).

When looking at a line profile along a row of the trap array, integrating over a width of 3 pixels, we see that the peak intensity of the traps increases by about a factor 2.

We thus showed that we could significantly reduce the aberrations *after* the vacuum chamber. This does not automatically imply that we actually improved the wavefront at the focus of the aspheric lens. An independent measurement of the wavefront before the vacuum chamber gives $\delta_{\mathrm{rms}} = 0.05\,\lambda$, showing that most of the aberrations are indeed introduced by the vacuum viewports and/or the aspheric lenses. We therefore used a single atom in the central trap of a 3×1 trap array with a $4\,\mu$m spacing, at the focus of the aspheric lens to directly investigate the effect of the aberration correction phase pattern $\varphi_{\mathrm{aberration}}$ on the trap itself by measuring the trap depth and radial frequency of the atom in the trap.

3.3.2 Quantifying the effect of the aberration correction

The two important parameters here to characterise the microtrap are the trap depth U_0 and the frequencies (ω_r, ω_z) with which the atom oscillates in the trap in radial and longitudinal direction respectively. If we approximate the microtrap as an harmonic potential, then these parameters are related by

$$\omega_r = \sqrt{\frac{4\,U_0}{m\,w_0^2}} \qquad \text{and} \qquad \omega_z = \sqrt{\frac{2\,U_0}{m\,z_{\mathrm{R}}^2}}, \tag{3.11}$$

with m the mass of the particle in the trap, w_0 the waist of the trap and $z_{\mathrm{R}} = \pi w_0^2/\lambda$ the Rayleigh length with λ the wavelength of the trapping light.

Measuring the trap depth seen by a single atom

We first measure the depth of the trap as seen by the ^{87}Rb atom. We follow the same procedure as in [Béguin, 2013] which relied on the method introduced in the thesis of G. Reymond [2002]. We make use of the fact that the excited state $\left|5P_{3/2}, F' = 3, m_{F'} = 3\right\rangle$ is only marginally shifted in energy by the trapping light. We can therefore quantify the light shift of the ground state caused by the microtrap by measuring the $\left|5S_{1/2}, F = 2, m_F = 2\right\rangle \rightarrow \left|5P_{3/2}, F' = 3, m_{F'} = 3\right\rangle$ transition frequency [Darquié, 2005; Tey *et al.*, 2008; Shih and Chapman, 2013], as all Zeeman sub-levels of the $5P_{1/2}$ state are shifted equally in energy for our π-polarised trapping light.

To measure the transition frequency, we shine σ^+-polarised probe light on the atom

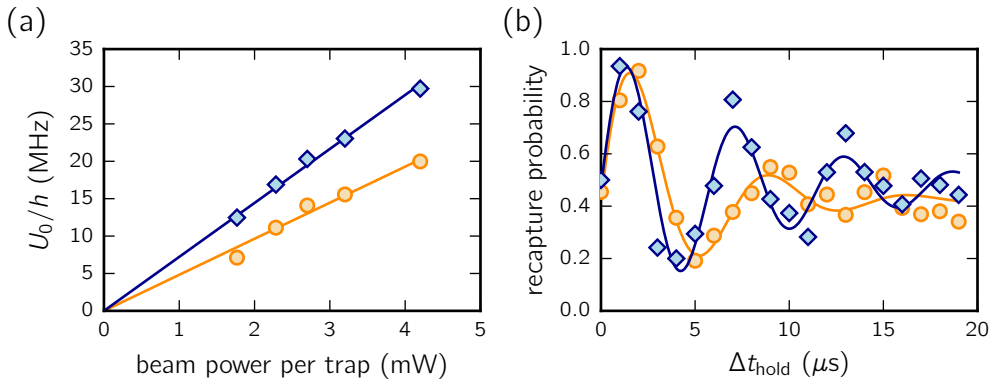

Figure 3.13: Microtrap characterisation with a single atom. We use a single atom trapped in a microtrap to verify that using the aberration correction phase pattern $\varphi_{\text{aberration}}$ (blue diamonds) actually improves the trap quality compared to the uncorrected beam (orange circles) at the focus of the aspheric lens. (a) The trap depth U_0/h as a function of the power in the trap beam. The aberration correction increases the trap depth by $\sim 50\,\%$. The solid lines are linear fits to the data through the origin. (b) We excite the atom to a higher monopole mode of the trap, let the atom oscillate for a variable time Δt_{hold} and measure the recapture probability after having switched the trap off again for a few μs. Solid lines are fits by the empirical function $y0 + Ae^{-\Delta t_{\text{hold}}/\tau}\sin(2\omega_r\,\Delta t_{\text{hold}})$. The trap frequency increases by about 30 % for the aberration corrected trap.

in the microtrap, and record the number of scattered photons as a function of the probe light frequency. The shift of the resonance of the atom in the trap compared to an atom in free space directly gives us the trap depth U_0/h. The measured trap depths are shown in Figure 3.13(a), for different trap beam powers per trap.

When fitting the measured light shifts by a linear function going through the origin, we find

$$\begin{aligned} &\text{uncorrected:} && U_0/P_{\text{trap}} = h \times 4.8\,\frac{\text{MHz}}{\text{mW}} \\ &\text{aberration corrected:} && U_0/P_{\text{trap}} = h \times 7.2\,\frac{\text{MHz}}{\text{mW}}. \end{aligned} \tag{3.12}$$

The trap depth as seen by the single atom thus improves by $\sim 50\,\%$ when correcting for the aberrations.

Measuring the trap oscillation frequencies

The second important trap parameter is the frequency with which the atom oscillates in the trap. The experiment to measure the transverse trap frequency [Reymond *et al.*, 2003] is explained in Figure 3.14 for the one dimensional case. We start the experiment with a single atom in the centre of the microtrap. We switch the trap off for a time

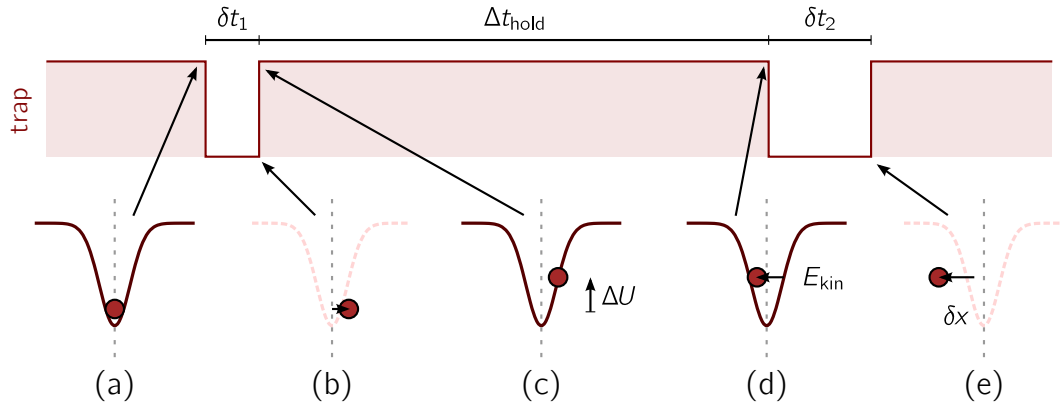

Figure 3.14: Sketch in 1D of the experiment to measure the trap frequency. (a) We start the experiment with a single atom in the microtrap. (b) The trap is turned of for a time $\delta t_1 = 4\,\mu$s. (c) In this time, the atoms moves away from the trap centre due to its finite initial velocity v_0. When the trap is switched on again, the atom gains the potential energy $\Delta U = 1/2 m\omega^2 (v_0\,\delta t_1)^2$ (with ω the trap frequency and m the mass of the atom). (d) We hold the atom for a variable time Δt_{hold} during which the atom will oscillate in the trap. When switching the trap off again, the atom has a kinetic energy $E_{\text{kin}} = (U_0 + \Delta U)\,(1 - \cos(2\omega\,\Delta t_{\text{hold}}))/2$. (e) After having turned the trap off a again for a time $\delta t_2 = 12\,\mu s$, the atom will have moved away from the trap by $\delta x = \sqrt{2E_{\text{kin}}/m} \cdot \delta t_2$. The probability to recapture the atom will thus oscillate with twice the trap frequency ω.

$\delta t_1 = 4\,\mu$s to excite it to a higher monopole mode in the trap. We keep the trap on for a variable time Δt_{hold}, during which the atom will oscillate in the trap. We then probe the kinetic energy of the atom by looking at the probability to lose the atoms after switching the trap off again for a time $\delta t_2 = 12\,\mu$s. The loss probability is related to the kinetic energy, and thus also oscillates with twice the trap frequency ω.

Here we can neglect the longitudinal motion of the atom, since with our trap beam parameters, according to Equation 3.11, the relation between the radial and transversal trap frequency is given by

$$\omega_z = \lambda/(\sqrt{2}\pi w_0) \cdot \omega_r \simeq 0.2\,\omega_{\text{r}}. \tag{3.13}$$

For the chosen time $\delta_1 = 4\,\mu$s, the free expansion along the beam axis thus remains small, and we can assume that we mainly excite a radial oscillation in the trap.

The result of the measurement is shown in Figure 3.13(b). A fit to the data with a

damped sine gives the following radial trap frequencies:

$$\begin{aligned} &\text{uncorrected:} && \omega_r = 2\pi \times 68.0\,\text{kHz} \\ &\text{aberration corrected:} && \omega_r = 2\pi \times 86.5\,\text{kHz} \end{aligned} \tag{3.14}$$

This corresponds to a 30 % increase in the trap frequency, but is still almost 20 % smaller compared to sending the trap beam directly to the aspheric lens without the SLM, as found by Lucas Béguin [2013] on the same setup with a single trap without the SLM. This hints that the more complex setup with the SLM slightly increases the waist of the microtraps.

Together with Equation 3.11 the measured increase in trap depth and frequency shows that the trap waist w_0 does not change when applying the aberration correction. We however significantly increased the diffraction efficiency of the SLM, giving us deeper traps for the same amount of light power, which in turn also increases the trap frequency.

In principle, we could use the single atom measurements as a quality measure to try to improve the trap quality even further, e.g. by using an evolutionary algorithm [Weise, 2009] on the Zernike coefficients. But as every data point in Figure 3.13 takes about 15 minutes to record, such an optimisation would be very time consuming and very sensitive to possible slow drifts of experimental parameters as the excitation beam intensity.

We tried however to use an aberration correction pattern which was constructed using only half of the measured value of each Zernike coefficient, which would be the 'correct' correction if the two viewports would introduce equal aberrations. The result was marginally worse than taking the full value of the measured Zernike coefficients measured with the Shack-Hartmann.

For all the results shown in this thesis from here on, the aberration correction phase pattern is subtracted from the phase displayed on the SLM.

3.4 Feedback for intensity homogeneity

Even when taking care when calculating the phase for a given target intensity distribution, and taking into account the non-flatness of the SLM chip and the aberrations introduced by the optics, the trap depths in the resulting trap array can vary quite significantly from one trap to another, which is detrimental to the experiment. Having traps that are too deep leads to a light shift so large that the

trapped atom is shifted too far off-resonant from the MOT-light, and no longer scatters enough photons to be detected efficiently. In too shallow traps on the other hand it is no longer possible to trap atoms reliably over the duration of the experiment. It is therefore important when creating trap arrays that all the microtraps have very similar trap depths.

As an example we run the Gerchberg-Saxton algorithm for a 10×10 square trap array with a trap spacing of $4\,\mu$m, where all traps have the same target intensity I_t. The resulting trap intensities as measured with the CCD camera are shown in Figure 3.15(b). We measure a rather large dispersion of trap intensities of $\pm 19\,\%$ rms, with the most shallow trap having $61\,\%$ and the deepest trap having $148\,\%$ of the mean intensity of the traps in the array.

The inhomogeneities in the trap depths that we see when measured with a CCD camera after the vacuum chamber (see Figure 3.6) can have various causes:

1. The Gerchberg-Saxton algorithm fails to calculate a phase which gives exactly equal trap intensities.

2. An imperfect diffraction of the light by the calculated phase pattern, e.g. due to remaining aberrations in the optics setup.

Both of the above mentioned points occur in our experiment. The first point we could easily correct for by adapting the target intensity in the numerical calculation of the phase pattern. The second point can also be corrected for by measuring the actual depth of the trap created by a given pattern with the CCD camera behind the vacuum chamber, and adapting the pattern accordingly[5].

We thus equalise the trap intensities measured on the CCD camera in the following way (see Figure 3.15(a)). We run the Gerchberg-Saxton algorithm with the desired trap array as the target intensity, starting out with a random phase in the calculation. After a given number of loops, when the calculation has converged, we pause the algorithm and display the current calculated phase on the SLM. We then measure the trap intensity I_i of each trap i in the image recorded with the CCD camera, and adjust its intensity in the target trap array as

$$I_i^{'} = \frac{\bar{I}}{1 - G\left(1 - I_i/\bar{I}\right)}, \tag{3.15}$$

[5] Again, we could in principle also measure the trap depths by using single atom measurements, but as the measurement of the homogeneity of trap depths would take in the order of 15-20 minutes, the total duration of the optimisation would become intractable in day to day experiments.

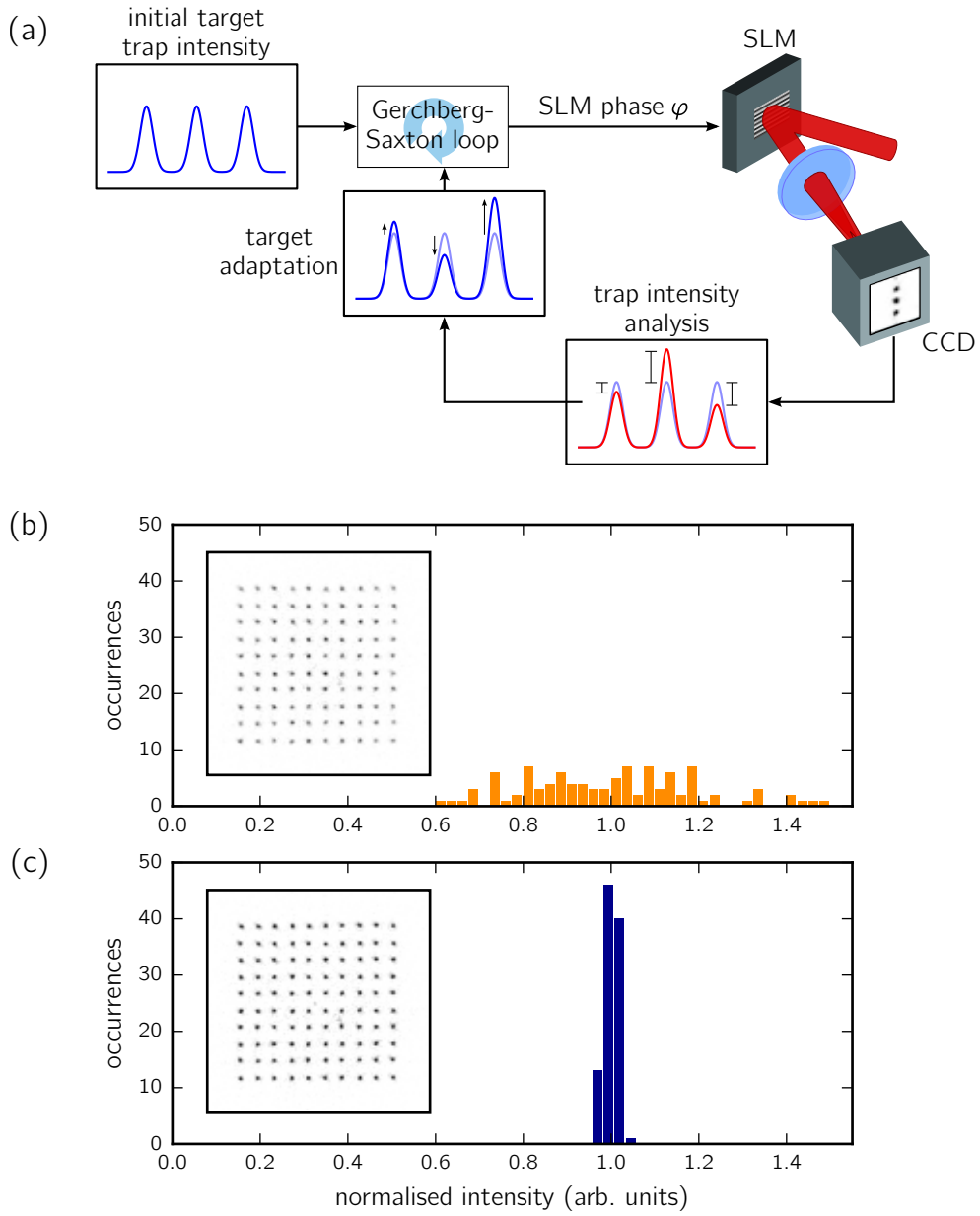

Figure 3.15: Feedback loop for trap intensity homogeneity. (a) For a given target image, we run the Gerchberg-Saxton algorithm, pause it and display the current phase on the SLM. We then analyse the trap intensities from this phase pattern as measured on the CCD camera, and adapt the target trap intensities accordingly, making deep traps shallower and shallow traps more intense in the target image. We then continue the Gerchberg-Saxton algorithm with the updated target image. We repeat the intensity feedback until the coefficient of variation of trap intensities has reached a satisfying level ($\sim 2\,\%$), typically after 5-10 feedback iterations. (b) The array after running the Gerchberg-Saxton algorithm once. The histogram shows that the intensities as measured on the CCD camera have a large spread, with a standard deviation of $19\,\%$ of the mean. (c) The same array, this time using the intensity feedback in the Gerchberg-Saxton. The standard deviation of the trap intensities is reduced to $1.4\,\%$. The insets show the respective images recorded with the CCD camera.

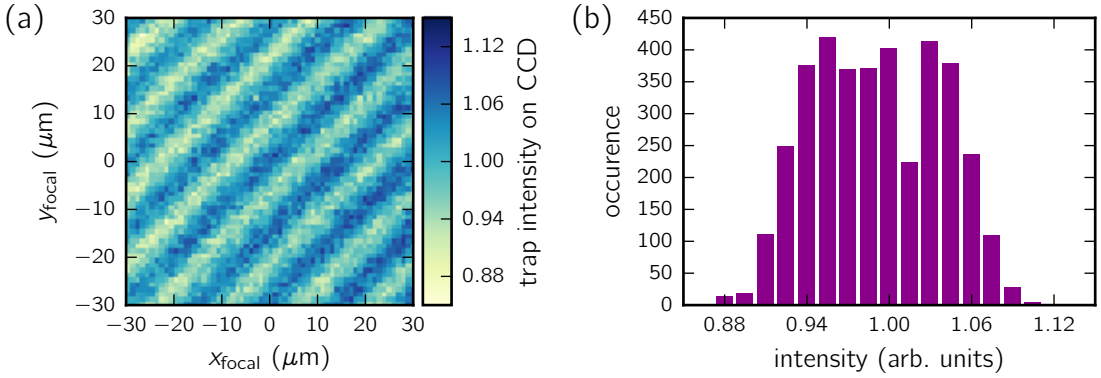

Figure 3.16: Intensity variations on the trap-imaging CCD camera. (a) Intensity of a single microtrap with constant power as measured on the CCD camera, scanned in steps of 1 μm in an area of $60 \times 60\,\mu\text{m}^2$ in the focal plane of the aspheric lens. We see intensity fringes with a period of about 10 μm and an rms around the mean of 5 %. (b) Histogram of the measured trap intensities in (a).

where $\bar{I}$ is the mean intensity of all traps in the CCD image and G and adjustable gain factor in the feedback. This means that traps that are too weak get enhanced in the target image, while traps that are too deep get dimmed, proportionally to their ratio with the mean of the trap intensities. We then continue the Gerchberg-Saxton algorithm with the updated target image[6]. The entire process of taking an image with the CCD camera, measuring all individual trap depths, and adjusting the respective trap intensities in the phase calculation, is done in an automated way by a computer.

After typically ~ 5 intensity feedback iterations the standard deviation of the trap intensities is reduced significantly to $\sim 1\,\%$, with the fastest improvement typically achieved with $G \simeq 0.7$. A larger gain overshoots the correction, leading to oscillations of the trap intensities with the trap feedback iterations, while a smaller gain increases the convergence time. Figure 3.15(c) again shows the 10×10 trap array, this time after having run the Gerchberg-Saxton including 20 intensity feedback iterations. The standard deviation could be reduced to 1.4 %, with the most shallow trap now having 96 % and the deepest trap having 103 % of the mean trap depth.

We recently became aware of spatial variation of the light intensity measured on the CCD camera, which results in a spatial variations of the measured trap depths, even for a a homogeneous trap array. The spatial intensity dependence of our CCD camera[7]

[6] After the implementation of the intensity feedback loop we realised that a similar technique was already discussed in [Matsumoto *et al.*, 2012].

[7] We use a The Imaging Source DMK 41BU02 monochrome industrial CCD camera with 8 bit A/D dynamic range.

is shown in Figure 3.16(a). We scan a single microtrap with constant total power in the transversal plane around the optical axis of the aspheric lens, and measure its intensity on the CCD camera. We see an oscillating intensity variation of the microtrap, with a period of about 10 μm and an rms about the mean of about 5 % (see Figure 3.16(b)). The origin of these intensity variations is most likely due to an internal interference of the trap beam in the microlens array in front of the CCD chip (personal communication, The Imaging Source, 10/07/2015). However, the 5 % intensity variations only slightly broaden the detected distribution of trap depths of Figure 3.15(b).

All the results presented in this chapter, the careful implementation of the SLM in the setup, the aberration correction and the feedback loop for homogeneous trap intensities were crucial to achieve high quality trap arrays with $\gtrsim 5$ traps for experiments presented in the following Chapters of this thesis.

3.5 Gallery of trap arrays

With the methods described in this chapter, one can arrange single neutral atoms in arbitrary geometries, and change the order with a simple click of the mouse on the computer. We are able to generate trap arrays with spacings as low a 3 μm, containing up to ~ 100 traps[8].

Figure 3.5 shows a selection of traps arrays that we are able to generate in the lab. We can simply arrange the atoms in one-dimensional chains, which we have used in [Barredo *et al.*, 2015], or in a ring (Figure 3.5(b)), realising a quasi-one-dimensional system with periodic boundary conditions, to study transport [Heidrich-Meisner, Honecker, and Brenig, 2007], thermalisation [Olmos, Müller, and Lesanovsky, 2010], or phase transitions [Mattioli, Glätzle, and Lechner, 2015] in one-dimensional systems.

For experiments in 2D, we can generate large non-trivial lattices, from square to triangular (Figure 3.5(d)), to hexagonal, kagome (3.5(e)) and 'squagome' (3.5(f)) lattices, e.g. to study the physics of graphene [Castro Neto *et al.*, 2009] and phenomena as frustration [Santos *et al.*, 2004; Glaetzle *et al.*, 2014] and topological spin liquids [Yan, Huse, and White, 2011; Peter *et al.*, 2015; Yao *et al.*, 2015].

It is even possible to put the atoms in aperiodic or completely random positions (Figure 3.5(c,g)), something that is intrinsically non-trivial for optical lattices [Weitenberg *et al.*, 2011], potentially allowing the study of phenomena as many-body

[8] The number of traps is limited by the total light power that can be sent on the SLM, and the field of view of the aspheric lens.

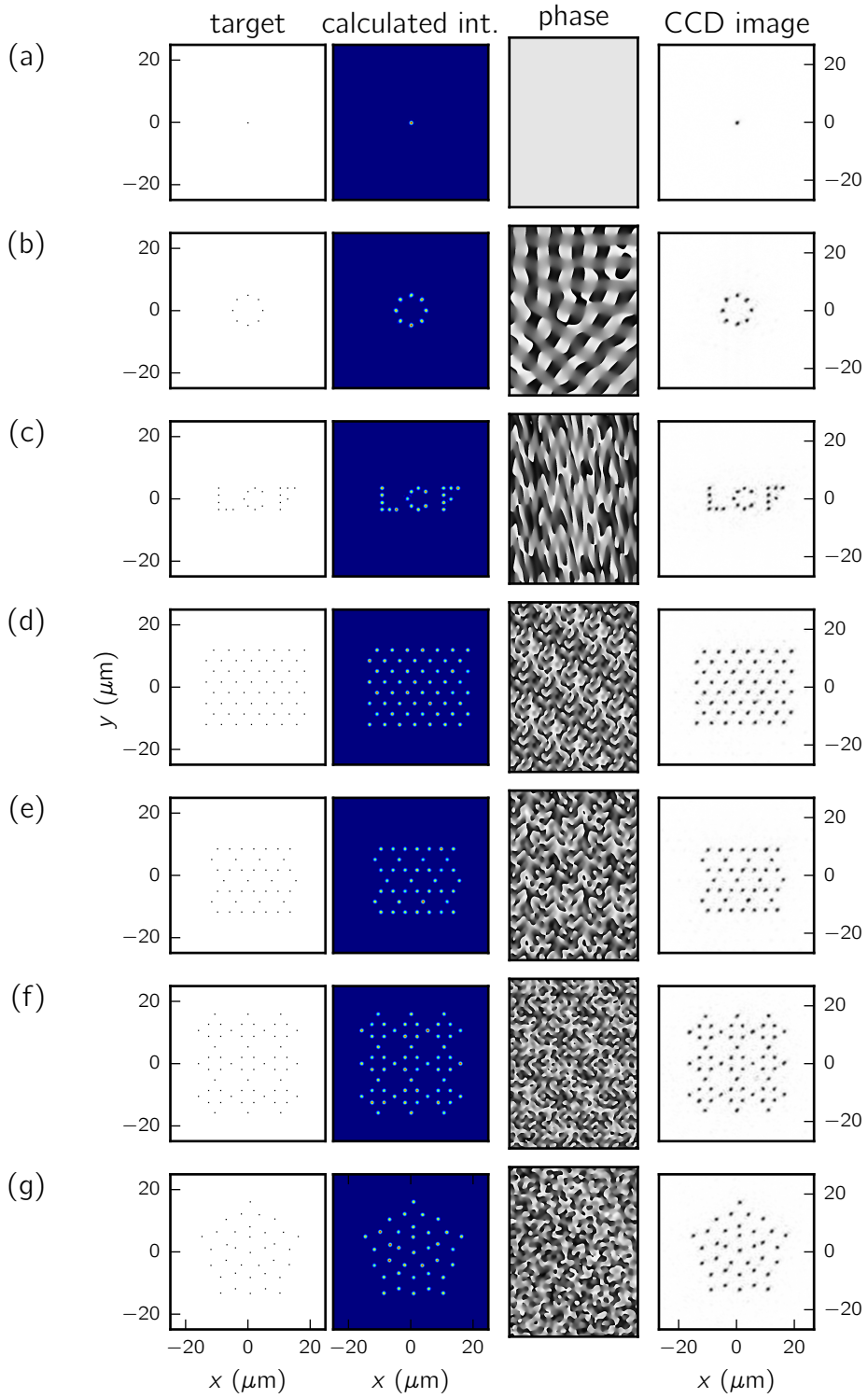

Figure 3.17: Examples of generated trap patterns. From left to right: the target pattern used as I_t in the Gerchberg-Saxton algorithm, the calculated intensity of the light field in the focal plane, the obtained phase pattern, and the trap intensities as measured with the CCD camera. (a) single trap, (b) circle of 8 traps, (c) arbitrary arrangement, (d) triangular lattice, (e) kagome lattice, (f) 'squagome' lattice, (g) quasi-periodic (Penrose) pattern.

localisation [Anderson, 1958; Hauke and Heyl, 2015] and transport in disordered networks [Bässler, 1993; Scholak *et al.*, 2011].

3.6 Conclusion

We have shown how we use a spatial light modulator to shape the spatial phase of our optical dipole trap beam to 'clone' the single microtrap. Using this technique, we are able to create arbitrary 2D geometries of up to ~ 100 single atoms traps, with trap spacings as low as $3\,\mu$m, and array sizes up to $\sim 50 \times 50\,\mu\text{m}^2$. We calculate an appropriate phase pattern for a given trap arrangement using the Gerchberg-Saxton algorithm. In order to create high-quality trap array, we have measured the aberrations in the dipole trap beam, and correct for them using the SLM. In order to create traps of equal depth, we employ a feedback which measures the depths of the traps, and automatically corrects the target intensity in the Gerchberg-Saxton algorithm.

Chapter 4

Spatially resolved state detection and manipulation in arrays of single atoms

In the previous chapter we have seen how we can create arbitrary arrays of microtraps by manipulating the spatial phase of a single trap beam using a Spatial Light Modulator. In this chapter we will see how we detect the state of the atoms by recording their scattered photons, spatially resolving each individual atom, on a CCD camera.

Furthermore, we demonstrate our ability to locally address an arbitrary site in the array to block or uniquely enable the Rydberg excitation of the addressed atom, and how we can use this addressing capability to manipulate the phase of an entangled two-atom state.

4.1 Determination of the state of the atoms in the microtraps

The reliable determination of the state of the atoms is crucial for our experiments. Before launching an experimental sequence, we need to continuously monitor the state of the microtraps of a given array, in order to launch an experiment as soon as a certain trigger condition is fulfilled, e.g. having a minimum number of loaded traps. In addition, at the end of a sequence, we need to detect whether a given atom has been excited to a Rydberg state or not. In this section, we present the simple but efficient detection method that we use in the experiment to achieve this.

4.1.1 Detection of the atomic fluorescence

We detect the presence of an atom in a given microtrap by measuring the scattered light from the 780 nm MOT cooling beams at the position of the traps. We collect the light via the same aspheric lens which focuses the trap beam (see Figure 4.1), separating it from the trap light with a dichroic mirror. We then image the trap plane

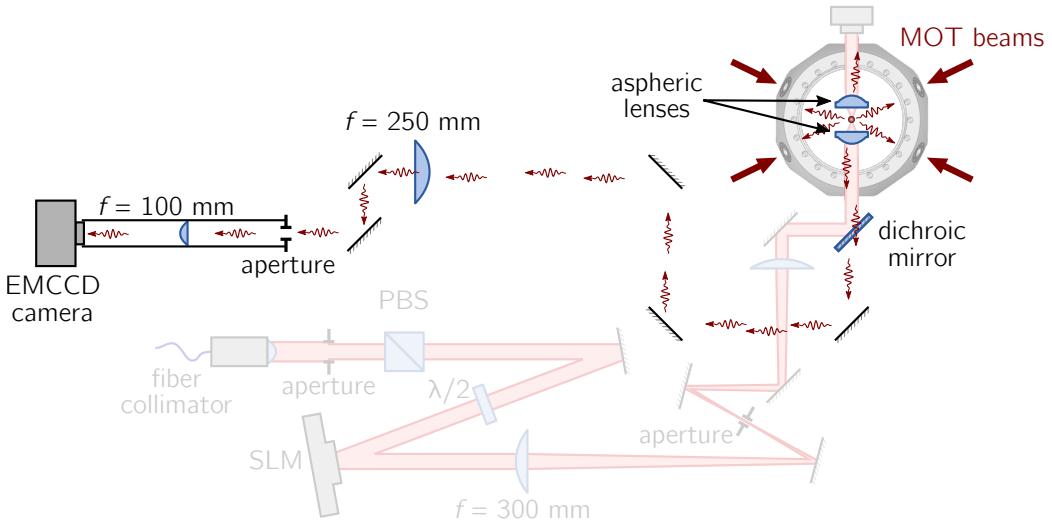

Figure 4.1: Overview of the single atom imaging system. We collect the MOT cooling light scattered by the atoms via the same aspheric lens which focuses the trap beam. A dichroic mirror separates the fluorescence light from the trap light. An $f = 250\,\mathrm{mm}$ lens focuses the light at an aperture which reduces slightly the depth of field, and a second $f = 100\,\mathrm{mm}$ lens images the atoms on the EMCCD chip, with total magnification of 16. The pixel separation of the EMCCD camera corresponds to $1\,\mu\mathrm{m}$ in the trap plane due to the magnification.

on a 16 bit electron multiplying CCD (EMCCD) camera[1], thermoelectrically cooled to $-80\,^{\circ}\mathrm{C}$ in order to reduce the noise on the chip. We currently do not use the electron multiplying mode, as the photon yield from the single atoms at the EMCCD camera is high enough at about 6 photons/ms, detecting about 2 % of photons scattered by an atom (see [Béguin, 2013] for an estimate of the detection efficiency).

The EMCCD camera has a 512×512 pixel resolution, with a pixel size of $16 \times 16\,\mu\mathrm{m}^2$. We calibrated the magnification of the imaging system to be 16, meaning that every pixel images a $1 \times 1\,\mu\mathrm{m}^2$ area in the trap plane. The fluorescence of each atom thus impinges on an area between 1×1 and 2×2 pixel, depending on whether it falls in the centre or on the edge of a pixel.

For all of the experiments presented in this thesis, we used the following parameters for the EMCCD camera. In order to increase the readout speed of the camera we used a 100×100 pixel subset of the CCD chip, and set the exposure time to 50 ms, giving us about 12 frames per second (fps), which we found to be a good trade-off between a high signal-to-noise ratio of the single atom signal and a high frame rate. A

[1] We use a Andor iXon Ultra 897 camera.

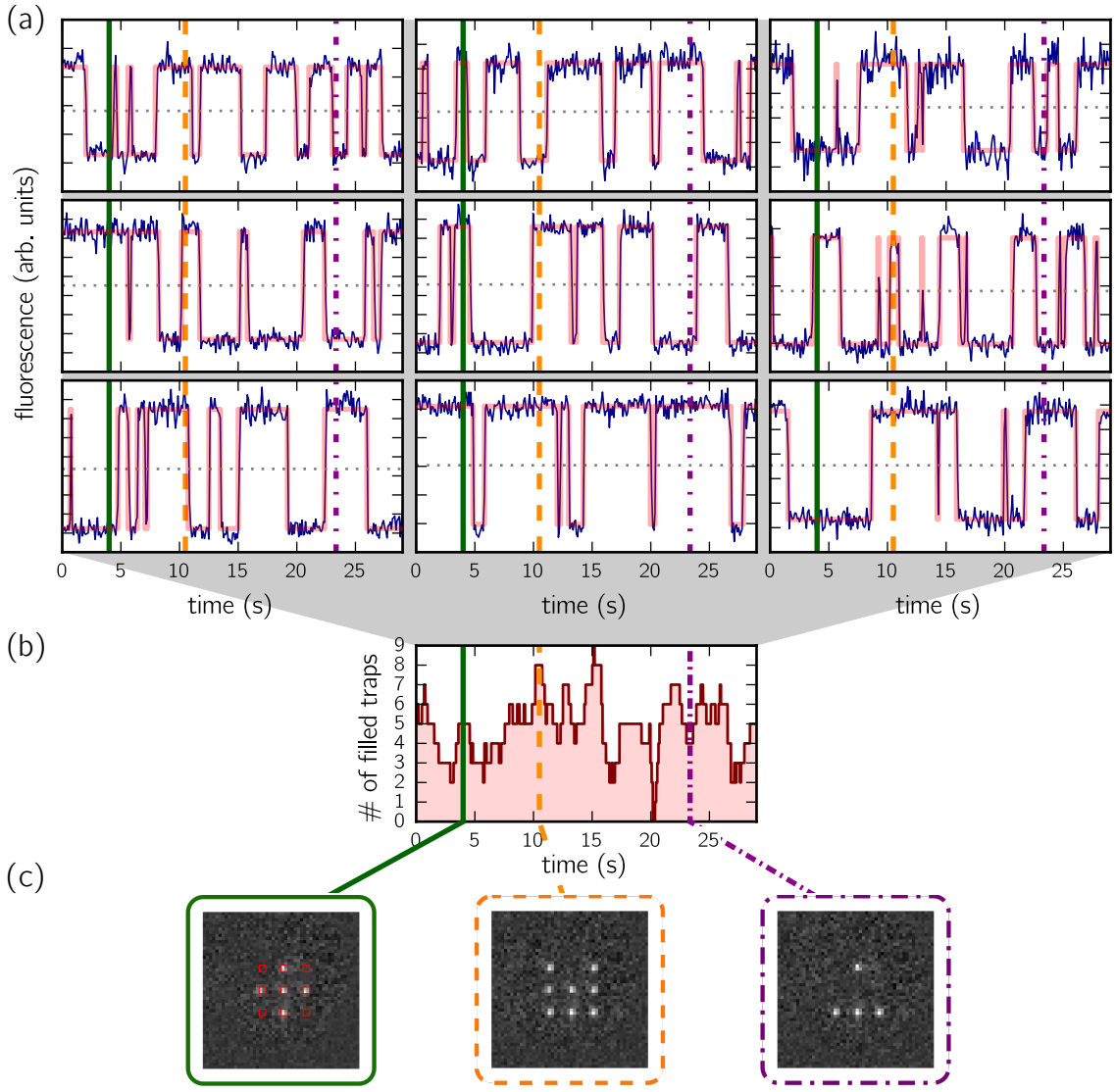

Figure 4.2: Fluorescence signal of atoms in a 3 × 3 trap array. (a) We monitor the mean fluorescence levels of the pixels indicated by the red squares in the frame in the bottom left during a 50 ms exposure, taking a frame about every 100 ms. For each trap, we see the typical telegraph-like fluorescence signal, with the low and high levels corresponding to 0 and 1 atoms in the trap respectively. We define a threshold (horizontal grey dashed lines) separating the two states, in order to create a binary signal (red curves on top of the fluorescence signal). (b) Number of filled traps obtained from the fluorescence traces. (c) Frames from the CCD camera taken at the times indicated by the green, orange and purple line respectively.

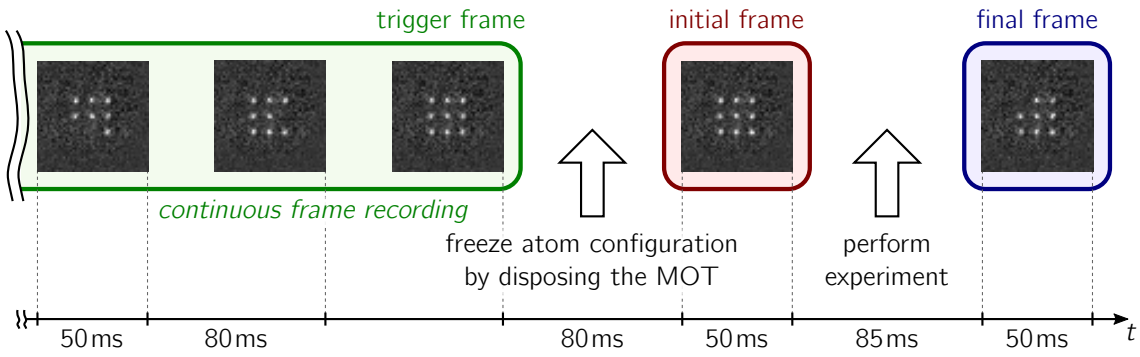

Figure 4.3: Timings of the EMCCD camera frames. We continuously record the fluorescence of the atoms on the EMCCD camera. When a predefined trigger condition is fulfilled, in this example the presence of 9 atoms in a 3×3 trap array, the configuration is frozen by turning of the MOT, thus stopping the loading process of the traps. We record another frame to get the initial atom configuration, perform a given experiment, e.g. a Rydberg excitation, and lastly record the final frame to see which atoms were lost during the experiment. The delays between the *trigger*, *initial* and *final* frames are set by the experimental sequence.

high frame rate is desirable, as we want to quickly launch an experiment once a given triggering condition has been fulfilled, before one of the traps loses its atoms again.

To display and analyse the detected atomic fluorescence on a computer, we developed a custom software based on the Python library pyqtgraph[2]. It allows the real time display of the frames captured by the EMCCD camera, and automatically checks for the presence of atoms in predefined regions of interest (ROIs). The typical fluorescence signals for nine ROIs placed at the trap positions in a 3×3 trap array are shown in Figure 4.2. For each fluorescence signal we define a threshold which we use to binarise the signal to having either zero or one atom in the trap. The Python program continuously analyses the traces and can trigger an experiment once a pre-chosen condition, e.g. a minimum number of filled traps, is fulfilled (see Figure 4.3).

We then remove the MOT atoms by switching off the MOT cooling beams for $\sim 40\,\mathrm{ms}$. The loading process of the microtraps is therefore frozen. Without the MOT around, the lifetime of an atom in a microtrap was measured to be $\tau_{1\mathrm{at}} \approx 10\,\mathrm{s}$. The lifetime of any given configuration in an N trap array is thus $\tau_{N\mathrm{at}} = \tau_{1\mathrm{at}}/N$.

Before we perform the actual experiment with the single atoms, we acquire an *initial frame*, giving us the initial atom configuration. It is not sufficient to just take

[2] pyqtgraph is a pure-python graphics and GUI library built on PyQt4 / PySide and numpy, aimed at fast data visualisation, distributed under the MIT open-source license.

the triggering frame for the initial atom configuration, as there is a finite probability for the atom configuration to change while disposing of the MOT. For the 3×3 array taken as an example here, in about 50 % of the experiments at least one of the atoms is lost between the triggering and the initial frame for trap loading rates of $R_{\mathrm{load}} \approx 1\,\mathrm{atom/s}$. Of these 50 % 'failed triggers', 10 % are accounted for by the finite vacuum lifetime of the configuration. The remaining 40 % are accounted for by the 35 ms dead time between the end of the *trigger* frame exposure and the launch of an experimental sequence, and the $\sim 20\,\mathrm{ms}$ to remove the MOT atoms.

We then record the *final frame* after having performed an experiment, from which we see which atoms were lost during the experiment. As will be shown later, this allows us to determine the internal state of each single atom individually, whether it was in the ground or Rydberg state.

We typically see a background on the single atom signal on the EMCCD camera, which is about 3 to 5 times larger than the fluorescence from a single atom. This background is due to MOT cooling light being scattered off components inside the vacuum chamber. The intensity of this speckle field varies in time on each pixel on the EMCCD camera. In order to still be able to define a threshold to automatically detect the presence of an atom in the trap, we 'shake' the pointing direction of five of the MOT beams with a few hundred Hz, by placing piezoelectric actuators underneath one of the mirrors of each of the five beams. This drastically improved the stability of the background on each pixel of the EMCCD camera, without leading to any noticeable increase of temperature for the trapped single atoms.

For any remaining fluctuations of the background, the Python program recording the camera frames can automatically adjust the threshold along with the background fluctuations in a very reliable way, by monitoring the average 'high' and 'low' values of the atomic fluorescence.

4.1.2 Loading statistics

The physics behind our single atom trapping was already briefly explained in Section 2.2.2. If a trap is empty, an atom can enter at any random time and stay in the trap, where it is continuously cooled by the MOT light. If an atom enters into an already filled trap, the two atoms will undergo a fast inelastic light assisted collision and will both be expelled from the trap [Schlosser *et al.*, 2001].

Since these two processes, loading an atom into the trap and removing the atom from the trap, rely on the same cause, namely an atom entering the trap, the expected

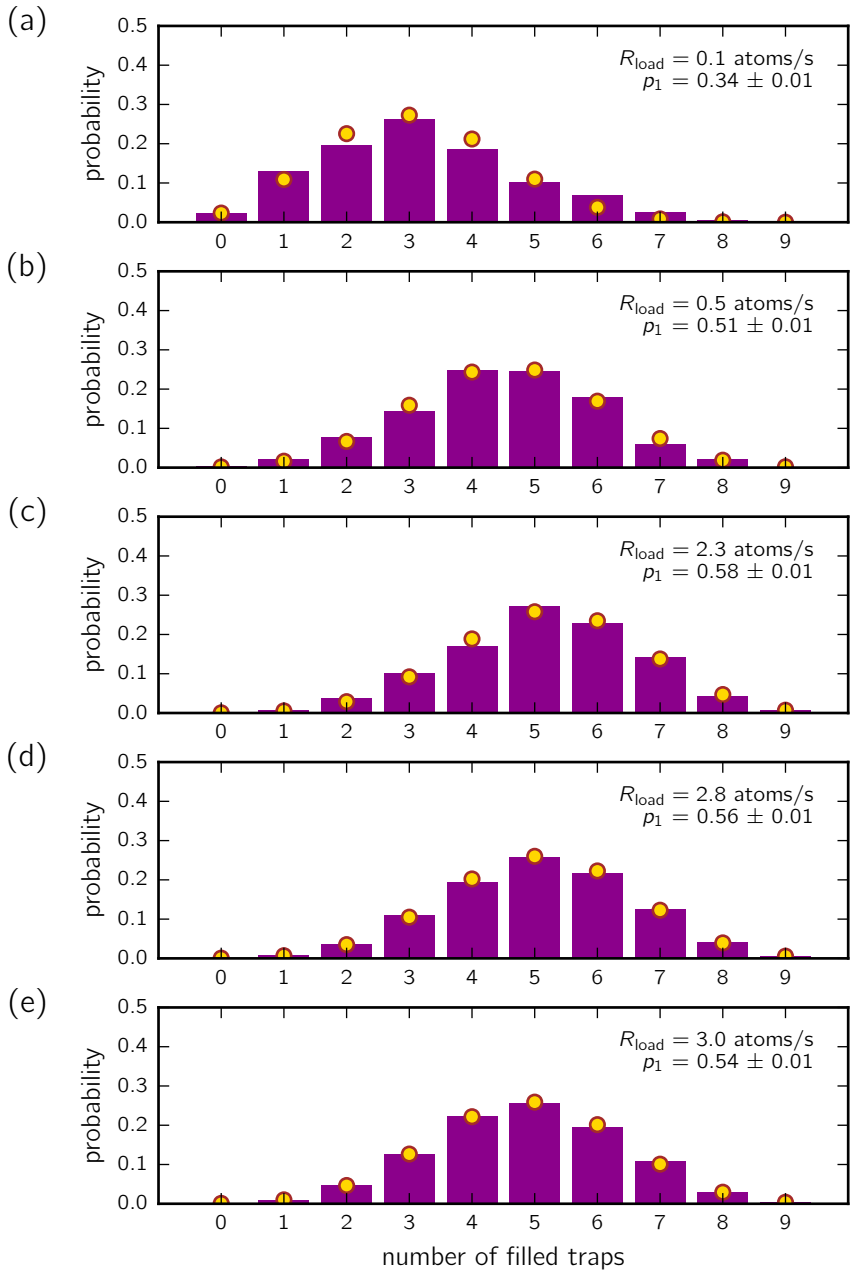

Figure 4.4: Counting statistics of filled traps in a 3 × 3 trap array. We measure the distribution of the number of filled traps for an array of nine traps for different rates R_{load} to load atoms into the trap (purple bars). We fit the distributions by a binomial distribution to get the occupation probability p of the traps (yellow points). The occupation probability saturates slightly above $p_1 = 0.5$ for loading rates $R_{load} \gtrsim 0.5$ atoms/s.

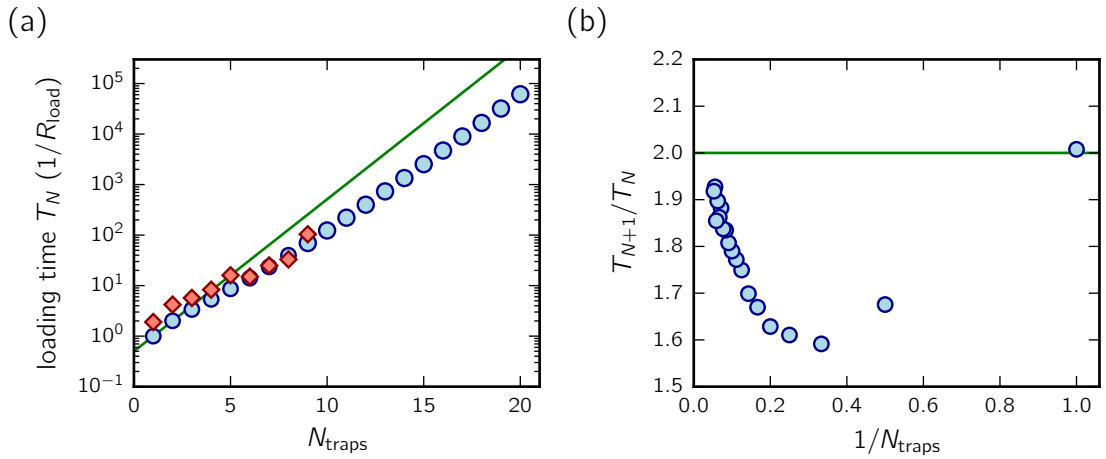

Figure 4.5: Times needed to completely fill an N-trap array. (a) Measured (red squares) and simulated (blue circles) average times T_N to fill an N trap array, in inverse trap loading rate R_{load}. The data is the result of a Monte-Carlo simulation. The green line shows the function $T_N = T_1 2^{N_{\mathrm{traps}}-1}$. (b) Same simulated data as in (a), shown as the ratio of loading times versus the inverse of the trap number, to find the large-N scaling of the loading times. For large trap numbers, the scaling goes towards $T_N \approx 2^{N_{\mathrm{traps}}}/R_{\mathrm{load}}$.

probability to find an atom in the trap at a given time is 50 %, if there were no other loss mechanism present.

Analysing the mean single atom occupation probability p_1 for 3×3 trap array, we find that above a loading rate of $R_{\mathrm{load}} \gtrsim 0.5\,\mathrm{atoms/s}$ into the microtrap we indeed find $p \simeq 0.5$ (see Figure 4.4). For very low loading rates the single-atom loss, e.g. due to background gas collisions, is non-negligible, whereas for high loading rates a occupation probability larger than $p_1 = 0.5$ is prevented by the high two-body loss rate [Schlosser, Reymond, and Grangier, 2002]. The loading rate itself was determined by taking the rate with which the trap state changes, thus ignoring other sources of atom loss as the $R_{\mathrm{loss}}^{(\mathrm{vac})} \simeq 0.1\,\mathrm{s}^{-1}$ vacuum loss rate. Further increasing the loading rate R_{load} to be larger than the light-assisted-collision rate $\beta'^{-1} \approx 1\,\mathrm{ms}$ [Fuhrmanek *et al.*, 2012] would lead to having more than one atom per trap on. Nevertheless, as our imaging scheme uses the same MOT beams that are responsible for the light assisted collisions, it will act as a parity projection of the atom number, again leaving on average half of the microtraps filled with a single atom.

The fact that we actually see occupation probabilities slightly larger than 0.5 can be explained by a finite probability $p_{2\to1}$ that when two atoms undergo a light-assisted collision in the microtrap, only one is expelled and the other one remains in the trap. It is even possible to significantly increase this probability $p_{2\to1}$ to dominate over the

two-body loss probability $p_{2\to 0}$ by carefully choosing the frequency and power of the 'collisional beam' of Figure 2.2. Occupation probabilities of up to 90 % have been achieved this way [Fung and Andersen, 2015; Lester *et al.*, 2015]. Very recently, a first preliminary test of this technique on our experiment gave occupation probabilities of $p_1 \gtrsim 80\,\%$.

With a single atom occupation probability of $p_1 \simeq 50\,\%$ we are limited to either work with trap arrays which are only partially loaded, or to work with small trap arrays and wait until all traps are occupied by a single atom at the same time.

For the latter, we measured the time to fully charge an array with N_{traps} traps both in the experiment and by doing a Monte-Carlo simulation (Figure 4.5(a)). On the experiment, waiting for a fully charged array is feasible only for up to $\simeq 9$ traps. For 9 traps the time to fully load the array is already about one minute for $R_{\text{load}} \simeq 1\,\text{atom/s}$. For higher trap numbers this rapidly increases to several minutes, rendering the total duration even of a simple experiment challenging. Even with higher loading rates this time cannot be much improved, as then the lifetime of a given atom configuration gets too short, and the probability to have the same atom configuration in the trigger and the initial frame (see Figure 4.3) gets too low.

For the Monte-Carlo simulation of the trap loading times, we start with an empty trap array. During each time step δt we add an atom to each trap with a probability $\delta t \cdot R_{\text{load}}$. If a trap contains more than one atom, it is reset to zero. We then measure the time until all traps are filled at the same time. We average on 10 000 runs, with $\delta t = 0.01$ and $R_{\text{load}} = 1$, for arrays between 1 and 20 traps.

We see a N_{traps}^{η} power-law scaling, with $\eta \approx 2$ when extrapolating to large trap numbers (see Figure 4.5(b)), and $\eta \approx 1.7$ for $N_{\text{traps}} < 7$. Note that this kind of problem is mathematically speaking equivalent to that of a continuous random walk in a hypercube, a common problem studied in mathematics [Volkov and Wong, 2008]

4.1.3 Detection of Rydberg excitations

Various techniques exist that aim at the number or position resolved detection of Rydberg atoms. One can make use of the low binding energy of Rydberg atoms by either applying a strong static electric field [Schwarzkopf, Sapiro, and Raithel, 2011], or and ionising laser [Lochead *et al.*, 2013] or ion beam [Manthey *et al.*, 2014] and then and detecting the resulting Rydberg ions. Another approach lies in detecting the change of the optical response of a cold atomic gas due to the strong Rydberg-Rydberg interactions [Gunter *et al.*, 2013]. We use a 'negative' detection scheme to determine if

an atom has been excited to a Rydberg state, since Rydberg atoms are not trapped by the microtraps and lost at the end of an experiment. We can thus deduce from the loss of an atom that it has been excited to the Rydberg state [Johnson *et al.*, 2008; Miroshnychenko *et al.*, 2010], with a single atom resolution and a $> 95\,\%$ detection efficiency.

Since the trap laser frequency is far detuned from any transitions involving the Rydberg state, we can approximate the polarisability α of the Rydberg atom by that of a free electron [Saffman and Walker, 2005]:

$$\alpha = -\frac{e^2}{m_\mathrm{e}\varepsilon_0\omega^2}, \tag{4.1}$$

where e and m_e are the charge and mass of the electron respectively, ε_0 the vacuum permittivity and $\omega/2\pi$ the frequency of the trap laser. Thus, since the polarisability for Rydberg states is negative, and the AC Stark shift proportional to $-\alpha$ [Friedrich, 1991], Rydberg states will be repelled by our 850 nm wavelength microtraps, as long as the trap light frequency is far away from all atomic resonances of the atom in the Rydberg state [Miroshnychenko *et al.*, 2010]. A trap with a typical depth of 20 MHz for ground state atoms will lead to an 'anti-trap' potential for the Rydberg states with a 'height' of 1 MHz, expelling the Rydberg atoms from the trapping region.

Thus, if the Rydberg atom has moved far enough away from the trap region before it decays back to the ground state, such that it will no longer be detected, we can use the loss of the atom from the trap during the experiment as a mean to check if the atom has been excited to a Rydberg state. For Rydberg states with $n > 50$ the lifetime is well above $50\,\mu$s [Branden *et al.*, 2010]. In $50\,\mu$s, the force on the Rydberg atoms due to the repulsive potential of the microtraps leads to a displacement of about $3\,\mu$m [Béguin, 2013]. Adding this to the finite initial velocity of the atoms (typically $\sim 60\,\mathrm{nm}/\mu\mathrm{s}$ for $T = 30\,\mu$K), the atoms will be far enough away when decaying to the ground state to not be recaptured by the trap.

We can therefore use the loss of an atom during the experiment as a signal that it has been successfully excited to a Rydberg state[3]. The maximum detected contrast of a single atom Rydberg Rabi oscillation suggests that this detection efficiency is larger than 95 %. The loss of ground state atoms during the experiment is the most detrimental effect to the detection efficiency, as will be detailed in the following

[3] In addition we have a micro-channel plate (MCP) installed in the vacuum chamber to allow e.g. positive Rydberg detection, but we have not used this in experiments yet, as its detection efficiency would be much lower than by loss detection, and would not offer a spatially resolved Rydberg detection.

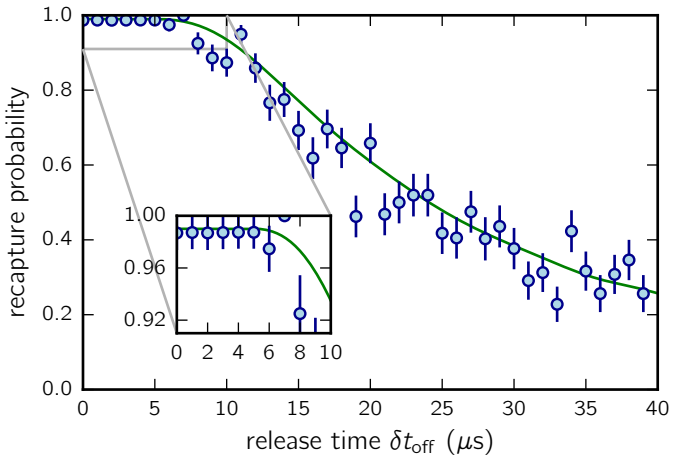

Figure 4.6: Release-and-recapture experiment of a single atom. We measure the recapture probability of a single atom after having switched the trap off for a time δt_{off}. The longer we switch off the trap, the higher the probability ε to lose the atom. The green solid line shows the best fit of the result of a Monte-Carlo simulation, giving a single atom temperature of $(30 \pm 2)\,\mu$K.

subsection.

4.1.4 Impact of detection errors

Due to the finite temperature of the single atom in the microtrap, the atoms have a small but finite probability to leave the trap region during the time that the trap is switched off for the Rydberg excitation, even if they remain in the ground state. We have measured the temperature of the atoms by a release-and-recapture experiment in a single trap. We switch the trap off for various durations and measure the probability to recapture the atom when turning the trap on again. We then fit the the data to the result of a Monte-Carlo simulation for various temperatures of the atom [Tuchendler *et al.*, 2008], and get a best fit for a temperature of the single atom of $(30 \pm 2)\,\mu$K (see Figure 4.6).

For typical experiments we switch the traps off for a few μs, where we have a probability of $\varepsilon = (3 \pm 1)\,\%$ to lose any given atom from its trap without performing any Rydberg excitation (see inset in Figure 4.6). As we detect the Rydberg atoms by the absence of fluorescence from its trap, ε thus gives us the probability to falsely identify a ground state atom as a Rydberg atom due to its loss from the trap.

One can show by a relatively simple mathematical induction that if P_q is the *detected*

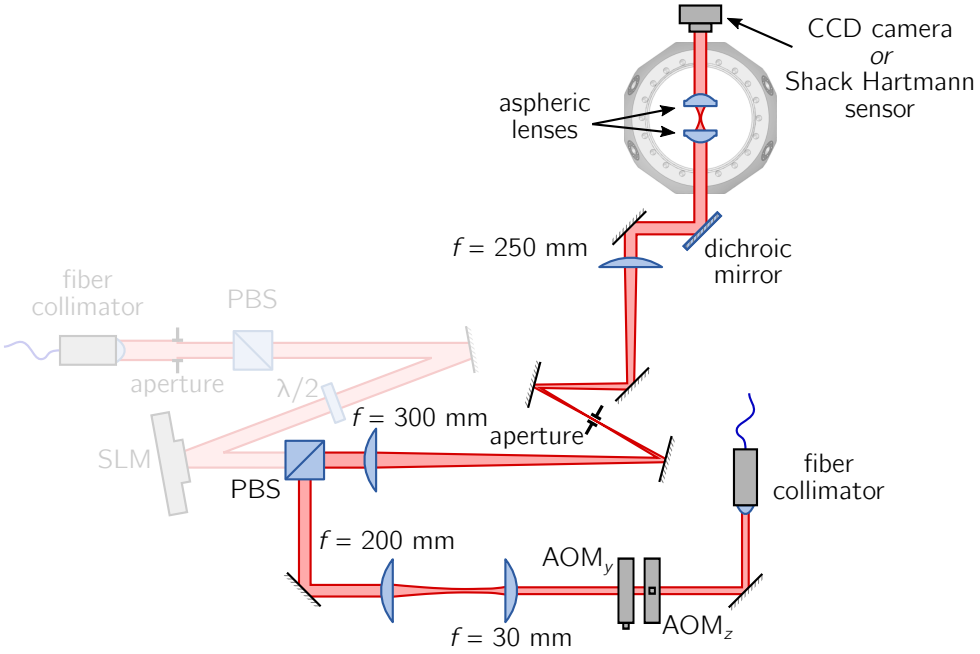

Figure 4.7: Setup of the single site addressing beam. For single site addressability we use a far red-detuned 850 nm laser beam which induces a light shift on the ground state of the addressed atom. We use two crossed AOMs for precise transverse positioning of the addressing beam (the undiffracted light is blocked by the aperture). We switch the beam using an electro-optic modulator (EOM) before the optical fiber (not shown). In the focal plane of the aspheric lens, the addressing beam has a measured $1/e^2$ radius of $w_0^{\text{add}} = 1.3\,\mu$m, slightly bigger than the waist of the microtraps.

probability to have excited q Rydberg atoms in an N atom array, and $\tilde{P}_p$ the *actual* probability to have p Rydberg excitations, then

$$P_q = \sum_{p=0}^{q} \binom{N-p}{q-p} \varepsilon^{q-p} (1-\varepsilon)^{N-q} \tilde{P}_p. \tag{4.2}$$

In principle we could correct our data for these detection error by inverting the above system of equations. In this thesis we nevertheless present only the uncorrected raw data.

4.2 Single site resolved addressing

An important feature in experiments for quantum simulation with cold atoms or ions is the local manipulation of individual qubits. This can either be done by directly

manipulating the qubit, e.g. by focusing an excitation laser on the chosen qubit [Nägerl *et al.*, 1999; Kruse *et al.*, 2010; Maller *et al.*, 2015], or by using global operations that are off-resonant for all but the selected qubit, e.g. by using electric [Lundblad *et al.*, 2009] or magnetic field gradients [Schrader *et al.*, 2004], or off-resonant laser fields [Weitenberg *et al.*, 2011; Lee *et al.*, 2013].

This section is based on our publication [Labuhn *et al.*, 2014]. As our Rydberg excitation beams are larger than the single atom arrays (see Section 2.4.3), it is not possible to selectively excite individual atoms to the Rydberg state using the excitation light only. Instead, we implemented the last of the above mentioned approaches, shining a tightly focused, far red-detuned 850 nm laser beam with a 1.3 μm $1/e^2$-radius, on a targeted site. Compared to the microtraps the addressing beam has a $\sim 30\,\%$ larger waist to reduce the sensitivity to alignment errors, and a 200 MHz frequency difference and an orthogonal polarisation in order to minimise the interference between the two.

Just like the 850 nm light field used for trapping the atom, the addressing beam induces a frequency shift on the ground state of the addressed atom, due to the AC Stark effect.

It is not possible for us to dynamically change the trapping light field with the SLM to address individual sites of the trap array, as in our experiments we need switching times in the order of a μs, whereas the the switching times of the SLM are in the order of 100 ms (see Figure 3.4). We thus installed an additional beam path for the single site addressing, which is superimposed with the trap beam with a PBS. Figure 4.7 shows the optics setup of the single site addressing. We used two crossed acousto-optic modulators (AOMs) for precise transverse positioning of the beam in the trap plane. The zero order of the AOMs is blocked by the aperture in the focus of the SLM telescope. The addressing beam is superimposed on the trap beam with a PBS, having a slightly smaller collimated waist than the latter to give a slightly larger spot in the focal plane of the aspheric lens.

In order to characterise the addressing beam, we measure its waist in the trap plane with a single atom. For this we keep the addressing beam fixed, and place a single atom at various positions along a line profile through the intensity maximum of the addressing beam. We then measure the light shift of the Rydberg excitation frequency compared to a free atom, while the trap is off and the addressing beam is on (Figure 4.8(a)). We fit a Gaussian curve to the measured light shifts from which yields a $1/e^2$ radius of the addressing beam of $w_0^{\mathrm{add}} = (1.3 \pm 0.1)\,\mu$m (Figure 4.8(b)).

Theoretically, for an ideal Gaussian beam with the measured beam parameters, we expect that if an atom is addressed with a 10 MHz light shift, another atom 3 μm

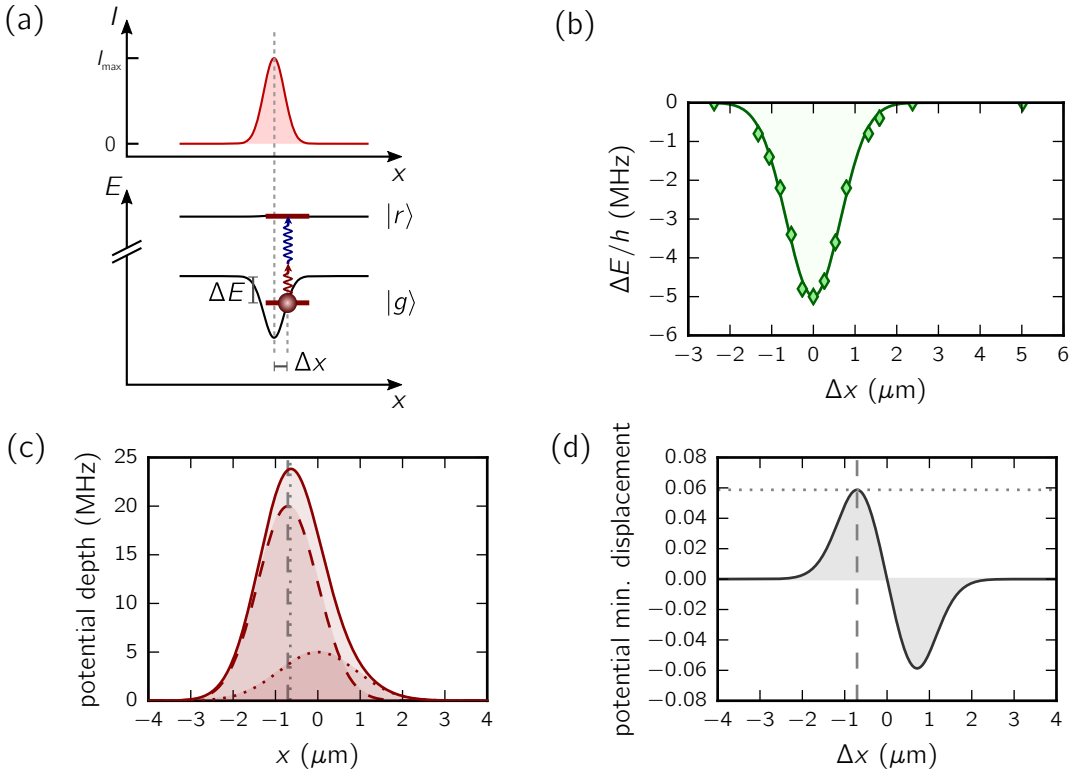

Figure 4.8: Measurement of the addressing beam profile in the trap plane. (a) We measure the addressing beam profile of the along the vertical (x) axis, by keeping the beam position fixed, while moving the position of the microtrap. We measure the light shift ΔE between $|g\rangle$ and the Rydberg state $|r\rangle = \left|82D_{3/2}\right\rangle$ at the position of the microtrap for several distances Δx from the addressing beam axis, giving us the local intensity of the addressing beam at this position. (b) Measured light shifts vs. Δx. Fitting a gaussian to the data yields a $1/e^2$ radius of $w_0 \simeq 1.3\,\mu$m. (c) The depths of the trap potential (dashed red curve), the addressing beam potential (red dotted curve), and the sum of the two (red solid curve). (d) The displacement of the potential minimum from the centre of the trap as a function of the distance Δx between the trap and the addressing focus. Even at the 'worst' distance (grey dashed line), the potential minimum displacement is at most 60 nm and is thus negligible for the measurement of the addressing beam profile.

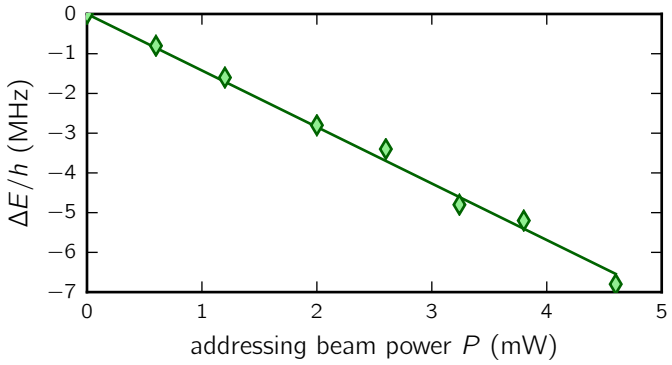

Figure 4.9: Light shift of the single atom due to the addressing beam. For different powers P in the addressing beam we measure the light shift on the transition between the ground state $|g\rangle$ and the Rydberg state $|r\rangle = \left|82D_{3/2}\right\rangle$ compared to the atom in free space. The fit gives a slope of $-1.4\,\mathrm{MHz/mW}$.

away would experience a light shift of merely 0.2 kHz, which is negligible compared to all other relevant frequencies in our experiment. When measured, the light shift at a 3 μm distance is below the experimental resolution.

In this particular experiment to measure the profile of the addressing beam, the trap and the addressing beam are on at the same time before and after the Rydberg excitation. The atom thus sees the combined potential of the two spots (Figure 4.8(c)). Nevertheless the influence of the addressing beam on the motional state of the atom is negligible for our experiments. For example, for potential depths of 20 MHz and 5 MHz for the trap and the addressing potential, the minimum of the combined potential is only shifted by 60 nm with respect to the original trap position (Figure 4.8(d)).

As we switch off the trap during the Rydberg excitation, the force on the atom due to the potential created by the addressing beam might also displace the atom. Here the trap is off for 3 μs. Even if we assume that the atom experiences the force at the maximum slope of the addressing beam potential during this time, it will only be displaced by ~ 100 nm. Therefore, the influence of the addressing beam can be neglected on the external state of the atom even when the trap is off, as long as the atoms does not see only the addressing potential for more than a few μs.

We do however see an increase of probability to lose the atom during an experiment when significantly increasing the addressing beam intensity, thus increasing the force exerted on the atom and pushing the atoms further away from the trapping region. However, for light shifts below 40 MHz, this loss probability remains below 1 %, and is thus negligible.

We also measured the light shift induced by the addressing beam on the ground-Rydberg transition as a function of the total power in the addressing beam, without moving the addressing beam between the measurements. We indeed measure the expected linear dependence on the beam power, with a slope of $-1.4\,\mathrm{MHz/mW}$. Note that the slope depends strongly on the alignment of the addressing beam with respect to the addressed microtrap. The measured slope can thus be used as a rough guide, but it is advisable to measure the exact light shift for each new alignment of the addressing beam.

4.2.1 Locally blocking Rydberg excitations

As a first application of the single-site addressability, we perform a Rydberg blockade experiment between two single atoms. This is similar to the experiment done by Urban *et al.* [2009], who used site-resolving excitation beams to demonstrate the Rydberg blockade with two atoms separated by $10\,\mu\mathrm{m}$. Here, we use our global excitation beams together with the single-site addressability to achieve similar results, for two atoms separated by only $3\,\mu\mathrm{m}$.

We tune the excitation lasers resonant to the free-space, two-photon transition between the ground state $|g\rangle$ and the Rydberg state $|r\rangle = \left|59D_{3/2}\right\rangle$, with a single atom Rabi frequency $\Omega = 2\pi \times 1\,\mathrm{MHz}$, without addressing any atom (see Figure 4.10(a)). The Rydberg-Rydberg interaction between two atoms in the $59D_{3/2}$ state, separated by $3\,\mu\mathrm{m}$, is $V_{\mathrm{vdW}} \simeq h \times 300\,\mathrm{MHz}$. Since $V_{\mathrm{vdW}} \gg \hbar\Omega$, the doubly excited state $|rr\rangle$ is shifted out of resonance. We thus only excite the symmetric superposition state

$$|s\rangle = \frac{|gr\rangle + |rg\rangle}{\sqrt{2}}, \tag{4.3}$$

with the coupling strength to this state being $\sqrt{2}\Omega$ [Urban *et al.*, 2009; Gaëtan *et al.*, 2009]. The probability $(P_{\mathrm{gr}} + P_{\mathrm{rg}})$ to find either atom in the Rydberg state thus oscillates between 0 and 1 with a frequency $\sqrt{2}\Omega$. The probability P_{rr} to have both atoms in the Rydberg state on the other hand is strongly suppressed (left Figure 4.10(c)).

If we now address atom 2 with a light shift $\Delta E \simeq 10\,\mathrm{MHz}$, it will no longer be resonant to the Rydberg excitation light (see Figure 4.10(b)). Atom 1 will therefore behave like an independent particle, oscillating between $|g\rangle$ and $|r\rangle$ with the single atom Rabi frequency Ω (Figure 4.10(d)). The remaining excitation probability of atom 2 is accounted for by detection errors [Labuhn *et al.*, 2015], falsely detecting a

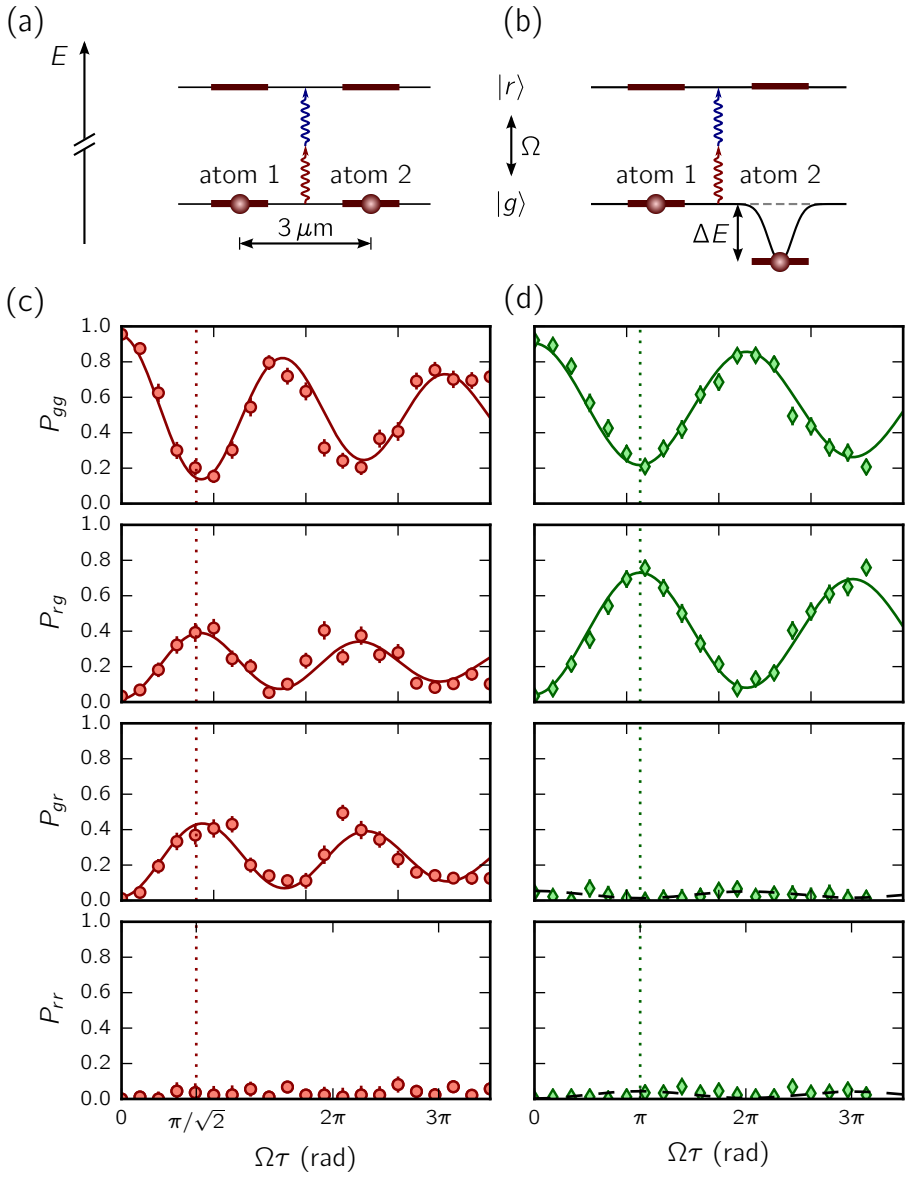

Figure 4.10: Using the addressing beam to exclude one atom from a global Rydberg excitation. Two atoms, separated by $3\,\mu$m, are illuminated by light which resonantly couples the ground state $|g\rangle$ to the Rydberg state $|r\rangle = \left|59D_{3/2}\right\rangle$ with a single atom Rabi frequency Ω, with (a) both atoms in free space, and (b) atom 2 addressed with a light shift of $\Delta E = 10\,$MHz, shifting it off-resonant from the Rydberg excitation. The time evolution of the populations in the two-atoms states $|gg\rangle$, $|rg\rangle$, $|gr\rangle$ and $|rr\rangle$ is shown, (c) for both atoms in free space, and (d) for atom 2 addressed. The solid lines are fits of damped sines to the data, the black dashed lines show the expected probability from an $\varepsilon = 3\,\%$, the dotted red and green lines indicate excitation pulses of $\pi/\sqrt{2}$ and π respectively.

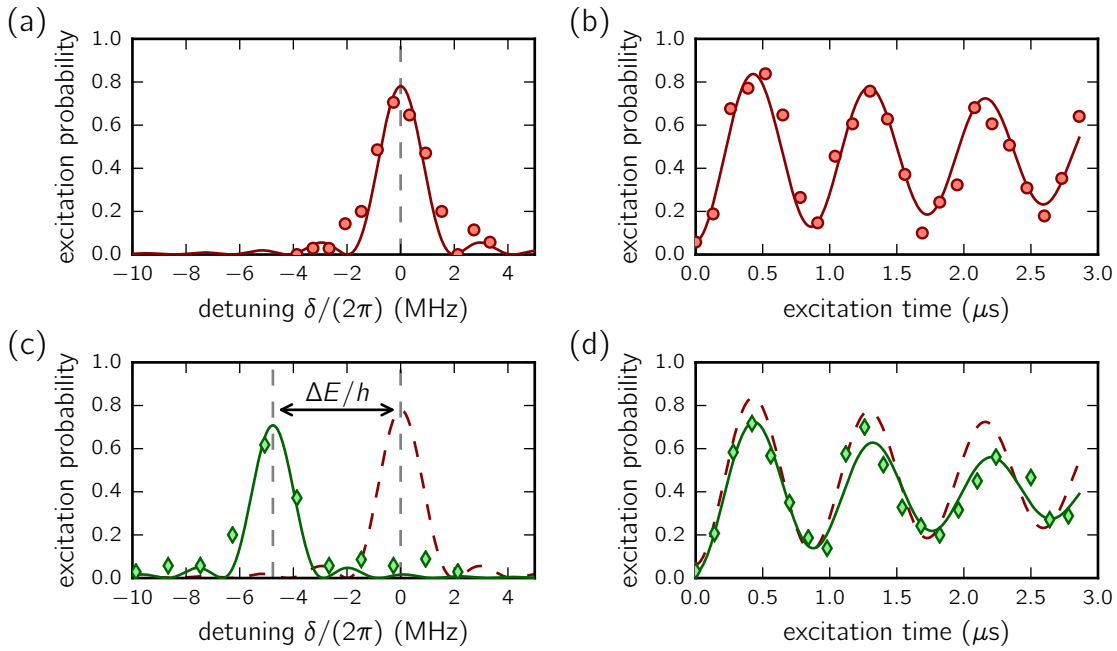

Figure 4.11: Rydberg excitation inside the addressing beam. We measure the spectrum and the Rabi frequency for the $|g\rangle \leftrightarrow |R\rangle = \left|100D_{3/2}\right\rangle$ transition, for the atom in free space (a,b), and while the atom is trapped by the addressing beam (c,d), leading to light shift of $\Delta E = -4.8\,\mathrm{MHz}$ (fit results of the free space measurement are shown as dashed light red curves for comparison).

ground state atom as a Rydberg atoms with a $\varepsilon = 3\,\%$ probability. We can therefore claim that we efficiently block atom 2 from being excited to the Rydberg state, without any measurable cross-talk.

4.2.2 In-trap Rydberg excitation

For certain experiments it may be required to use the addressing beam as an additional microtrap that can be switched independently from the holographically created traps. For example, for some experiments we would like to create a state of the form $|\psi(0)\rangle = |rgggg...\rangle$ [Olmos, Lesanovsky, and Garrahan, 2012; Schempp *et al.*, 2014]. Such a state can be prepared by switching only switching off the addressing beam 'trap' during the excitation, with the excitation beams resonant to the free-space transition. Another possibility is to switch off the holographically created traps, and tune the excitation beam resonant to the atom trapped in the addressing beam.

For comparison, we first perform a single-atom Rydberg excitation to the $|r\rangle = \left|100D_{3/2}\right\rangle$ state, only using the addressing beam as a trap with a depth of $U_0/h \simeq 20\,\mathrm{MHz}$,

and as usual switching off the trap during the Rydberg excitation. In a second experiment, we first ramp the addressing-beam trap down to a trap depth of $U_0/h \simeq 5\,\mathrm{MHz}$, but then leave it on during the Rydberg excitation. When measuring the spectrum of the trapped atom, we see the expected light shift $\Delta E/h \simeq -4.8\,\mathrm{MHz}$ of the transition frequency (see Figure 4.11(a,c)). When measuring the Rabi oscillation between $|g\rangle$ and $|r\rangle$ (Figure 4.11(b,d)), we notice that the measured single atom Rabi frequency Ω remains the same, but the contrast of the oscillation decreases and the damping gets more pronounced for the in-trap oscillation. We attribute this to the changing light shift which the atom sees in the trap. Due to the finite temperature of the atom the exact position of the atom in the trap is different in each realisation of the experiment, leading to an inhomogeneous broadening of the Rydberg transition. It is therefore preferable to perform the Rydberg excitation in free space whenever possible.

4.2.3 Local manipulation of a two-body wave function

Besides locally shifting the Rydberg transition into or out of resonance, it is also possible to use the addressing beam to manipulate the many-body wave function. We demonstrate this by again taking two atoms, $3\,\mu$m apart, in the Rydberg blockade regime ($V_{\mathrm{dd}} \gg \hbar\Omega$). We shine in an excitation pulse of duration $\pi/(\sqrt{2}\Omega)$ (see Figure 4.12(a)), preparing the atoms in the symmetric 'bright' state

$$|\psi(T=0)\rangle = \frac{1}{\sqrt{2}}(|gr\rangle + |rg\rangle). \tag{4.4}$$

We then turn on the addressing beam on atom 2, shifting the ground state energy by an amount ΔE (here we neglect the light shift on the Rydberg state). The states $|gr\rangle$ and $|rg\rangle$ therefore also differ in energy by ΔE, leading to a different phase evolution of the two parts in the wave function in Equation 4.4. After a time T, the two-atom state will therefore have evolved to

$$|\psi(T)\rangle = \frac{1}{\sqrt{2}}(|gr\rangle + e^{-i\,\Delta E\,T/\hbar}\,|rg\rangle). \tag{4.5}$$

After a time $T_\pi = \pi\hbar/\Delta E$ the system will have evolved to the antisymmetric 'dark' state

$$|\psi(T=T_\pi)\rangle = \frac{1}{\sqrt{2}}(|gr\rangle - |rg\rangle), \tag{4.6}$$

which is no longer coupled to the ground state $|gg\rangle$ by the excitation lasers. The

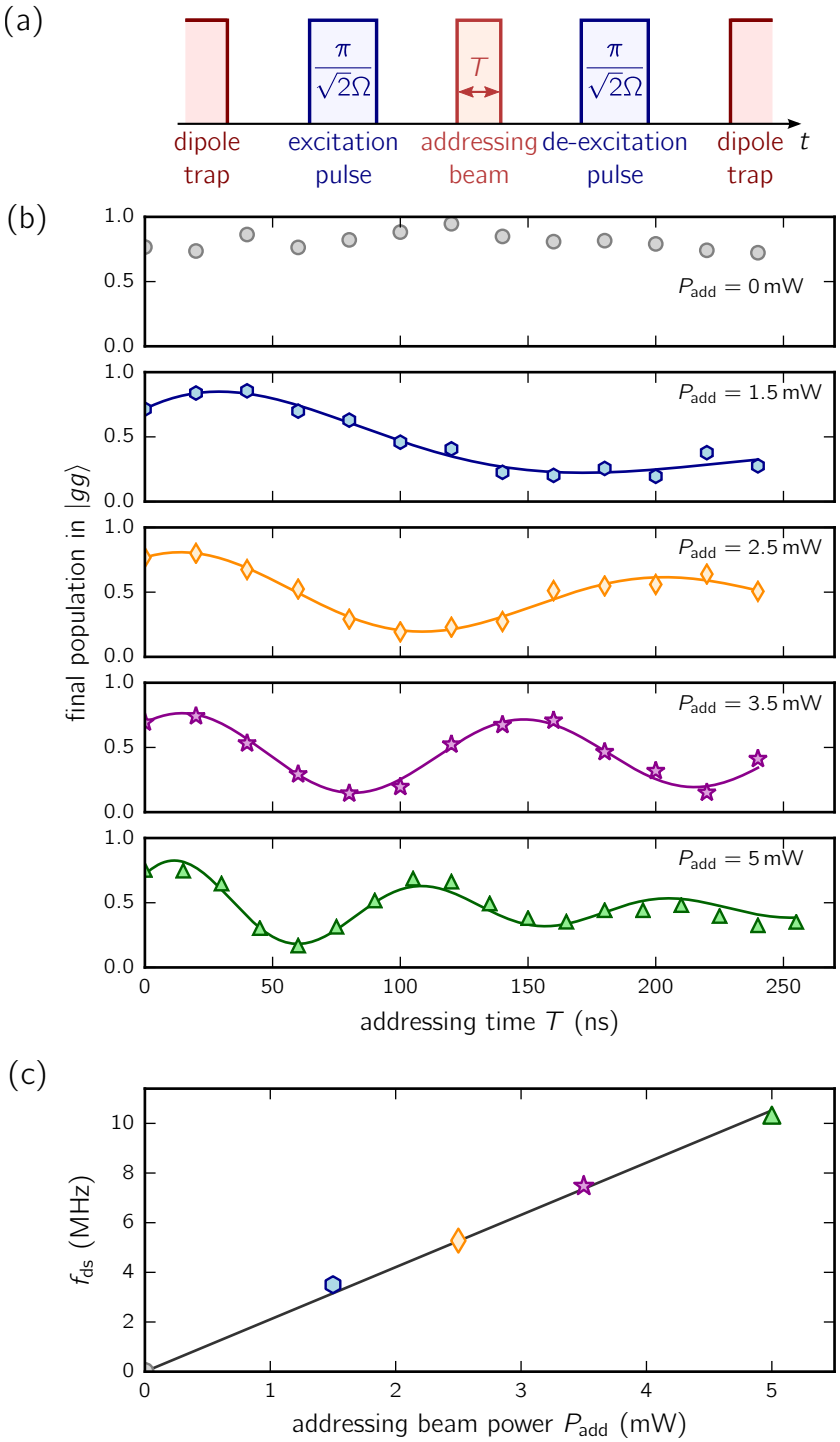

Figure 4.12: Dark state oscillations. (a) Experimental sequence: we prepare two atoms, separated by 3 μm, in the state $(|gr\rangle + |rg\rangle)/\sqrt{2}$ with $|r\rangle = |82D_{3/2}\rangle$. We then illuminate atom 2 with the addressing beam for a time T to induce a light shift ΔE, thus changing the relative phase evolution between $|gr\rangle$ and $|rg\rangle$. (b) We measure the population in the ground state $|gg\rangle$ after shining a de-excitation pulse on the atoms, for different addressing beam powers P_{add}, fitting by a damped sine with a phase offset. (c) The oscillation frequency scales linearly with the addressing beam power, with a slope of 2.1 MHz/mW.

probability of de-exciting the atoms to $|gg\rangle$ is thus expected to oscillate between 0 and 1 with a frequency $f_{\mathrm{ds}} = \Delta E/h$.

Figure 4.12(b) shows the probabilities P_{gg} to de-excite the atoms back to the ground state $|gg\rangle$ after having addressed atom 2 for a duration T. We indeed observe that the system oscillates between the bright and the dark state. We extract the oscillation frequencies by fitting the data with the function $y_0 + A\sin(2\pi f_{\mathrm{ds}} T + \phi)e^{-T/\tau_{\mathrm{ds}}}$, and see the expected linear dependence of f_{ds} on the magnitude of the addressing beam power P_{add}, i.e. the induced light shift ΔE, shown in Figure 4.12(c).

We see a constant phase offset of the oscillation of $\phi \simeq -0.1\,\pi$, which we cannot account for. The imperfect contrast of the oscillation is due to the finite Rydberg excitation efficiency, the finite detection efficiency, and the finite temperature of the atoms. The latter has the effect that on one hand atom 2 sees a slightly different light shift in each experiment, which leads to a slightly different phase evolution between the two components of the wave function between the excitation and de-excitation pulse.

On the other hand, also the movement of the atoms between the excitation and de-excitation leads to dephasing. We actually prepare the initial state $|\psi(T=0)\rangle = \frac{1}{\sqrt{2}}(|gr\rangle + e^{i\xi(T)}\,|rg\rangle)$, with $\xi(T) = \boldsymbol{k}(\boldsymbol{r}_1(T) - \boldsymbol{r}_2(T))$, $\boldsymbol{k}$ being the wave vector of the excitation light and $\boldsymbol{r}_i$ the position of atom i [Wilk *et al.*, 2010]. Due to the change of $\boldsymbol{r}_1$ and $\boldsymbol{r}_2$ during the experiment this additional phase is not entirely cancelled out during the de-excitation. The movement of the atoms thus introduced a small, random phase between $|gr\rangle$ and $|rg\rangle$ in each experiment, also leading to some additional dephasing of the measured oscillation.

4.3 Conclusion

We have demonstrated our ability to measure the fluorescence of single atoms in the microtraps in real-time with a sensitive CCD camera. The spatially resolved detection lets us start experiments on a predefined atom configuration, allowing us to work with filling fractions of the traps arrays higher than 50 % despite the random trap loading process. We deduce the successful excitation of an atom to a Rydberg state by the loss of the atom during the experiment, as we know the initial and final atom configuration of a Rydberg experiment with a fidelity of nearly 100 %. The Rydberg detection efficiency itself is limited by the small probability $\varepsilon = 3\,\%$ to lose a ground-state atom from its trap during an experiment, thus being falsely identified as a Rydberg atom.

An additional addressing beam lets us selectively excite a chosen atoms to a Rydberg

state while leaving all other atoms in the array in the ground state.

In future work, we hope to reduce the false Rydberg detections by cooling the single atoms to lower temperatures, for example using Raman sideband cooling [Kaufman, Lester, and Regal, 2012], and to implement a scheme to achieve loading probabilities of the microtraps reaching up to 90 %, which can be achieved by optimising the light-assisted collisions [Fung and Andersen, 2015; Lester *et al.*, 2015], or rearranging the atoms in the traps with the movable addressing beam [Beugnon *et al.*, 2007; Lengwenus *et al.*, 2010]

In the following two chapters we will use the presented techniques to probe both the collective enhancement and the spatial correlation of Rydberg excitations in array of single atoms.

Chapter 5

The collective enhancement of the Rydberg excitation in fully blockaded ensembles

As explained in the introductory chapter, the strong interaction among Rydberg states can lead to a situation where only atom can be excited to a Rydberg state within a certain volume at the same time. This mechanism is called Rydberg blockade. The simultaneous excitation of two atoms to a Rydberg state is prohibited if the Rydberg-Rydberg interaction V_{vdW} between the atoms leads to an energy shift of the state $|rr\rangle$, which is larger than the bandwidth of the atomic transition. A characteristic length scale for Rydberg atoms is the interatomic distance for which the interaction and the transition linewidth are equal. This length is called the Rydberg blockade radius. On our experiment, the bandwidth of the ground-Rydberg transition is given by the single atom Rabi frequency Ω_1, so that the blockade radius can be defined as

$$R_{\mathrm{b}} = \sqrt[6]{\frac{C_6}{\hbar\Omega_1}}, \tag{5.1}$$

with the van der Waals interaction $V_{\mathrm{vdW}} = C_6/R^6$ being the dominant interaction here. The blockade radius thus scales as $n^{11/6}$ with the principal quantum number n.

The concept of the Rydberg blockade is not only valid for two atoms but also for larger ensembles of atoms, as long as all the atoms in the ensemble are *pairwise blockaded*. If this condition is fulfilled, then it is only possible to excite one single atom in the ensemble to the Rydberg state at the same time. As a consequence, the Hilbert space reduces from 2^N states to just two states. These are the ground state

$$\left|g^{(N)}\right\rangle = |g_1 g_2 ... g_N\rangle\,, \tag{5.2}$$

and the state with a single Rydberg excitation, which, since we do not know *which*

atom has been excited, is the N-atom superposition state

$$\left|\psi_{1r}^{(N)}\right\rangle = \frac{1}{\sqrt{\sum_{i=1}^{N}|\Omega_i|^2}} \sum_{i=1}^{N} \Omega_i e^{i\boldsymbol{k}\cdot\boldsymbol{R}_i} \left|g_1 g_2 \ldots r_i \ldots g_N\right\rangle , \tag{5.3}$$

with the Rydberg excitation shared among all the atoms. Here, Ω_i is the local Rabi frequency of atom i, $\boldsymbol{R}_i$ its position and $\boldsymbol{k}$ the wavevector of the excitation laser.

Due to the collectivity of the single Rydberg excitation, the coupling strength between the ground state $\left|g^{(N)}\right\rangle$ and the collectively excited state $\left|\psi_{1r}^{(N)}\right\rangle$ is enhanced compared to that of a single atom, now being

$$\Omega_N = \sqrt{\sum_{i=1}^{N}|\Omega_i|^2}. \tag{5.4}$$

If we assume that all atoms in the blockade sphere have the same single atom Rabi frequency, i.e. $\Omega_i = \Omega_1$ for all atoms i, then this enhancement[1] is exactly $\sqrt{N}$:

$$\Omega_N = \sqrt{N}\Omega_1. \tag{5.5}$$

In addition, if one can ignore the phase factors $e^{i\boldsymbol{k}\cdot\boldsymbol{R}_i}$ in Equation 5.3, i.e. the interatomic distances are small compared to the wavevector $\boldsymbol{k}$ of the excitation light, we excite the highly symmetric $|W\rangle$-state

$$\left|W^{(N)}\right\rangle = \frac{1}{\sqrt{N}} \sum_{i=1}^{N} \left|g_1 g_2 \ldots r_i \ldots g_N\right\rangle , \tag{5.6}$$

with a multi-partite entanglement among the atoms [Wilk *et al.*, 2010; Haas *et al.*, 2014; Zeiher *et al.*, 2015]. In the experiments presented in this thesis, the phase factors do not vanish, since the atomic separations of several micrometer is much larger than the effective two-photon wavevector $\boldsymbol{k} = \boldsymbol{k}_\mathrm{R} + \boldsymbol{k}_\mathrm{B}$ of the red and the blue excitation light. However, we could in principle map the Rydberg states to a different hyperfine level of the ground state with a separate optical de-excitation pulse, thus cancelling out the excitation and de-excitation wavevectors [Wilk *et al.*, 2010]. For ^{87}Rb, the wavevector of the 6.835 GHz hyperfine splitting of the ground state is then negligible compared to the interatomic spacings.

[1] Due to the enhanced coupling strength to the collectively excited state, the N atom blockade radius slightly decreases to $R_\mathrm{b}^{(N)} = \sqrt[6]{\frac{C_6}{\hbar\sqrt{N}\Omega}} = R_\mathrm{b}/\sqrt[12]{N}$. As the effect is quite small – R_b decreases by 25 % for 30 atoms – we assume Eq. 1.1 also to be valid for multiple atoms.

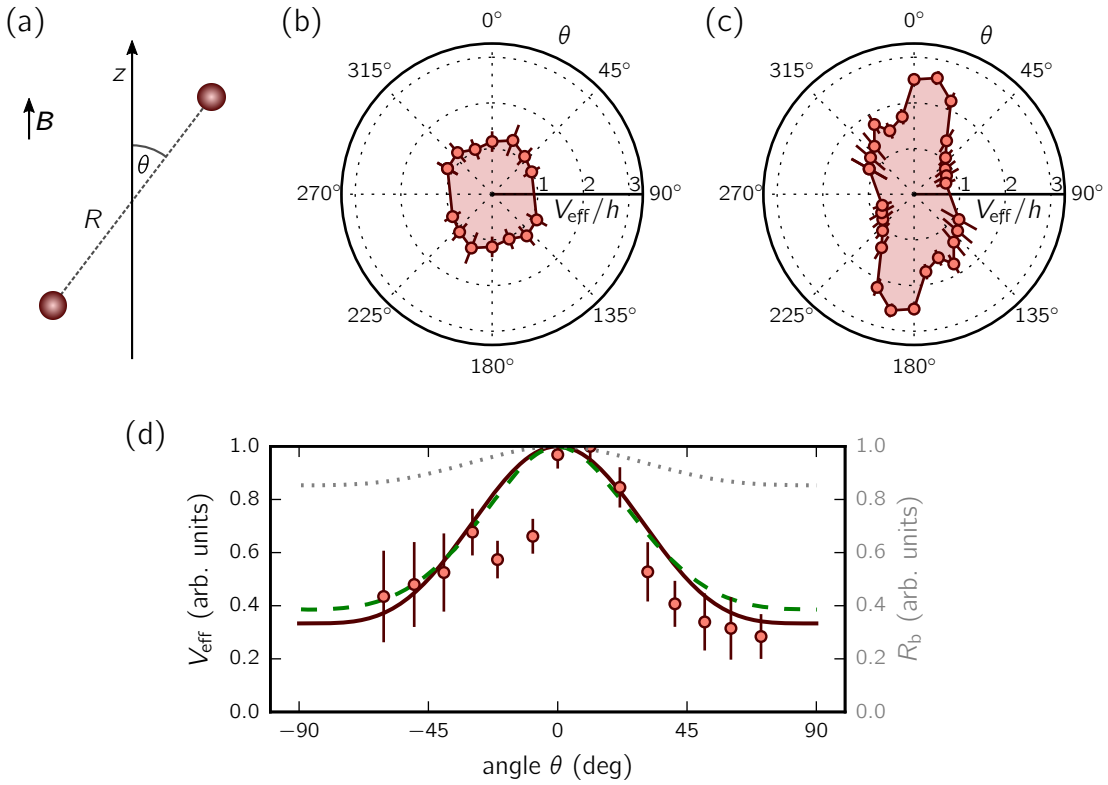

Figure 5.1: Anisotropy of the van der Waals interaction. Effective interaction strength $V_{\mathrm{eff}}(\theta)/h$ measured for two atoms, with interatomic distance $R = 12.4\,\mu m$, as a function of the angle θ between the internuclear axis and the quantisation axis (a), for the Rydberg states (b) $\left|82S_{1/2}, m_j = 1/2\right\rangle$, and (c) $\left|82D_{3/2}, m_j = 3/2\right\rangle$ (radial axes in MHz). (d) *Green dashed line*: Calculated effective potential $V_{\mathrm{eff}}(\theta)$ for the $\left|nD_{3/2}, m_j = 3/2\right\rangle$ state, adapted from Figure 6(b) in [Vermersch, Glaetzle, and Zoller, 2015]. *Red solid line*: Approximation of the calculated effective potential by $V_{\mathrm{eff}}(\theta) = V_{\mathrm{eff}}(0) \cdot [1 + 2\cos(\theta)^4]/3$ (data points the same as in (c)). *Grey dotted line*: Blockade radius R_{b} (see Equation 5.1).

5.1 The role of the anisotropy of the interaction

The van der Waals interaction among Rydberg states is not necessarily isotropic [Carroll *et al.*, 2004; Reinhard *et al.*, 2007; Vermersch, Glaetzle, and Zoller, 2015], and therefore also the blockade volume can deviate from a spherical shape. While the van der Waals interaction for S Rydberg states is fairly isotropic, D states can show strong anisotropy in their interaction.

Furthermore, if the angle θ between the interatomic axis and the quantisation axis is non-zero, the van der Waals interaction can couple all Zeeman sublevels of the Rydberg state. In our case of Rydberg states $j = 3/2$, thus describing the van der

Waals interaction for all Zeeman-sublevel pairs leads to a 16×16 interaction matrix. Although the full numerical calculation of the interaction for non-zero angles taking into account all Zeeman sublevels poses no difficulty for two atoms, it quickly becomes intractable for an increasing number of atoms. It is therefore helpful to introduce an effective, anisotropic van der Waals potential $V_{\text{eff}}(R, \theta)$, which is defined as the weighted average of the various interaction channels for a given angle θ, reducing the previous interaction matrix again to a single scalar [Vermersch, Glaetzle, and Zoller, 2015]. Since there exists no analytical solution for $V_{\text{eff}}(\theta)$, we use for the sake of simplicity an heuristic formula

$$V_{\text{eff}}(R, \theta) = \frac{C_6(0)}{R^6} \cdot \frac{1 + 2\cos^4(\theta)}{3} \tag{5.7}$$

to describe the anisotropy of the interaction, which reproduces well the numerical curve, as shown in Figure 5.1(d). We see that changing θ from 0 to 90° reduces the effective interaction by a factor 3. The anisotropy of the Rydberg blockade radius is much smaller than for the interaction strength, due to the dominating effect of the $1/R^6$ scaling of the van der Waals interaction. The blockade volume defined by $V_{\text{eff}}(\theta) = \hbar\Omega_1$ can be well approximated by a prolate spheroid with an aspect ratio of about $3^{1/6} \simeq 1.2$.

We have measured the angular dependence of both S and D Rydberg states, shown in Figure 5.1(b,c), by looking at the coherent excitation dynamics of two atoms separated by $R \simeq R_{\text{b}}$, as we have described in [Barredo *et al.*, 2014]. The slight asymmetry observed for the D-state is most likely due to a systematic error: The effective potential V_{eff} is defined for a vanishing double-excitation probability. However, to be able to determine the interaction V, we need $V \approx \hbar\Omega_1$ (see [Béguin *et al.*, 2013]), leading to non-negligible double excitation probability. The exact magnitude of these double excitations was different for positive and negative angles θ, resulting in slightly different values of the obtained V_{eff}. More details on the anisotropy of the van der Waals interaction can be found in the thesis of Sylvain Ravets [2014].

We will see later in this chapter that for large number of atoms, the approach of an effective potential to describe the van der Waals interaction at non-zero angles becomes questionable in some cases, as the blockade seems to be no longer perfect when we increase the number of atoms inside the blockade volume.

5.2 Experimental observation of the Rydberg blockade in a fully blockade ensemble

The collective enhancement of the Rabi frequency in fully blockaded ensembles of cold atoms have been reported on in a dilute cloud [Heidemann *et al.*, 2007], an optical dipole trap [Ebert *et al.*, 2014], one-dimensional [Dudin *et al.*, 2012] and two-dimensional [Zeiher *et al.*, 2015] optical lattices. However, all of these experiment suffer from uncertainties or spreads in the prepared atom numbers.

Here we present our experimental results on the collective Rydberg excitation of a fully blockaded ensemble of atoms, with negligible uncertainties in the prepared atom numbers and complete counting statistics of the Rydberg excitations.

Our measurement was divided into two parts. For the first series experiments with up to nine atoms, we prepared a trap array with the respective number of traps and waited until all traps contained exactly one atom before launching the experiment. We placed the traps on a 3×3 square grid with a lattice spacing of $a = 3\,\mu$m. Depending on the desired atom number of the experiment, we put between one and nine traps on the grid, arranged as shown in the fluorescence images in Figure 5.2. Since there is a finite probability for the atom configuration to change *after* the experiment has been triggered, as described in Section 4.1.1, we *post-selected* the experiments on those where the initial frame shows a fully loaded arrays.

For more than nine traps, waiting for all traps in the array to contain one atom is no longer feasible as mentioned in Section 4.1.2, since the probability to have a fully loaded array gets too low and the experimental cycle time thus too long[2]. To probe the collective enhancement for more than nine atoms, we thus used a 19 trap array in triangular geometry, which we triggered on having between 8 and 15 atoms in the traps[3]. We post sorted the experiments according to the number of atoms in the trap array in the initial atom configuration. The triangular lattice has a lattice spacing of $3.6\,\mu$m, as shown in top right of Figure 5.3. The distance between any pair of traps in the array is smaller than $15\,\mu$m. We slightly increased the principal quantum number of the used Rydberg state to $n = 100$ to ensure full blockade among all atoms. All important experimental parameters used in each experiment are given in Table 5.1.

Once the experiment has been triggered, the atoms are prepared in the ground state

[2] For a fully loaded 9-trap array the cycle time of the experiment is around one minute.

[3] For the experiments on the partially loaded array with 8 and 9 atoms we removed two traps, one on the very left and one on the very right of the triangular array.

Table 5.1: Experimental parameters used for the experiments. Parameters of the trap array and the used Rydberg state for the fully loaded square array on the 3×3 grid (Figure 5.2), and the partially loaded triangular trap array (Figure 5.3). The C_6 coefficients are obtained using second-order perturbation theory, as described in [Béguin, 2013].

	trap array parameters			**Rydberg state parameters**			
experiment	spacing a (μm)	N_t	N	n	C_6/h (MHz μm^6)	$\Omega_1/(2\pi)$ (MHz)	R_b (μm)
fully loaded	3.0	1–9	N_t	82	-8.9×10^6	1.5	14
partially loaded	3.6	19	8–15	100	-7.3×10^4	1.1	20

(see Section 2.4)

$$\left|g^N\right\rangle = \left|g_1 g_2 ... g_N\right\rangle . \tag{5.8}$$

We then switch off the traps for $3\,\mu$s, and shine in an excitation pulse of duration τ which is resonant to the single atom transition $|g\rangle \leftrightarrow |r\rangle$, with a single atom Rabi frequency $\Omega_1 \simeq 1.5\,$MHz, and finally count the number of detected Rydberg atoms.

The measured probabilities to have 0, 1 and 2 Rydberg excitations are shown in Figure 5.2 for the fully loaded arrays, and in Figure 5.3 for the various atom numbers of partially loaded array. To extract the collective Rabi frequency Ω_N, we fit an asymmetrically damped sine of the form

$$P(\tau) = a e^{-\gamma\tau} \left(\cos^2(\Omega_N \tau/2) + b\right) + c \tag{5.9}$$

where a, b, c, γ and Ω_N are adjustable parameters of the fit. This functional form was chosen to account in a simple way for the observed asymmetry in the damping of the oscillation. We observe a speedup of the oscillation with increasing atom number, as well as an increase of the damping rate. We also see an increase of the double excitation probably with excitation time, which seems to depends on the geometry of the trap array. We will discuss these observations later in this chapter.

We extract the collective N-atom Rabi frequencies between $\left|g^N\right\rangle$ and $\left|\psi_{1r}^{(N)}\right\rangle$ from the fits to the zero excitation probabilities, i.e. the left panels in Figures 5.2 and 5.3, and normalise them to the respective single atom Rabi frequencies Ω_1, measured on a single atom in the centre of the array. The obtained enhancement, shown in Figure 5.4(a), follows quite closely the expected $\sqrt{N}$ behaviour. It appears that the enhancement is slightly lower than expected for the fully loaded array.

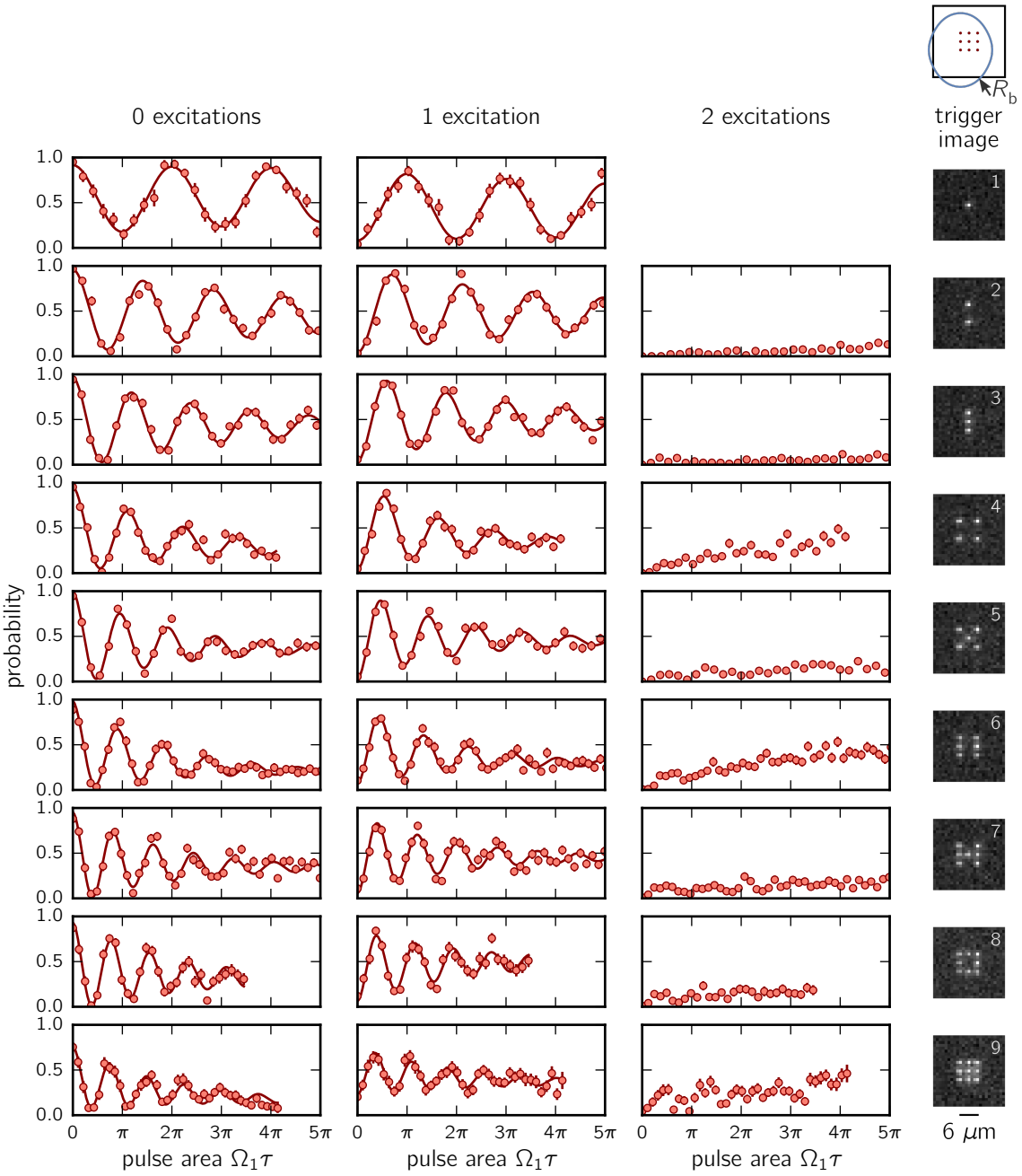

Figure 5.2: Rydberg excitation dynamics in fully loaded trap arrays with one to nine traps. We show the probabilities to have zero (left), one (middle), or two Rydberg excitations (right) for fully loaded trap arrays, with one (top) to nine (bottom) traps, on a 3×3 grid with a $3\,\mu$m lattice constant. The images at the very right show examples of trigger images for the respective atom numbers. We use the Rydberg state $|r\rangle = |82D_{3/2}\rangle$, giving a calculated blockade radius of $R_b > 10\,\mu$m in all directions (see fluorescence image for $N_{at} = 8$ atoms). The x-axes are the product of the excitation time τ and the single atom Rabi frequency $\Omega_1 \simeq 2\pi \times 1.5\,$MHz. The solid lines are fit of asymmetrically exponentially damped sines (see text). The error bars show the quantum projection noise for the ~ 100 repetitions of each experiment.

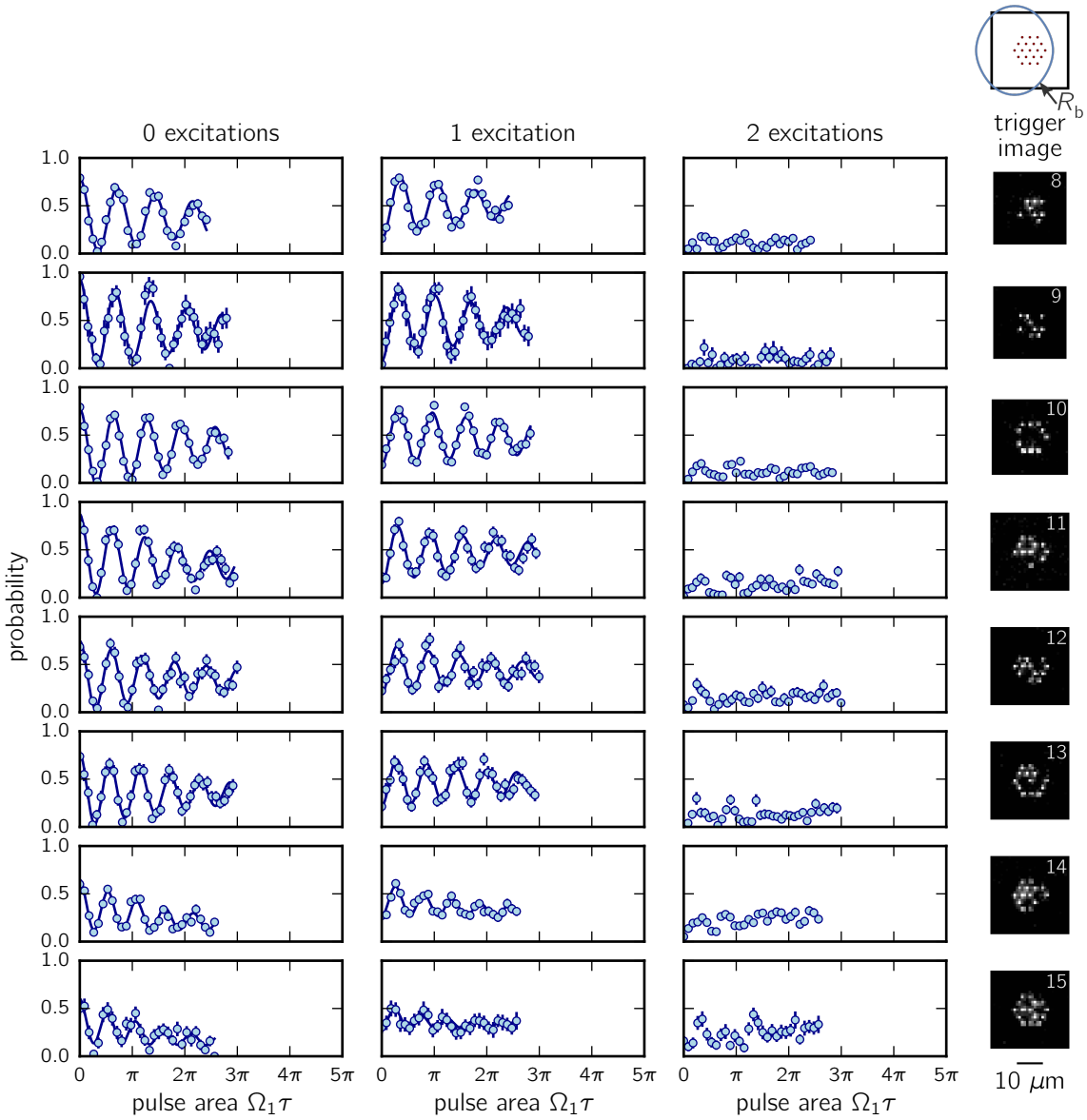

Figure 5.3: Rydberg excitation dynamics in a partially loaded 19 trap array. We show the same plots as in Figure 5.2, for a triangular lattice with 19 traps with a $3.6\,\mu$m nearest neighbour spacing, containing between 8 and 15 atoms (top to bottom). We use the Rydberg state $|r\rangle = \left|100D_{3/2}\right\rangle$, giving a calculated blockade radius of $R_b > 14\,\mu$m in all directions (see fluorescence image for $N_{at} = 15$ atoms). The x-axes are the product of the excitation time τ and the single atom Rabi frequency $\Omega_1 \simeq 2\pi \times 1.1\,$MHz. The solid lines are fit of asymmetrically exponentially damped sines (see text). The error bars show the quantum projection noise for the ~ 100 repetitions of each experiment.

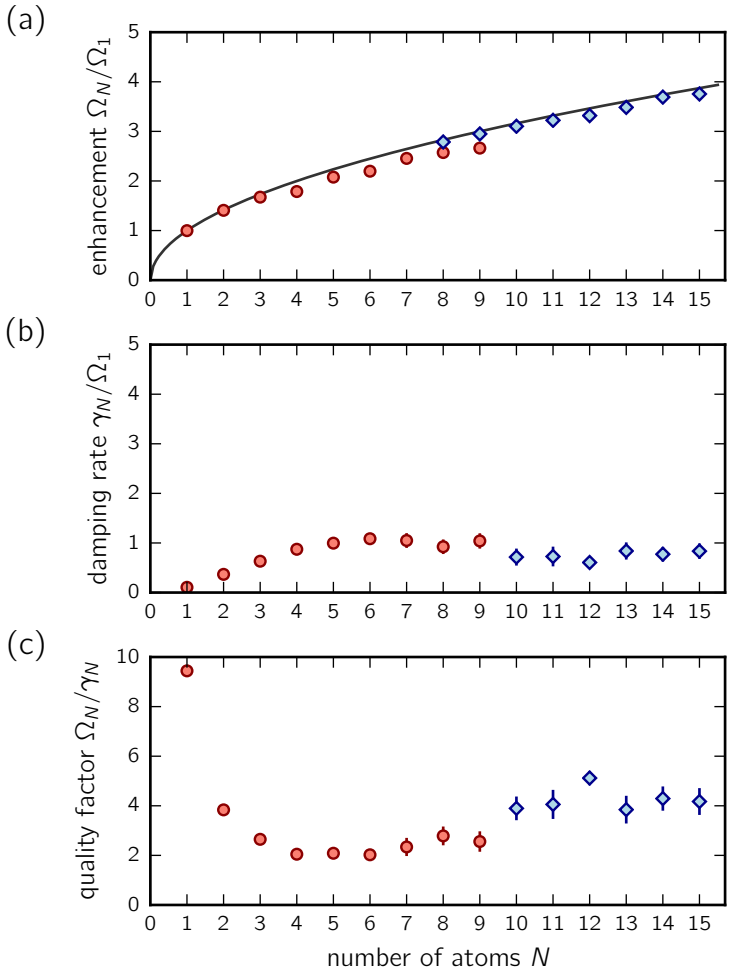

Figure 5.4: Rabi frequency and damping rate of the multi-atom Rabi oscillation. Parameters extracted from zero excitation dynamics of the fully loaded (red circles) and partially loaded (blue squares) trap arrays in Figures 5.2 and 5.3. (a) Enhancement of the collective Rabi frequency Ω_N compared to the single atom Rabi frequency Ω_1 of an atom in the centre of the array. The solid line shows the expected $\sqrt{N}$ behaviour. (b) Exponential damping rates in units of the respective single atom Rabi frequencies. (c) The ratio of the Rabi frequency and the damping rate, showing that the quality of the oscillations gets worse for more than one atom, but then stays roughly constant. Error bars (sometimes smaller than the data points) are 1σ statistical uncertainties from the fits.

Figure 5.4(b) shows the damping rates γ_N obtained from the fits. One sees that γ_N first increases with the number of atoms, although slower than Ω_N. This becomes more apparent when looking at the quality factor of the oscillation, given by the ratio of the Rabi frequency and the damping rate Ω_N/γ_N, shown in Figure 5.4(c). We see that the quality factor first decreases for more than one atom, and then seems to remain constant for larger atoms numbers.

5.3 Analysis of the experimentally observed imperfect blockade

We will now look at various possible sources of noise to account for the increase of the damping with increasing atom number, and the non-zero double excitation probability.

5.3.1 Analysis of the possible sources of noise

In order to quantify the effect of some of our imperfections, we numerically solve the time-dependent Schrödinger equation with the Hamiltonian of N two-level atoms

$$\hat{H} = \sum_i \frac{\hbar|\Omega_i|}{2}(e^{i\boldsymbol{k}\cdot\boldsymbol{R}_i}\hat{\sigma}_{rg}^{(i)} + e^{-i\boldsymbol{k}\cdot\boldsymbol{R}_i}\hat{\sigma}_{gr}^{(i)}) + \sum_{i<j} V_{ij}\hat{\sigma}_{rr}^{(i)}\hat{\sigma}_{rr}^{(j)} + \sum_i \hbar\delta_i\hat{\sigma}_{rr}^{(j)}, \tag{5.10}$$

with $\boldsymbol{R}_i$ the position of atom i, $\hat{\sigma}_{rg}^{(i)} = |g\rangle\langle r|$ and $\hat{\sigma}_{gr}^{(i)} = |r\rangle\langle g|$ the transition operator, $\hat{\sigma}_{rr}^{(i)} = |r\rangle\langle r|$ the projection operator on the Rydberg state, and $V_{ij} = C_6/|\boldsymbol{R}_i - \boldsymbol{R}_j|^6$ the van der Waals interaction. In order to keep the calculation tractable, we truncate the Hilbert space removing all states containing more than 4 Rydberg excitations, and limit the maximum strength of a pairwise van der Waals interaction[4] to $\max\{|V_{\mathrm{vdW}}|\} = h \times 300\,\mathrm{MHz}$.

Inhomogeneous laser couplings: Experimentally we measure slightly different single atom Rabi frequencies Ω_1 for the trap positions in the arrays. For the 3×3 array, we measure variations of $\pm 5\,\%$ with respect to the mean Rabi frequency. For the 19 trap triangular lattice we observe variations of $\pm 10\,\%$. These inhomogeneities are due to the Gaussian intensity profile of the excitation laser beams, as explained

[4] Very large interactions will shift the respective state far off-resonant. This may cause very fast oscillations of the population of the state, but with negligible amplitude. Those oscillations have no contribution to the evolution of the states, but can significantly slow down the numerical differential equation solver, as it will drastically reduce the time step size to follow those fast oscillations.

in Section 2.4.3. According to Equation 5.4, this leads to a small reduction of the collectively enhanced coupling strength Ω_N, but does not increase the probability to create multiple excitations. For fully loaded arrays, an Ω_i varying from site to site will not introduce any damping or reduce the contrast of the oscillation. For partially loaded trap arrays however, the sites i participating in an experiment changes for each realisation of the experiment, and thus also the involved Ω_i. The collective Rabi frequency Ω_N will therefore also vary slightly from shot to shot, leading to a small effective damping of the measured oscillation, which is too small to notice for our experimental parameters.

Inhomogeneous detunings: Spatial variations of the red and blue Rabi frequencies Ω_R and Ω_B among the atoms may lead to variations of the effective detunings $\delta_i = (|\Omega_\mathrm{B}^{(i)}|^2 - |\Omega_\mathrm{R}^{(i)}|^2)/(4\Delta)$ of the ground-Rydberg transition. They result in the different components of $|\Psi_{1r}\rangle_N$ having different energies, leading to a beating of several frequencies in the collective Rabi oscillation, which may be interpreted as damping on the data. A numerical evaluation of the N-atom Schrödinger equation, with the Hamiltonian from 6.1 and $\Omega_i = \Omega_1$, shows that this only becomes significant for $\langle|\delta_i|\rangle \gtrsim 0.2\ \langle\Omega_i\rangle$. We measured the individual detunings from $|r\rangle$ to be $\langle|\delta_i|\rangle < 0.05\ \langle\Omega_i\rangle$, which leads to no noteworthy modification of the collective Rabi oscillation.

Motion of the atoms: The finite temperature of the atoms of $T \approx 30\,\mu$K leads to a residual motion of the atoms during the excitation, with $v_\mathrm{th} = \sqrt{k_\mathrm{B}T/m} \simeq 0.06\,\mu\mathrm{m}/\mu\mathrm{s}$. The associated Doppler effect yields a distribution of frequency shifts $\sigma_\delta = |\boldsymbol{k}_\mathrm{R} + \boldsymbol{k}_\mathrm{B}|\, v_\mathrm{th} \simeq 2\pi \times 0.15\,\mathrm{MHz}$. This appears to be similar to the above mentioned inhomogeneous detunings due to the excitation light shifts. However, the velocity of the atoms is different in each realisation of the experiment, and thus each time every atom will see a slightly different Doppler shift. This will show as a true dephasing of the collective Rabi oscillation over multiple realisations of the experiment.

To numerically simulate the effect of the atomic motion, we modify the Hamiltonian in Equation 6.1 to include the finite velocity, changing the phase factor[5] $e^{i\boldsymbol{k}\cdot\boldsymbol{R}_i} \to e^{i\boldsymbol{k}\cdot(\boldsymbol{R}_i+\boldsymbol{v}_i t)}$, the interaction $V_{ij} = C_6/|\boldsymbol{R}_i - \boldsymbol{R}_j|^6 \to V_{ij} = C_6/|\boldsymbol{R}_i + \boldsymbol{v}_i t - \boldsymbol{R}_j - \boldsymbol{v}_j t|^6$, and adding a detuning $\delta_i = |(\boldsymbol{k}_\mathrm{R} + \boldsymbol{k}_\mathrm{B})\, \boldsymbol{v}_\mathrm{th}|$, with $\boldsymbol{v}_i$ being the velocity, for each atom i. Here we set $\varepsilon = 0$, and $\Omega_i = \Omega_1$ for all i. We average over 100 realisations of the simulation, each time drawing different velocities for the atoms according to the velocity distribution given by the respective temperature. The small variations in $\boldsymbol{R}_i$

[5] The change of $\boldsymbol{k}$ due to the Doppler effect is negligible for the phase factor.

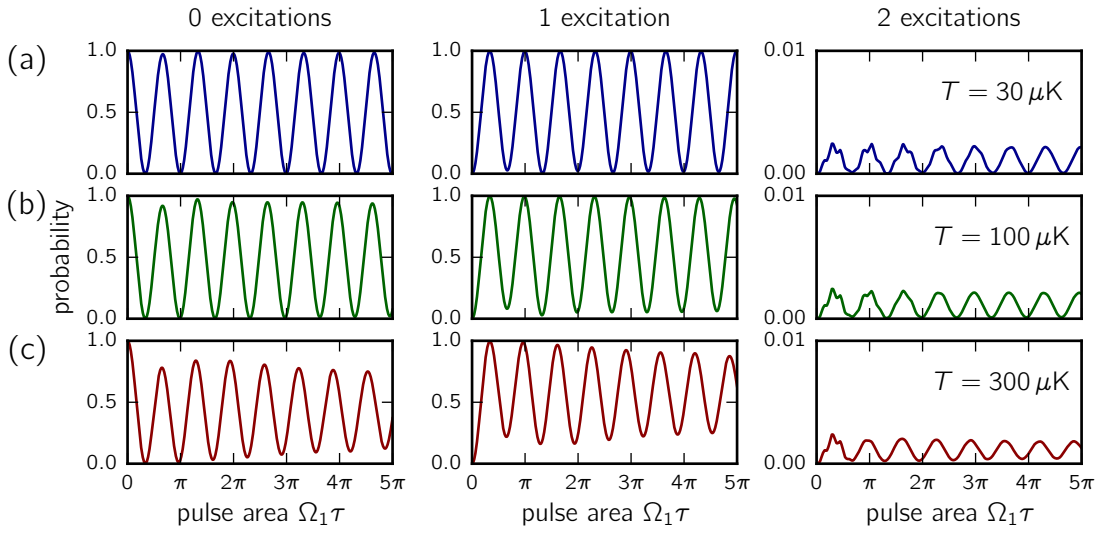

Figure 5.5: Effect of a finite temperature on the collective oscillation of 9 atoms. We solve the time dependent Schrödinger equation for a 3×3 atom array, taking the same parameters as in the experiment and including the movement of the atoms, for three different temperatures of the atom, $30\,\mu$K, $100\,\mu$K and $300\,\mu$K (a, b and c). We average over 100 realisations of the simulation, each time drawing different velocities of the atoms according to the distribution given by the respective temperature, and taking an $\varepsilon = 0$. We see that for $30\,\mu$K, the temperature of the atoms in our experiment, we hardly see any effect on the collective oscillation. The probability to excite states with multiple Rydberg excitations is negligible (note the different y-axis of the plots in the right column).

in the order of $\sim 100\,$nm has no effect on the dynamics, and is not taken into account here.

The result of the simulation for 9 atoms in the 3×3 trap array is show in Figure 5.5. We see that for the temperature of our atoms of $T = 30\,\mu$K the influence of the motion is hardly visible. The oscillation starts to show some damping only if the temperature exceeds $\sim 100\,\mu$K. In addition, we do not see any significant population in the multiple-excitation states. The same observations also holds true for the other atoms numbers in the 3×3 array.

False Rydberg detections: As we have mentioned in Section 4.1.3, there is a finite probability of falsely detecting a ground state atom as a Rydberg atom. This is caused by a ground state atom leaving the trapping region during the excitation, thus being lost from the trap and falsely registered as a Rydberg atom. To picture the effect of these detection errors, we assume to have no imperfection in the experiment, including a perfect Rydberg blockade. The probabilities to have 0 or 1 excitation would

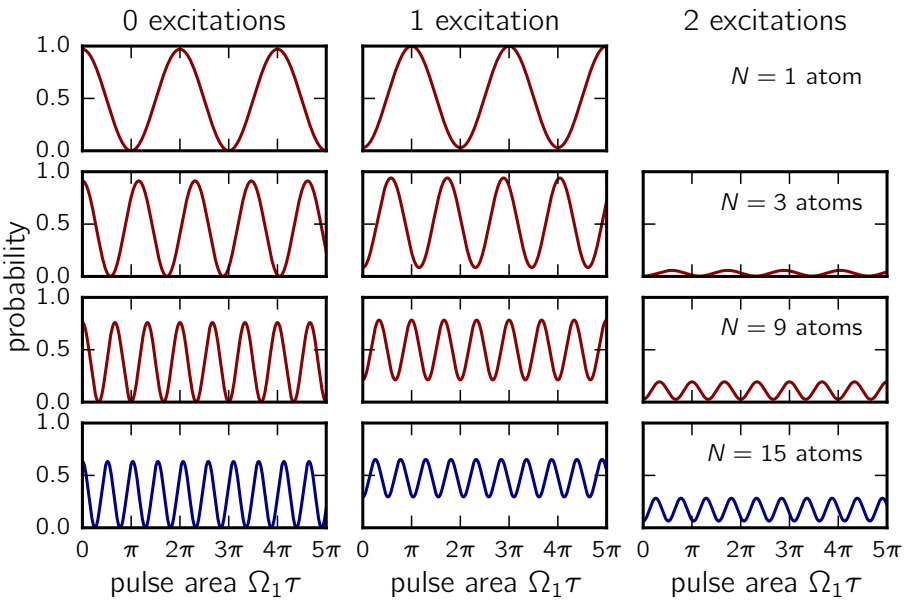

Figure 5.6: Effect of the false Rydberg detection on an ideal collective Rabi oscillation. Theoretically obtained curves for $N = 1, 3, 9$ and 15 atoms (top to bottom), assuming a *perfect blockade*, i.e. $P_{1r}^{(N)}(\tau) = \sin(\sqrt{N}\Omega_1\tau/2)^2$, for a false Rydberg detection probability $\varepsilon = 3\,\%$. We show the probability to have 0, 1 or 2 excitations (from left to right). For $\varepsilon = 0$, P_{2r} would be zero in all cases.

then be $P_{0r}^{(N)}(\tau) = \cos(\sqrt{N}\Omega_1\tau/2)^2$ and $P_{1r}^{(N)}(\tau) = \sin(\sqrt{N}\Omega_1\tau/2)^2$, respectively. All populations of multiple-excitation states would be zero.

If we now add a finite false Rydberg detection probability, the observed probabilities will be modified according to the set of Equations in 4.2, and are shown in Figure 5.6 for $N = 1, 3, 9$ and 15 atoms, for $\varepsilon = 3\,\%$ as on the experiment. We notice a decrease of the oscillation amplitude of P_{0r} and P_{1r}, which in first order of ε is proportional to the number of atoms. We see and a significant population of the doubly excited state P_{2r} for larger atom numbers, which in first oder of ε is given by $P_{2r} \simeq (N-1)\varepsilon P_{1r}$. The effect is constant though for all excitation times τ.

We therefore conclude that we can account for the most part of the decreasing contrast of the oscillation with the false Rydberg detection, but we so far do not fully understand the increase of the damping rate when going from one to a few atoms, nor the increase of P_{2r} with τ, which we observed for some trap configurations. Overall, the observed damping is comparable to that observed by Zeiher *et al.* [2015] on single atoms in an optical lattice, who claim that it "might be due to phase noise and slow frequency drifts of the laser", or an incoherent coupling to nearby Rydberg

states [Ebert *et al.*, 2015]. More work is needed to clarify the imperfect Rydberg blockade when using Rydberg D-states.

5.3.2 Double-excitation analysis

In the following section we will investigate the observed double excitation events in the full Rydberg blockade regime.

The non-perfect contrast of the Rabi oscillations between $\left|g^{(N)}\right\rangle$ and $\left|\psi_{1r}^{(N)}\right\rangle$ in Figure 5.2 and 5.3 is mostly attributed to our imperfect optical detection, losing ground state atoms during the excitation and falsely detecting them as Rydberg atoms with an $\varepsilon \simeq 3\,\%$ probability. However, since the time during which we switch off the trap was the same with $3\,\mu$s in all experiments, it cannot account for the increased damping and the increase of double Rydberg excitation probability with time. The only parameter varying with time in the experiment are the excitation pulses. One could argue that the excitation pulses might increase the atom loss probability, for instance due to off-resonant single-photon scattering. We verified that this is not the case however, by repeating the same experiments as in Figures 5.2 and 5.3, now with a detuning of $\delta = 100\,\mathrm{MHz}$. Here, we observed no change of the atom loss probability with the duration of the excitation pulse.

We now take a look at the blockade conditions. For the 3×3 trap array the distance between the traps is $a \simeq 3\,\mu$m, and the smallest pairwise interaction is about $12\,\mathrm{MHz}$ [Béguin *et al.*, 2013], much larger than the Rabi frequency $\Omega_1/2\pi = 1.5\,\mathrm{MHz}$, thus being well in the Rydberg blockade regime.

For the 19 trap array, the smallest calculated pairwise interaction is $V_{\mathrm{vdW}} \simeq 3\,\mathrm{MHz}$, only slightly larger than the single atom Rabi frequency $\Omega_1/2\pi = 1.1\,\mathrm{MHz}$. Nevertheless, solving the Schrödinger equation with the Hamiltonian given in Equation 6.1 gives double excitation probabilities below $5\,\%$.

If the assumption of an ideal two-level system with an interaction given by the effective van der Waals potential $V_{\mathrm{eff}}(\theta)$ were correct, the only other cause to observe population in the doubly excited states would be the detection efficiency ε. As we have seen in Figure 5.6, this is not enough to account for the double excitation probabilities observed in Figures 5.2 and 5.3.

The assumption of ε being the only source of double excitation events is further refuted if we look at *where* in the array the double excitations occur (see Figure 5.7). For this we take all the events, for all excitation times τ, where we detected *exactly* two excitation events, and sort them by the distance between the two excitations. We

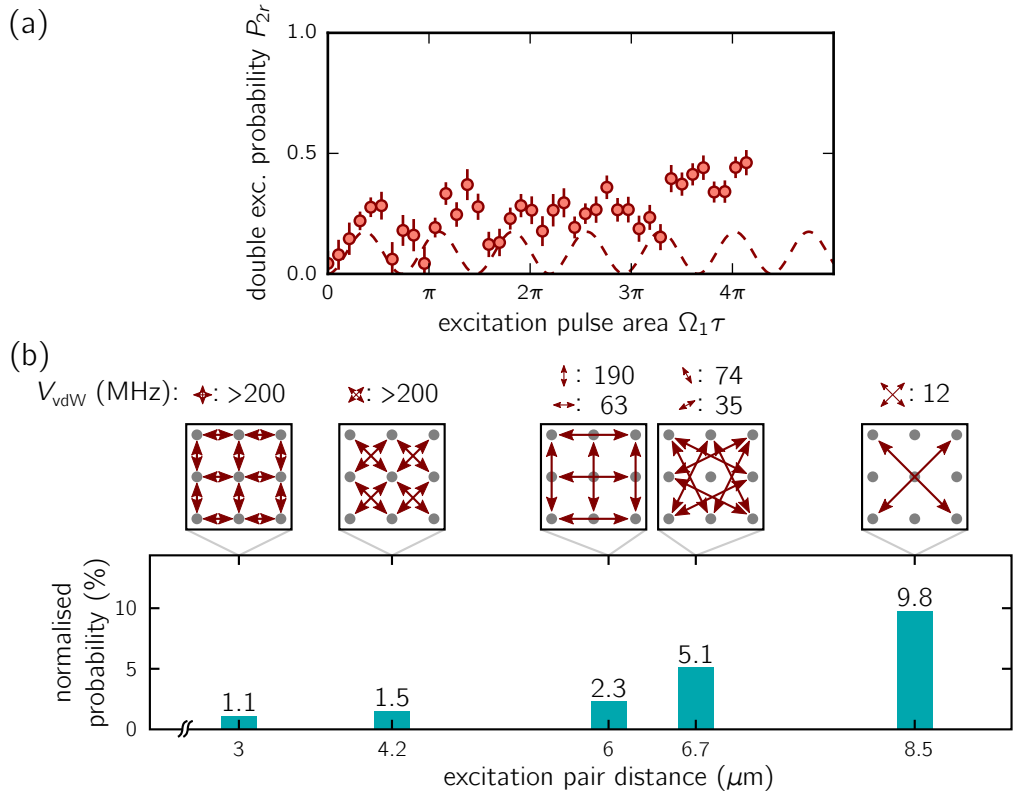

Figure 5.7: Spatial correlations of the double excitation events in the 3 × 3 array. (a) Detected probabilities of double excitations in a 3×3 atom array (red points), as shown in Figure 5.2. The dashed line shows the expected probability of detected double excitation for a perfect oscillation $P_{2r}(\tau) \simeq \varepsilon \cdot \sin(\sqrt{9}\Omega_1\tau/2)^2$, due to the finite detection efficiency $\varepsilon = 3\,\%$. (b) Normalised pair distance of the excitations. The histogram shows the probability to find the double excitation at a given distance, normalised by the number of configurations containing that distance, as indicated in the insets above the plot. The values above the distance plots give the respective calculated van der Waals interaction in MHz. For uncorrelated excitation pairs, all probabilities would be equal.

plot the relative occurrences of each Rydberg pair distance, normalised by the number of configurations containing the given distance. Thus, if the finite detection efficiency ε where the only cause for double excitations, all excitation distances would show up with equal probabilities. We notice however that this is not the case, and see a strong favouring of large separations of the excitation pair. Even if we consider the enhanced coupling strength to the singly excited state $\Omega_9 = \sqrt{9}\Omega_1 = 2\pi \times 4.5\,\mathrm{MHz}$, we should still be well blockaded, as confirmed by numerical simulations. Very similar behaviour is seen for all experiments with both the fully loaded 3×3 grid and the partially loaded 19 trap grid.

We thus believe that the assumed Rydberg-Rydberg interaction is slightly weaker than expected. This might be caused by the large number of interacting Zeeman sublevels [Vermersch, Glaetzle, and Zoller, 2015] of the Rydberg D states. For all atom pairs not aligned with the quantisation axis, all 16 pair state Zeeman sublevels are coupled together by the van der Waals interaction. For a large number of atoms, this may lead to a weak excitation of multiple-excitation states, and hence to a gradual increase of population of the Rydberg manifold. This assumption is supported by observations made in Rydberg D-state polaritons [Tresp *et al.*, 2015].

Another possible explanation might be the excitation of Rydberg molecules comprised of neighbouring Rydberg states, described by Derevianko *et al.* [2015]. However, for the molecular state to be resonant with the excitation laser, the distance between the atoms needs to be precise within a small fraction of a nanometer, which is unlikely to have happened just by chance on our experiments.

To gain a more quantitative insight into the effect of the large Zeeman manifold of the blockade will be an important task in view of future applications of the Rydberg blockade in quantum simulation and quantum computing experiments.

5.4 Conclusion

We have probed the collective enhancement of the Rabi oscillation between the ground state and a state with a single Rydberg excitation shared among all atoms, in the full Rydberg-blockaded regime. We observe well-contrasted, coherent collective oscillations, and measure the expected $\sqrt{N}$-scaling with the atom number N.

The double excitation probabilities seen in the experiments are larger than what can be explained by our false Rydberg detections. This may be due to an overestimation of the van der Waals interaction strength, although in previous experiments our calculated C_6 coefficients were well confirmed by the data [Béguin *et al.*, 2013; Barredo *et al.*, 2014]. Another explanation could be the weak coupling to Rydberg pair-states involving the various Zeeman sub-levels of the Rydberg D-states used in this experiment [Vermersch, Glaetzle, and Zoller, 2015], for atom pairs that are not aligned along the quantisation axis.

A further investigation of the efficiency of the Rydberg blockade is necessary in view of using the blockade in high-fidelity quantum-gate operations for quantum information protocols [Saffman, Walker, and Mølmer, 2010].

Chapter 6

Realisation of the Quantum Ising model in 1D and 2D arrays of Rydberg atoms

One aim of a quantum simulator is to give access to microscopic local observables, that can neither be accessed in the simulated material nor on a classical computer. In order for a particular quantum simulator to be credible, it needs to be benchmarked, which may be accomplished by various means. One can simulate a system with an analytically known behaviour, or compare the results of a quantum simulation on different systems. This is why realising a quantum simulator of a given Hamiltonian using different physical platforms is important. The promising results presented in the previous chapter thus motivated us to study the quantum Ising model on our experiment.

Here, we realise the Quantum Ising model on a system with between 8 and ~ 30 spins, and compare it to the numerical solution of the Schrödinger equation with the Quantum-Ising Hamiltonian whenever possible. For spin numbers $N > 15$, the numerical treatment of the full Hilbert space becomes difficult. The *ab initio* numerical simulation of our system was done by Tommaso Macrì from the Universidade Federal do Rio Grande do Norte, and International Institute of Physics (Brazil), based on a pseudo-spin 1/2 model with anisotropic, long-range interactions, and a finite Rydberg detection efficiency ε. In order to keep the numerical calculation tractable, we truncate the Hilbert space to a given maximum number of spin excitations. More details of the numerical simulations of this chapter can be found in the supplementary material in [Labuhn *et al.*, 2015].

We probe the Rydberg excitation dynamics for the case where the blockade radius extends between one and a few nearest neighbours, for various 1D and 2D geometries of atom arrays. Our apparatus allow the detection of the exact location of the Rydberg excitations, giving us direct access to the spatial correlations occurring in cold Rydberg media. The emergence of spatial correlations of Rydberg excitations in atomic media

due to their strong interactions has been suggested a decade ago [Robicheaux and Hernández, 2005]. The theoretical study of such Rydberg systems suggested that the spatial ordering undergoes phase transitions when changing the excitation laser parameters [Weimer *et al.*, 2008], even leading to a dynamic crystallisation of the Rydberg excitations [Pohl, Demler, and Lukin, 2010].

Those spatial correlations have since been indirectly observed experimentally, by looking at counting statistics and the temporal evolution of the total Rydberg excitation number [Viteau *et al.*, 2011; Dudin, Bariani, and Kuzmich, 2012; Schempp *et al.*, 2014; Urvoy *et al.*, 2015]. Only recently the spatial ordering has been observed directly by a spatially resolved detection of Rydberg atoms by field ionisation [Schwarzkopf, Sapiro, and Raithel, 2011], and on a quantum gas microscope [Schauss *et al.*, 2015], even allowing the adiabatic preparation of the crystalline[1] ground state [Schauss *et al.*, 2015].

Our new setup not only allows us to pinpoint the exact positions of the Rydberg excitation, but also lets us choose the initial ordering of the ground state atoms, in almost any arbitrary 2D geometry.

We can describe the internal dynamics of a system with N atoms with a ground state $|g\rangle$ and a Rydberg state $|g\rangle$, which are coupled by the Rabi frequency Ω, by the Hamiltonian

$$\hat{H} = \frac{\hbar\Omega}{2}\sum_{i}^{N}(\hat{\sigma}_{rg}^{(i)} + \hat{\sigma}_{gr}^{(i)}) + \sum_{i<j} V_{ij}\hat{\sigma}_{rr}^{(i)}\hat{\sigma}_{rr}^{(j)} + \hbar\delta\sum_{i}^{N}\hat{\sigma}_{rr}^{(j)}. \tag{6.1}$$

Here $\hat{\sigma}_{rg}^{(i)} = |g\rangle\langle r|$ and $\hat{\sigma}_{gr}^{(i)} = |r\rangle\langle g|$ are the transition operators between the ground and the Rydberg state of atom i, $\hat{\sigma}_{rr}^{(i)} = |r\rangle\langle r|$ the projection operator on the Rydberg state, $V_{ij} = C_6/|\boldsymbol{R}_i - \boldsymbol{R}_j|^6$ the van der Waals interaction between atoms i and j, and δ the detuning of the excitation lasers from the single atom resonance.

We can now introduce the two spin states $|\downarrow\rangle \equiv |g\rangle$ and $|\uparrow\rangle \equiv |r\rangle$. Following the spin-1/2 notation, we can map [Schauss *et al.*, 2015] the Hamiltonian in Eq. 6.1 to an Ising- type Hamiltonian of the form

$$\hat{H} = \frac{\hbar\Omega}{2}\sum_{i}^{N}\hat{\sigma}_{x}^{(i)} + \sum_{i,j,i\neq j}\frac{V_{ij}}{2}\hat{\sigma}_{z}^{(i)}\hat{\sigma}_{z}^{(j)} + \sum_{i}^{N}[B_i - \hbar\delta]\hat{\sigma}_{z}^{(j)}, \tag{6.2}$$

with $\hat{\sigma}_{\alpha}^{(j)}$ $(\alpha = x, y, z)$ being the Pauli spin matrices and $B_i = \sum_{j,j\neq i} V_{ij}/2$. The

[1] However, as recent pre-print rebuts the claim of a true crystalline state [Petrosyan, Mølmer, and Fleischhauer, 2015]

first and the last term of the Hamiltonian describe a transverse and a longitudinal magnetic field respectively. There is a large interest in such Ising-type Hamiltonians both theoretically [Weimer *et al.*, 2008; Weimer and Büchler, 2010; Lesanovsky, 2011] and experimentally [Richerme *et al.*, 2014; Jurcevic *et al.*, 2014; Schauss *et al.*, 2015]. On our experiment, we can realise such a Hamiltonian by simply shining the Rydberg excitation light on an array of ground state atoms, with a given single atom Rabi frequency Ω and detuning δ from the single atom resonance.

In all of the results presented in this chapter, we choose $\delta = 0$. The spin-Hamiltonian thus simplifies to

$$\hat{H} = \frac{\hbar\Omega}{2} \sum_{i}^{N} \hat{\sigma}_x^{(i)} + \sum_{i<j} V_{ij} \hat{n}^{(i)} \hat{n}^{(j)}, \tag{6.3}$$

with $\hat{n} = (\mathbb{1} + \hat{\sigma}_z)/2$ counting the number of Rydberg excitations on a given site, being either 0 or 1. The spin-spin coupling is given by the van der Waals interaction $V_{ij} = C_6(\theta)/|\boldsymbol{R}_i - \boldsymbol{R}_j|^6$ between atoms i and j is anisotropic, as we are still using Rydberg D-states (see Section 5.1).

6.1 A ring of 8 atoms

We first probe the spatial correlations and dynamics of Rydberg excitations on a system consisting of eight atoms arranged on a ring. This relatively small system size allows us to prepare the ring in a deterministic way, so that we can generate an eight-trap pattern, and trigger the experiment as soon as all the traps are filled[2]. Furthermore, we can still numerically solve the time-dependent Schrödinger equation with the Hamiltonian of Equation 6.3 with the full Hilbert space including all 256 basis states. Despite the anisotropy of the van der Waals interaction of the Rydberg D-states, we assume translational invariance along the ring, thus realising a quasi-1D spin chain with periodic boundary conditions.

We can easily investigate different regimes of the range of the blockade radius by either tuning the interatomic spacing a in the ring, or the blockade radius R_b via the C_6 coefficient by changing the principal quantum number of the used Rydberg state. Intuitively, we expect independent Rabi oscillations if $R_\mathrm{b} < a$, a Rabi oscillation to a state with a collective single excitation with an enhanced Rabi frequency if R_b exceeds the system size as seen in Chapter 5, and a more complicated behaviour for $R_\mathrm{b} \approx a$.

[2] This way, the full data acquisition for the intermediate blockade regime in Figure 6.1(b) took about 24 hours.

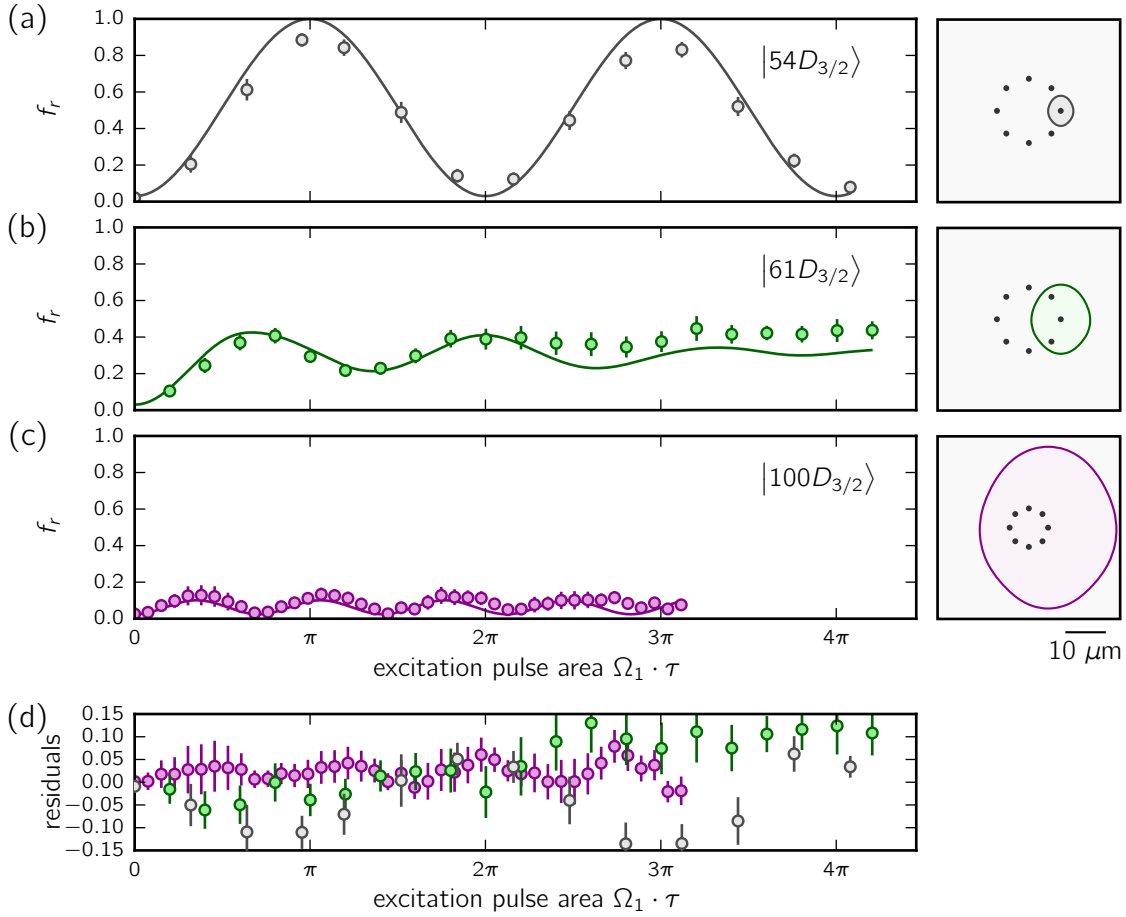

Figure 6.1: Rydberg excitation dynamics for an 8 atom ring. We probe the temporal evolution of the Rydberg fraction f_r for three different regimes of the blockade radius R_b, and compare it to the solution of the Schrödinger equation with the quantum Ising Hamiltonian of Equation 6.3 including a finite detection efficiency $\varepsilon = 3\,\%$ (solid lines). The sketches on the right show the positions of the atoms and the respective radii. (a) For R_b smaller than the atomic separation a the atoms behave independently, and each atom oscillates between the ground and Rydberg state with the single atom Rabi frequency Ω_1. (b) For $R_b \simeq 1.5a$ the Rydberg fraction shows a damping which we attribute to the beating of several incommensurate frequencies of the interacting system. (c) For R_b larger than the trap array, multiple Rydberg excitations are blockaded, and f_r oscillates between 0 and 1/8 with a frequency $\sqrt{8}\Omega_1$. (d) Residuals between the data points and the model.

Table 6.1: Experimental parameters used for the experiments. Parameters of the three different experiments shown in Figure 6.1).

	trap array parameters		Rydberg state parameters				
interaction regime of Figure 6.1	spacing a (μm)	N_{at}	n	calculated C_6/h (GHz μm^6)	$\Omega_1/(2\pi)$ (MHz)	R_b (μm)	α
independent (a)	6.3	8	54	6.7×10^3	1.6	4	0.63
intermediate (b)	6.3	8	61	7.6×10^5	1.3	9.1	1.4
fully loaded (c)	3.8	8	100	8.0×10^7	0.95	21	5.5

We experimentally realise these three regimes by choosing the experimental parameters given in Table 6.1. We probe the global excitation dynamics by measuring the Rydberg fraction f_r, i.e. the average number of Rydberg excitations divided by the total number of atoms N. In the non-interacting regime, with $R_b < a$, the atoms behave independently of each other, and thus each atom will undergo Rabi oscillations between $|g\rangle$ and $|r\rangle$ with the same single atom Rabi frequency[3] Ω_1. Thus also the Rydberg fraction oscillates between 0 and 1 with frequency Ω_1, as seen in Figure 6.1(a). The deviation from the expected f_r, plotted in Figure 6.1(d), stems from the finite Rydberg excitation efficiency.

For the other extreme case, the blockade radius R_b being larger than the system size, we use the Rydberg state to $n = 100$, and reduce the interatomic spacing to $a = 3.8\,\mu$m, yielding a calculated $R_b \simeq 21\,\mu$m with an $\Omega_1 = 2\pi \times 0.95\,$MHz. All the atoms are now pairwise blockaded, leading to an oscillation of the system between the collective ground state and a strongly correlated state, with a single excitation symmetrically shared among all eight atoms. Equivalent to the results presented in Chapter 5, the Rydberg fraction now oscillates with an enhanced frequency $\sqrt{8}\Omega_1$ between 0 and 1/8, as shown in Figure 6.1(c).

In the intermediate regime, where the blockade radius is comparable to the interatomic spacings, the dynamics becomes less intuitive. We now chose $n = 62$, giving a calculated $R_b = 9.1\,\mu$m with an $\Omega_1 = 2\pi \times 1.3\,$MHz, and again taking an interatomic spacing of $a = 6.3\,\mu$m. We expect a ratio $\alpha = R_b/a \simeq 1.4$, so nearest neighbour excitations should now be blockaded, whereas next-nearest neighbours only show a van der Waals interaction strength of about 0.26 MHz and should behave nearly independently. The observed dynamics of the Rydberg fraction in shown in

[3] We have measured the Rabi frequencies to be equal within 4 % along the ring.

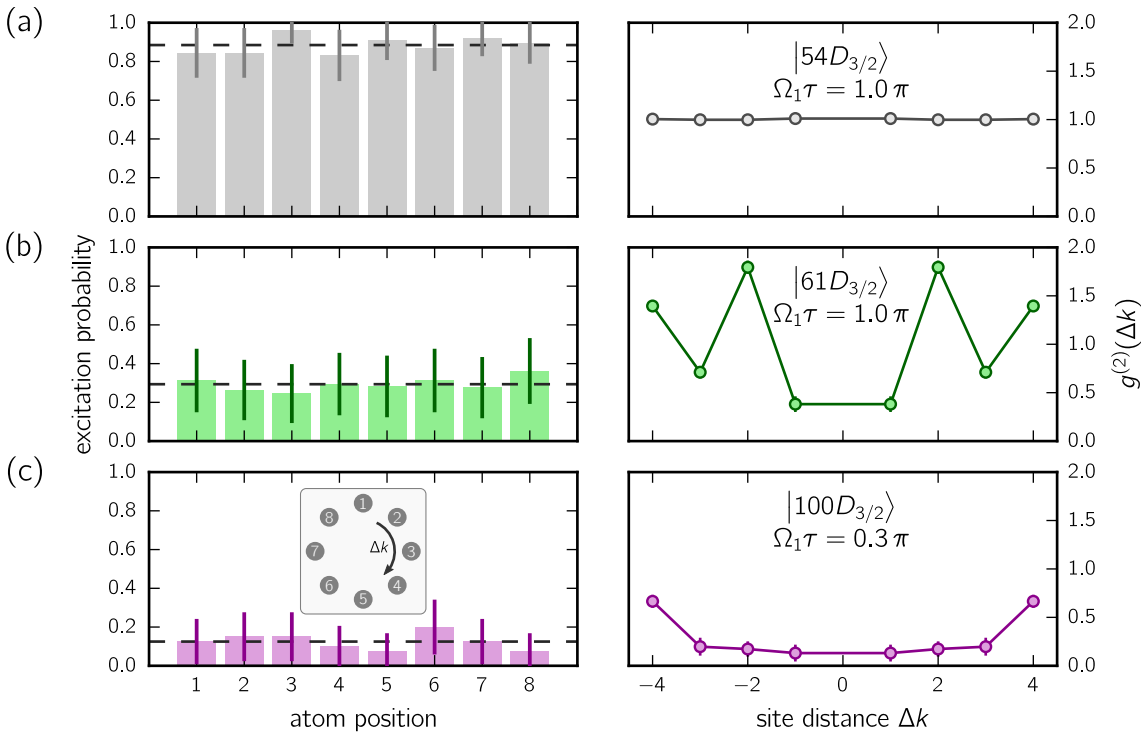

Figure 6.2: Site-resolved Rydberg excitation probability. The single-site resolved mean Rydberg excitation probabilities (left), and the pair correlation function $g^{(2)}(\Delta k)$ (right), for the data shown in Figure 6.1, with (a) $\alpha \simeq 0.63$, (b) $\alpha \simeq 1.4$, and (c) $\alpha \simeq 5.5$, for excitation times given in the right panels. The excitation probabilities are homogeneous among all sites within the error bars. The dashed lines in the left panels show the respective means, the solid lines in the right panels are guides to the eye. The site numbering is shown in the inset in (c).

Figure 6.1(b). It shows the beating of the incommensurate frequencies of the several resonantly or near-resonantly coupled eigenstates of the system, which looks as an effective damping (for long excitation times, the simulation does show a revival of the oscillation). We again compare the data to the full numerical solution of the Schrödinger equation of the spin-1/2 model of Equation 6.3, including an $\varepsilon = 3\,\%$. The measured data values agree quite well with the model. Only for the second half of the dataset, with excitation pulse areas $> 2\pi$, they start to deviate. This might be a sign of the limits of the simple two level model for our D-state Rydberg atoms, especially since the interacting atom pairs are not aligned with the quantisation axis, thus possibly leading to more involved interaction dynamics, as described in the previous chapter.

We see that we can easily vary the interaction regime of the system by strongly

tuning $\alpha = R_\mathrm{b}/a$, the important parameter in this kind of experiment, by almost one order of magnitude, from a non-interacting $\alpha = 0.6$ to $\alpha = 5.5$.

As we measure the *atom resolved* Rydberg excitation probability, we can directly probe the spatial Rydberg-Rydberg pairs correlations. Due to the anisotropy of the interaction the system is not rotationally invariant. However, the important parameter here is not the interaction strength directly, but the blockade radius R_b. As the range of the blockade of the varies very little along the ring, we expected the system to behave translationally invariant. This assumption is supported by the mean Rydberg excitation probability per site, shown in Figure 6.2, for all three values of α presented above. We measure an excitation probabilities which are homogeneous on all sites within the error bars (the same holds true for other excitation times, which are not shown here).

A structured excitation pattern only becomes visible when computing the Rydberg-Rydberg pair correlation function

$$g^{(2)}(\Delta k, t) = \frac{1}{N_\mathrm{traps}} \sum_i \frac{\langle n_i(t) n_{i+\Delta k}(t)\rangle}{\langle n_i(t)\rangle \langle n_{i+\Delta k}(t)\rangle}, \tag{6.4}$$

averaged over all sites Here, $n_i(t)$ is the Rydberg excitation probability of a ground state atom at site i, for an excitation time t. The results are shown in the right panels of Figure 6.2, for the same excitation times as in the site-resolved excitation probabilities.

In the non-interacting regime with $\alpha \simeq 0.63$, we as expected do not see any correlations of the Rydberg excitations, as all atoms behave independently, showing nearest neighbour interactions of only $V_\mathrm{vdW} \simeq h \times 0.1\,\mathrm{MHz}$.

In the intermediate regime with $\alpha \simeq 1.4$, we see strong antiferromagnetic-like or crystal-like correlations, with a strong suppression of nearest neighbour excitations ($\Delta k = \pm 1$), and a nearly doubled excitation probability for next-nearest neighbours pairs ($\Delta k = \pm 2$).

In the fully blockaded regime with $\alpha \simeq 5.5$, we again expect a completely flat correlation function if the assumption of perfect blockade holds true, as there should always be at most one single excitation present in the system. The false Rydberg detection probability ε should only lead to a global offset from zero, as ε was measured to be equal among all site. However, we notice an increase of $g^{(2)}$ at $\Delta k = \pm 4$, i.e. for Rydberg pairs created at opposing sites of the ring. This means that for the occurrence of double Rydberg excitations, the excitations arrange themselves as far apart as possible. The occurrence of double excitation in the system is surprising, as even the

smallest calculated effective interaction strength in the system is $V_{eff} \gtrsim h \times 20\,\mathrm{MHz}$. Again this might hint that the effective interaction strength might be an over-simplified model.

We finally compare the measured pair correlation function $g^{(2)}(\Delta k, \Omega\tau)$ for the intermediate regime of $\alpha \simeq 1.4$ with that obtained from the solution of the Schrödinger with the quantum Ising model of Equation 6.3, including the anisotropic interaction, with and without including ε. In order to take into account a false positive detection probability of $\varepsilon = 3\,\%$, a standard Monte-Carlo algorithm was run, 'exciting' each ground state atom to the Rydberg state with a probability obtained from the solution of the time dynamics of the Schrödinger equation. The remaining ground state atoms are then converted to 'Rydberg' atoms with a probability $\varepsilon = 3\,\%$.

As the Rydberg fraction f_r in Figure 6.1(b) starts to deviate from the model for $\Omega_1\tau \gtrsim 2\pi$, we also expect the correlation function to show the 'correct' behaviour of a true spin-1/2 system only up to this point. The results for excitation pulse areas between 0.2π and 4.2π are shown in Figure 6.3. Overall we notice that the false detection probability ε only leads to a small reduction of the contrast of the pair correlations. For small excitation pulse areas of up to $\Omega_1\tau \simeq 1\pi$ we see a remarkable agreement between the data and the theory, except for the shortest excitation pulse of 0.2π, where the Rydberg excitation probability of multiple atoms is still too low to have sufficient events for the calculation of $g^{(2)}$. For excitation pulse areas between 1π and 2π the data no longer follows the model exactly, but the same pattern of the correlation is still visible. Only for excitation times larger than 2π the disagreement becomes more pronounced. Most notably the suppression of next-nearest neighbours weakens significantly, again suggesting that the idea of the effective van der Waals potential in Equation 5.7 to model the angular dependence of the interaction begins to fail. We attribute this deviation to the Zeeman structure of Rydberg D-states, which is not taken into account in our spin-1/2 model. It may lead to a reduced Rydberg-Rydberg interaction due to the van der Waals interaction coupling to other Zeeman sublevels for $\theta \neq 0$, i.e. atomic pairs not aligned along the quantisation axis, yielding a decreased efficiency of the Rydberg blockade, as we have already observed in Chapter 5.

To understand the origin of these increasing deviation from the model, we look at the time evolution of $g^{(2)}$ for each value of Δk separately. We see in Figure 6.4 that for all Δk the correlations oscillate with time. This is due to the still relatively small system size, which does not conceal the coherent nature of the Rydberg excitation. For $\Delta k = 1$ there is a roughly linear increase of $g^{(2)}$ on top of the oscillating behaviour.

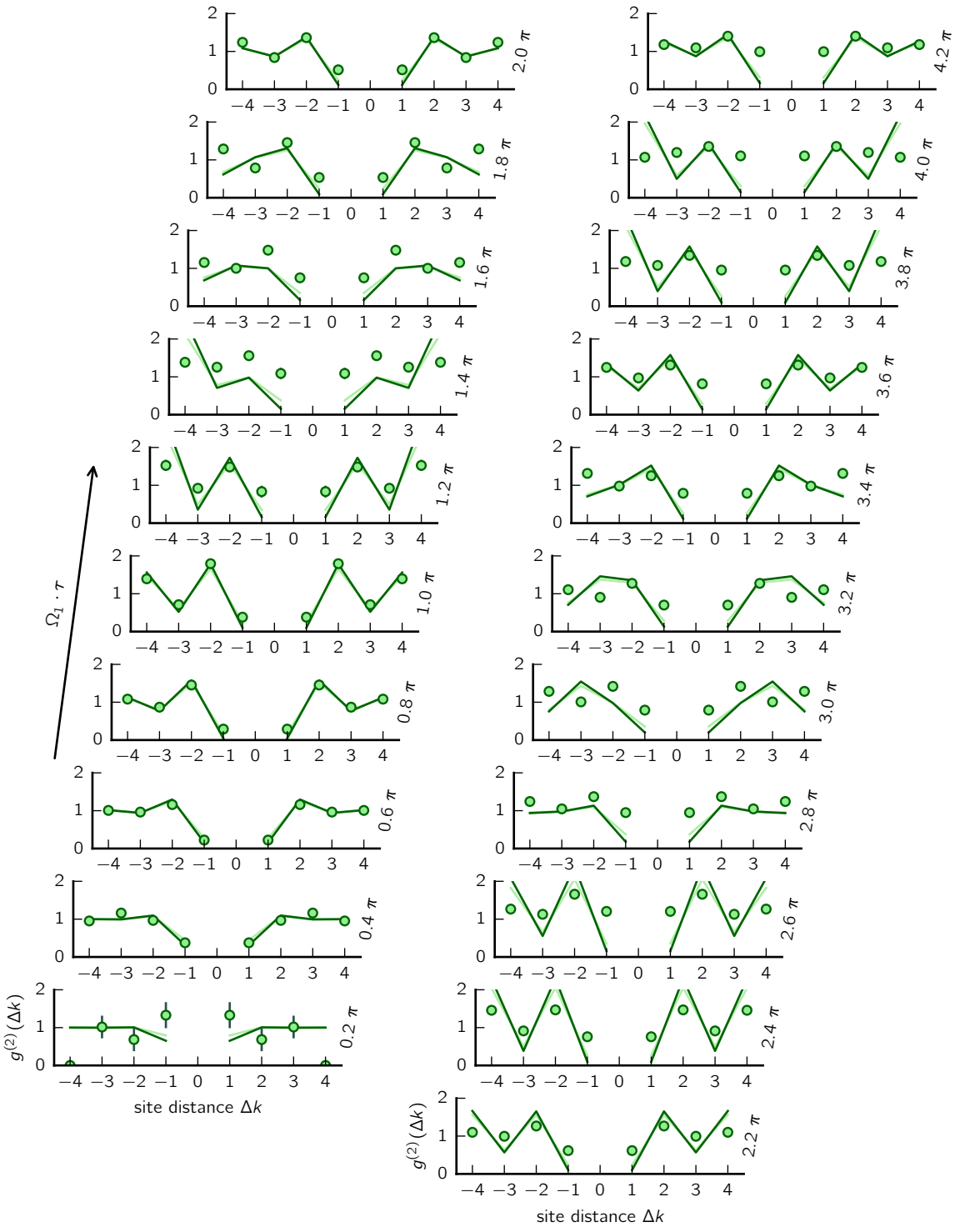

Figure 6.3: The Rydberg-Rydberg pair correlation function for the 8 atom ring. We compare the measured Rydberg-Rydberg pair correlation function to the correlations obtained from the spin-1/2 model, for the parameters of Figure 6.1(b), as a function of the excitation pulse length $\Omega_1\tau$. The solid lines are obtained by numerically solving the time-dependent Schrödinger equation with the Hamiltonian of Equation 6.3, for perfect detection (dark green), and including a detection error of $\varepsilon = 3\,\%$ (light green).

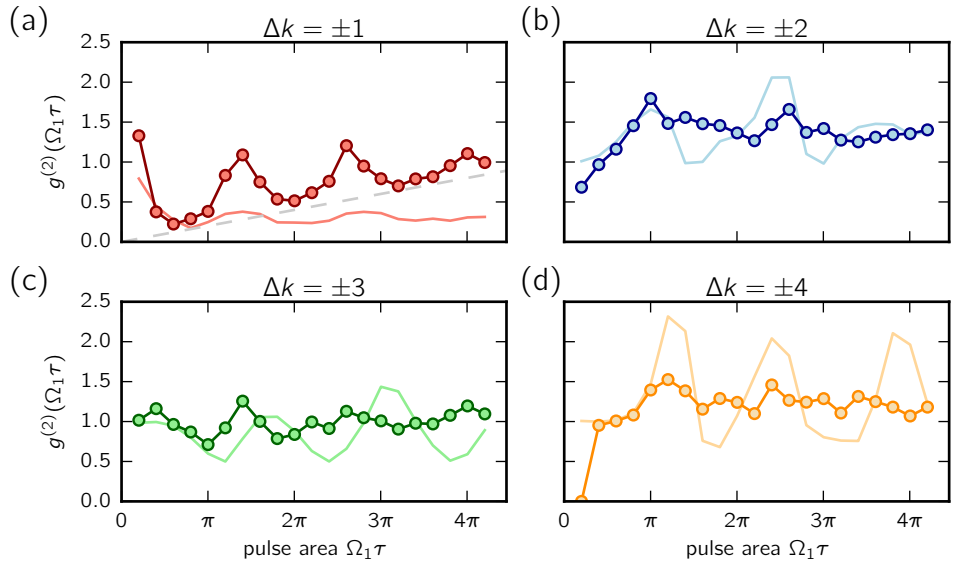

Figure 6.4: Time evolution of the pair-correlations. We show $g^{(2)}(\tau)$ for Δk ranging from ± 1 to ± 4 (a to b). Due to the coherent coupling and the still relatively small system size $g^{(2)}$ oscillates with the excitation time. For $\Delta k = \pm 1$ the pair correlations increase with time. The dashed grey line in (a) shows a slope of $0.2/\pi$.

This observation supports the assumption of an imperfect Rydberg blockade, since even for an interatomic axis perpendicular to the quantisation axis the nearest-neighbour interaction is still $V_{\mathrm{vdW}}(\theta = 90°) \simeq h \times 4.9\,\mathrm{MHz}$, sufficiently larger than the Rabi frequency $\Omega_1 = 2\pi \times 1.3\,\mathrm{MHz}$, thus nearest neighbour excitations should still be blockaded.

As a possible extension to the experiment presented here, one could perform a sweep of the laser detuning and Rabi frequency as demonstrated by Schauss *et al.* [2015]. If the translational invariance holds true, then due to the periodic boundary conditions and the even atom number one could adiabatically follow the ground state of the system to reach the antiferromagnetic state, producing a state of the form

$$|\Psi_{\mathrm{af}}\rangle = \frac{|\uparrow\downarrow\uparrow\downarrow\uparrow\downarrow\uparrow\downarrow\rangle + |\downarrow\uparrow\downarrow\uparrow\downarrow\uparrow\downarrow\uparrow\rangle}{\sqrt{2}}. \tag{6.5}$$

After local rotations this state is equivalent to the GHZ state [Greenberger, Horne, and Zeilinger, 1989]

$$|\mathrm{GHZ}\rangle = \frac{|\uparrow\downarrow\uparrow\downarrow\uparrow\downarrow\uparrow\downarrow\rangle + |\downarrow\uparrow\downarrow\uparrow\downarrow\uparrow\downarrow\uparrow\rangle}{\sqrt{2}}. \tag{6.6}$$

We measure an overlap of the experimentally produced state after an excitation pulse of $\Omega_1\tau = 1.0\pi$ with the antiferromagnetic state of $|\langle\Psi_{\mathrm{af}}|\Psi_{\mathrm{exp}}(1.0\pi)\rangle|^2 = 0.4$.

6.2 Partially filled quasi-1D array

In the previous section we have probed the Rydberg-Rydberg pair correlations of eight atoms arranged along a fully loaded ring. In the intermediate regime of the interaction we observed strong correlations of the Rydberg excitations, which for excitation times up to $\Omega_1\tau \simeq 1\pi$ is very well described by a quantum-Ising type Hamiltonian. We attribute the increasing deviation from the model for longer excitation times to a more complex interaction mechanism for atom pairs whose interatomic axis is not aligned with the quantisation axis.

We therefore modify the trap geometry to a 'racetrack'-shaped array of $N_{\mathrm{t}} = 30$ traps, as shown in Figure 6.5(a). We chose this geometry to (i) have as many atom-pairs as possible aligned along the quantisation axis while keeping a quasi-1D chain with periodic boundary conditions, and (ii) to have Rabi frequencies as homogeneous as possible throughout the array, where the main constraint is the finite extent of the the 474 nm excitation laser along the y-axis.

With our stochastic trap loading we cannot wait until all traps in the array are filled with a single atom. However, as explained in Section 4.1, we can monitor the state of each trap in real time, allowing us to trigger the experiment on a minimum number of present atoms. In order to nevertheless improve the atom number statistics in the experiment from a binomial distribution centred around $N_{\mathrm{t}}/2 = 15$ atoms, we set the trigger condition for the experiment to the presence of ≥ 20 atoms, yielding a short experimental cycle time of $\approx 2.5\,\mathrm{s}$. Figure 6.5(b) shows the thereby obtained atom number distribution. We observe a narrow distribution centred around 20 atoms, corresponding to a filling fraction of 67 %. We do not always obtain 20 atoms in the initial atom configuration, since there is a finite probability for trap to lose or catch an atom between the triggering frame and the initial frame, as explained in Section 4.1.1. For very slow trap loading rates, we would observe an atom number distribution with a sharp peak at $N = 20$ atoms. In the data presented in this section, we chose *not to* post-select on the atom number.

In order to observe strong Rydberg pair correlations despite the partial loading, we now use the $\left|79D_{3/2}\right\rangle$ Rydberg state, with a calculated $C_6/h = 6.0 \times 10^6\,\mathrm{GHz}\,\mu\mathrm{m}^6$. Using a single atom Rabi frequency $\Omega_1 \simeq 2\pi \times 1.0\,\mathrm{MHz}$, we expect a blockade radius of $R_{\mathrm{b}} \simeq 13.5\,\mu\mathrm{m}$. Compared to the lattice spacing $a = 3.1\,\mu\mathrm{m}$, we obtain a ratio

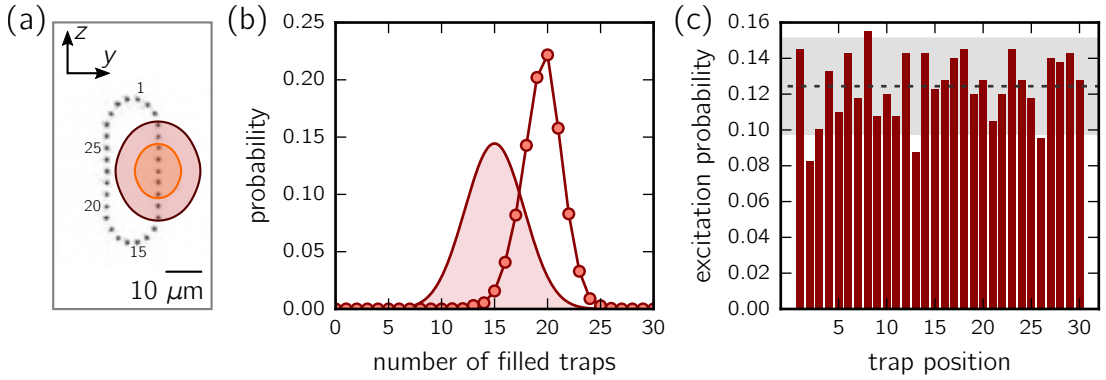

Figure 6.5: Parameters of the partially loaded Racetrack-like trap array. (a) CCD image of the trap intensities, with an inter-trap distance $a = 3.1\,\mu$m. The numbers indicate the site labelling, the shaded areas the blockade radii of $R_b \simeq 13.5\,\mu$m for the $|79D_{3/2}\rangle$ (red) and $R_b \simeq 7.4\,\mu$m for the $|57D_{3/2}\rangle$ (orange) state. The array has an extent along the y-axis of $14\,\mu$m compared to the $1/e^2$-radius of the blue excitation beam of $w_B^{(y)} = 47\,\mu$m, and an extent along the z-axis of $39\,\mu$m compared to $w_R^{(z)} = 230\,\mu$m of the red beam. (b) The experiment is triggered by the presence of $N \geq 20$ atoms in the 30 traps. The points show the relative occurrences of obtained number of ground state atoms in the initial atom configurations. The shaded area shows the expected distribution for random triggering. (c) Site dependent excitation probability of a ground state atom to the $|79D_{3/2}\rangle$ state, for an excitation time $\Omega_1\tau = 0.64\pi$. The dashed line gives the mean excitation probability, the shaded grey area the statistical uncertainty.

$\alpha = R_b/a \simeq 4.3$, which should be sufficient to observe strong correlation even for a half-filling of the traps.

Along the racetrack, the measured light shifts seen by the atoms due to variations the excitation light intensity differ by less than 0.06 % of the mean Rabi frequency Ω_1, the Rabi frequencies by less than 0.09 %. We measure again the site-resolved excitation probability for a present single atom, for an excitation time of $\Omega_1\tau = 0.64\pi$, shown in Figure 6.5(c). Almost all excitation probabilities are equal within the error bars. Due to the limited sample size, exciting on average ~ 3.7 out of the 20 atoms, for 400 realisations at $\Omega_1\tau = 0.64\pi$, the statistical uncertainty is relatively large.

The measured Rydberg fraction f_r as a function of excitation time is shown in Figure 6.6(a). We observe initial oscillations which are damped out for longer excitation times. We compare the data to the theoretical expected dynamics of the Rydberg fraction, obtained by again numerically solving the Schrödinger equation for the spin-1/2 Hamiltonian of Equation 6.3 and including an $\varepsilon = 3\,\%$ for all sites. The agreement between the model and the experimentally observed dynamics is remarkable,

with the residuals (see Figure 6.6(b)) smaller than ± 0.02.

We again compute the experimentally observed, time dependent Rydberg-Rydberg pair correlation function given in Equation 6.4, here with Δk being the absolute site distance in either direction. In the case of a partially loaded array, both n_i and $n_{i+\Delta k}$ are computed from only those experiments where a ground state atom is present in the initial atom configuration both at site (i) and at site $(i + \Delta k)$ at the same time. The result is shown in Figure 6.6(c). We see a strong suppression of $g^{(2)}(\Delta k)$ for short distances $\Delta k \leq 3$. The correlations emerge already at very short times, after which they show some small dynamics, but reach a quasi-steady state after $\Omega_1 \tau \approx 2\pi$.

To further assess the validity of the spin-1/2 model in this system, we want to again compare the measured pair correlations to the ones obtained from the model. For the calculation, carried out by Tommaso Macrì, the Schrödinger equation for the Hamiltonian of Equation 6.3 was solved numerically. The pair correlation function was computed for various random initial ground state distribution according to the ones observed experimentally. After several hundred realisations the computed pair correlation function is well converged.

The comparison between data and theory, shown in Figure 6.7 for a selection of excitation times, shows a remarkably good agreement. Also the apparently high value of $g^{(2)}$ for small Δk is reproduced by the theory. For these small distances $\Delta k < \alpha$, the small ε actually has a strong influence on the correlation function. In case of perfect blockade, i.e. $\varepsilon = 0$, $g^{(2)} = 0$ for small distances. Including a finite ε modifies the pair correlation computed with Equation 6.4 in the following way. To lowest order in ε, the numerator $\langle n_i n_{i+\Delta k} \rangle$ gives a non-zero value in the blockaded regime only if atom i is in the Rydberg state (with a probability f_r), and atom $i + \Delta k$ is lost as a ground state atom (with probability $\varepsilon = 3\,\%$), or vice versa, giving $2\varepsilon f_r$. The denominator $\langle n_i \rangle \langle n_{i+\Delta k} \rangle$ gives f_r^2, thus yielding a $g^{(2)} \simeq 2\varepsilon / f_r$, which experimentally can be as large as 0.5. Our observations show that the interaction induces spatial correlations in the system on a length scale R_b. The damped quasi-oscillatory behaviour of $g^{(2)}$ is typical of a that of a liquid. It has also been observed in Rydberg excitations on a 2D optical lattice Schauss *et al.* [2015].

The improved agreement to the spin-1/2 model compared to the eight-atom ring presented in the last section is likely due to the fact that many atom pairs are aligned along the quantisation axis, and only a single excitation in the 'bend' of the racetrack is allowed at the same time, thus making the effects of the anisotropy small.

In order to intentionally increase the effect of the anisotropy by allowing several excitations in the bend, we would ideally increase the lattice spacing by factor

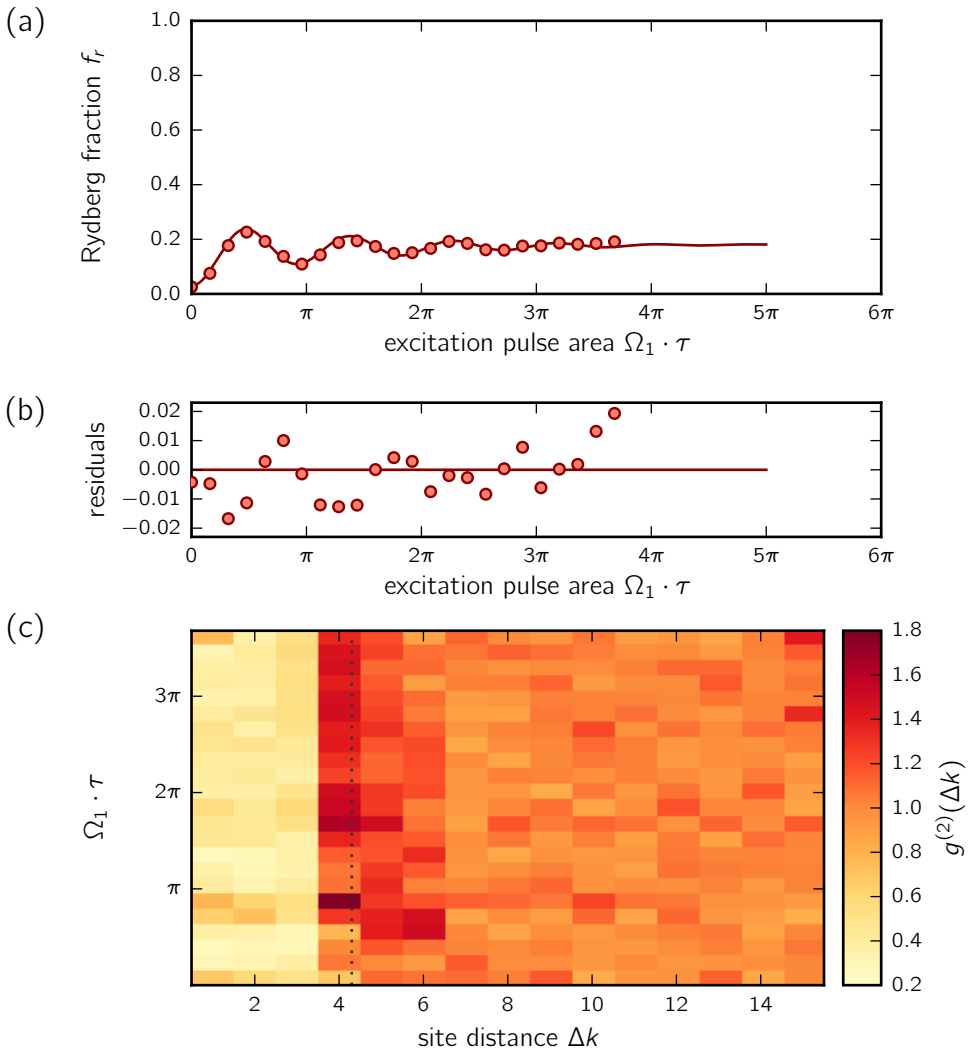

Figure 6.6: Excitation dynamics and correlations for large α. (a) The Rydberg excitation fraction in the racetrack for the $|79D_{3/2}\rangle$ Rydberg state (circles) and the numerical calculation using the spin-1/2 model (solid line), taking into account a false detection probability of $\varepsilon = 3\,\%$. (b) The residuals between the data and the model (error bars are smaller than the symbol size). (c) The Rydberg-Rydberg pair correlation $g^{(2)}(\Delta k)$ of Equation 6.4, the dotted line indicates $R_b(\theta = 0)$. The dynamics seems to reach a quasi-steady state after $\Omega_1 \tau \approx 2\pi$.

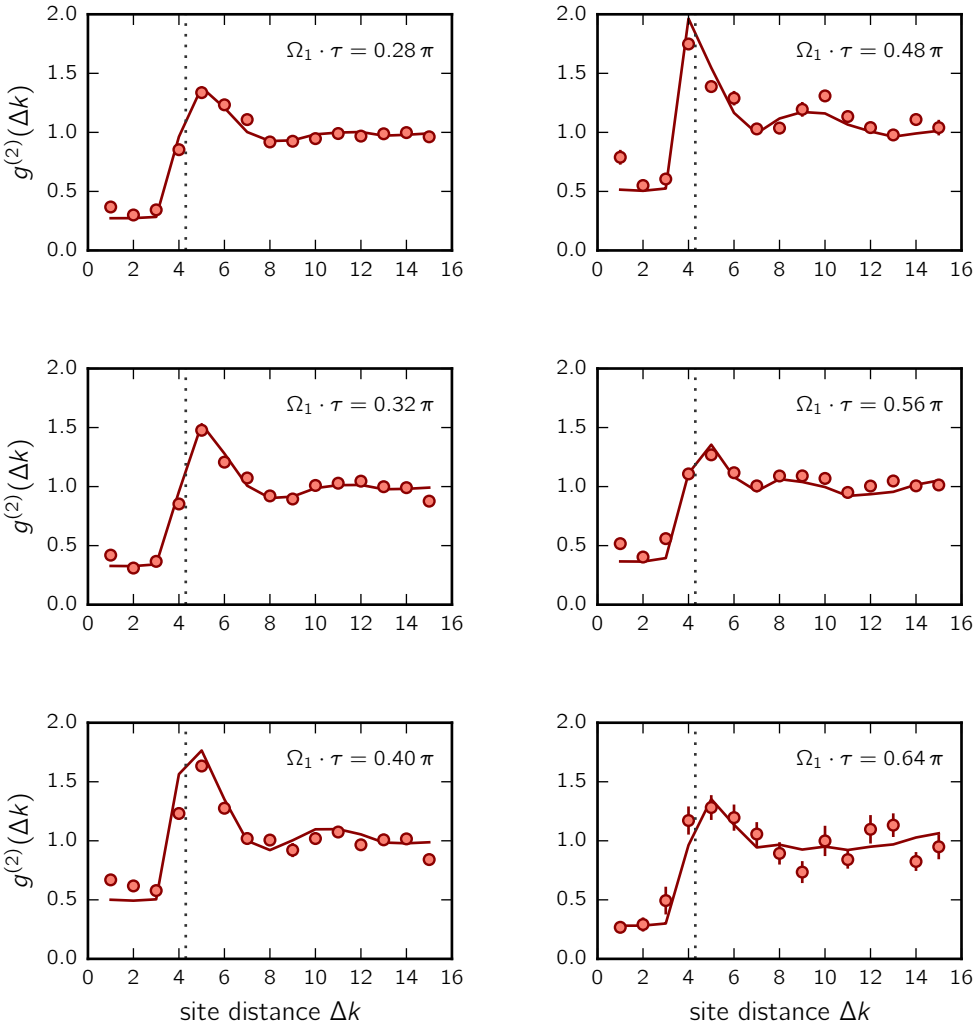

Figure 6.7: Comparison of the measured pair correlations to the spin-1/2 model. We compare, for a selection of excitation times, the measured Rydberg-Rydberg pair correlations for the $|79D_{3/2}\rangle$ state of Figure 6.6, with the numerically obtained pair correlations of the spin-1/2 model, taking into account a false detection probability of $\varepsilon = 3\,\%$. The dashed line indicates $\alpha = 4.3$.

~ 2. Unfortunately this is unpractical for us, since then the array size would be comparable to the spatial extend of the excitation lasers, and Rabi frequencies would vary significantly among the trap sites. We therefore keep the array size fixed, and reduce the blockade radius R_b instead, by reducing the principal quantum number to $n = 57$. With $\Omega_1 \simeq 2\pi \times 1.7\,\mathrm{MHz}$ and a calculated $C_6/h = 2.7 \times 10^5\,\mathrm{MHz}\,\mu\mathrm{m}^6$, we get $R_\mathrm{b} = 7.4\,\mu\mathrm{m}$, giving $\alpha = 2.4$. As before, we again trigger on the presence of 20 atoms in the 30 traps.

We perform the same experiment as before with the $n = 79$ state, shown in Figure 6.8. Until an excitation time of $\Omega_1\tau \approx 1\pi$ the Rydberg fraction f_r follows the course predicted by the spin-1/2 model. For longer excitation times, the measured Rydberg fraction lies systematically above the calculated curve, meaning that we again measure more Rydberg excitations than predicted by the model. Finally, the pair correlations $g^{(2)}$ for the $\left|57D_{3/2}\right\rangle$ state as a function of excitation time is shown in Figure 6.8(b). The contrast is reduced compared to the previously presented one, and again a quasi-steady state seems to be reached after a time $\Omega_1\tau \approx 2\pi$. A numerical calculation of $g^{(2)}$ has not been carried our so far, as the Hilbert space is now significantly larger compared to the racetrack with the $n = 79$ Rydberg state, due to the increased number of possible Rydberg excitations in the system. While the calculation of f_r is still relatively simple by solving once the time dependent Schrödinger Equation, the calculation of $g^{(2)}$ including the finite ε in Monte-Carlo simulation requiring ~ 100 realisation to converge, becomes much more involved.

We have seen a clear distinction between the two realisations of the experiment. For the larger $\alpha = 4.3$ the agreement with the spin-1/2 model is exceptional, whereas with a smaller $\alpha = 2.4$ a deviation of the Rydberg fraction from the model becomes quickly visible. Which we attribute to a more pronounced influence of the anisotropy when decreasing α.

6.3 Partially filled 7x7 square lattice

In the previous section we investigated the Rydberg-Rydberg pair correlations along a partially loaded, quasi-1D chain of 30 traps with periodic boundary conditions. When comparing the experimental results to the spin-1/2 model of Equation 6.3, we observe an excellent agreement for $\alpha = R_\mathrm{b}/a = 4.3$, whereas for $\alpha = 2.4$ we notice an increasing discrepancy of the Rydberg fraction for larger excitation times, which may be caused by a larger influence of the anisotropy of the interaction for atomic pairs not aligned with the quantisation axis.

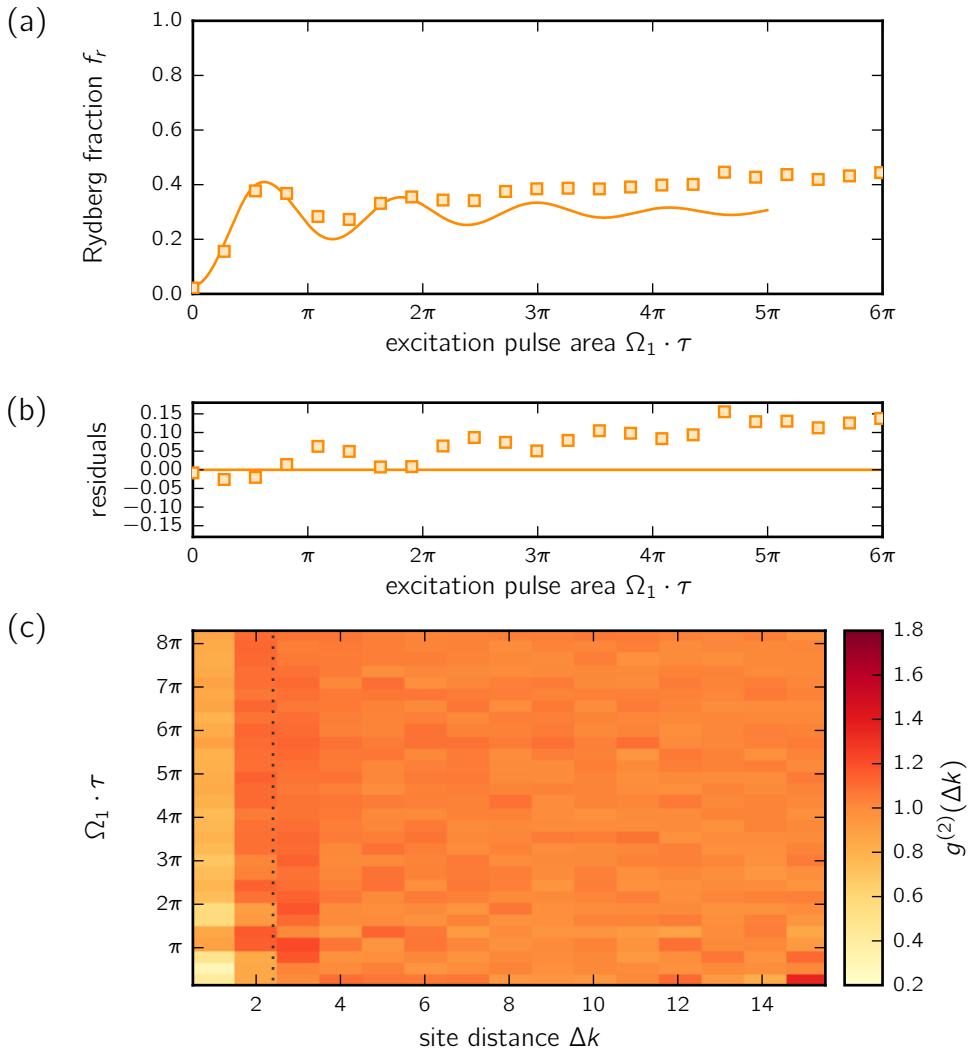

Figure 6.8: Excitation dynamics and correlations for small α. (a) The Rydberg excitation fraction in the racetrack for the $|57D_{3/2}\rangle$ Rydberg state (squares) and the numerical calculation using the spin-1/2 model (solid line), taking into account a false detection probability of $\varepsilon = 3\,\%$. (b) The residuals between the data and the model. (c) The Rydberg-Rydberg pair correlation $g^{(2)}(\Delta k)$ of Equation 6.4, the dotted line indicates $R_b(\theta = 0)$. Compared to the experiment with large α the correlation function is less contrasted, but also seems to reach a quasi-steady state after $\Omega_1 \tau \approx 2\pi$.

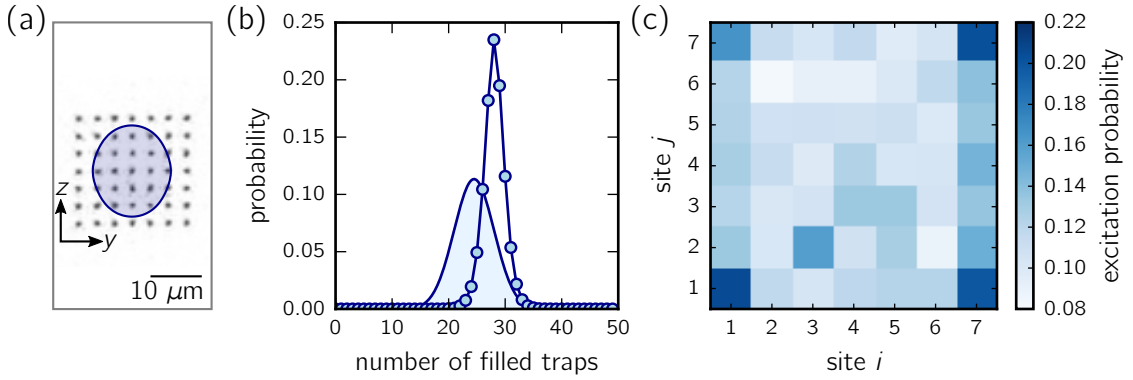

Figure 6.9: Parameters of the partially loaded 7x7 square trap array. (a) CCD image of the trap intensities, with a lattice spacing $a = 3.5\,\mu$m. The blue shaded area shows the blockade radius of $R_b \simeq 9.1\,\mu$m for the $|61D_{3/2}\rangle$ state, with $\alpha = 2.6$. (b) The experiment is triggered on the presence of $N \geq 30$ atoms in the 49 traps. The points show the relative occurrences of obtained numbers of ground state atoms in the initial atom configurations. The shaded area shows the expected distribution for random triggering. (c) Single-site resolved Rydberg excitation probability of a ground state atom at position $(i, j) = (\frac{y}{a}, \frac{z}{a})$ in the array, for an excitation time $\Omega_1\tau = 0.90\pi$. Due to finite size effects the excitation probability is slightly higher at the edges and corners of the array.

In order to further probe the influence of the angular dependence on the dynamics of the Rydberg fraction and the Rydberg-Rydberg pair correlations, we now prepare a two-dimensional 7×7 square trap array, with a lattice spacing $a = 3.5\,\mu$m. We use the Rydberg state $|61D_{3/2}\rangle$ with a calculated $C_6/h = 7.6 \times 10^5\,\text{MHz}\,\mu\text{m}^6$. With a single atom Rabi frequency $\Omega_1 \simeq 2\pi \times 1.4\,\text{MHz}$ we expect a blockade radius $R_b = 9.1\,\mu$m, giving a ratio $\alpha = 2.6$.

We trigger the experiment on the presence of $N \geq 30$ atoms present in the 49 traps, narrowing and shifting the atom number distribution to higher atom numbers compared to random triggering (see Figure 6.9(b)). Again we do not post-select the experiments on the initial atom number. In Figure 6.9(c) we show the Rydberg excitation probability for each site in the array, for an excitation time $\Omega_1\tau = 0.90\pi$. We see the effect of the finite size of the system, leading to a higher excitation probability along the edges and in the corners of the array, as those sites have fewer neighbours than the sites in the bulk, and thus are less often blockaded. Even though the false positive detection probability ε varies between 2 % and 4 % among the trap sites, those variations do not contain any pattern, and would be to small to explain the variation in excitation probability.

The measured dynamics of the Rydberg fraction f_r for the square array, shown in

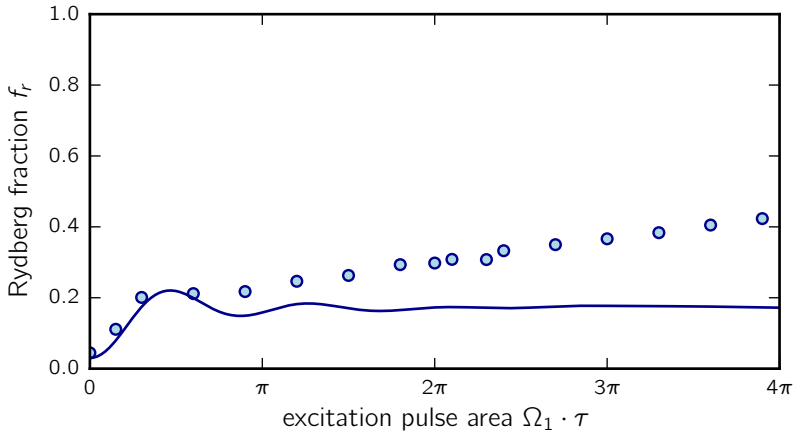

Figure 6.10: Time evolution of the Rydberg fraction in the 7x7 square trap array. Measured Rydberg fraction f_r (points) and solution of the Schrödinger equation with the spin-1/2 Hamiltonian of Equation 6.3 (solid line), taking into account a false detection probability of $\varepsilon = 3\,\%$.

Figure 6.10, agrees with the spin-1/2 model only for short excitation times below $\Omega_1\tau = 1\pi$, then monotonously increases with the excitation time without showing any further oscillations. This suggests that already with $N_{\mathrm{at}} \sim 30$ atoms, the observed excitation dynamics resembles that of a many-body system observed in large ensembles (see e.g. [Löw *et al.*, 2009]), with an initial fast rise followed by a saturation of the Rydberg fraction. However, if the magnitude of the van der Waals interaction would just be smaller than expected, the saturation of the Rydberg fraction would occur at a slightly higher value, but we would not see a slow continuous increase as observed in the experiment. We thus again attribute the seemingly linear increase of f_r for $\Omega_1\tau > \pi$ to multilevel effects, which are indeed expected to be strong in this array where the internuclear axis of many pairs lies at a large angle θ to the quantisation axis.

In order to study the effect of the finite size of the system and the angular dependence of the interaction on the Rydberg-Rydberg correlations, we now compute the two-dimensional pair correlation function

$$g^{(2)}(\Delta k, \Delta l) = \frac{1}{N_{\mathrm{traps}}} \sum_{i,j} \frac{\langle n_{i,j} n_{i+\Delta k, j+\Delta l}\rangle}{\langle n_{i,j}\rangle \langle n_{i+\Delta k, j+\Delta l}\rangle}, \tag{6.7}$$

where $n_{i,j}$ refers to the excitation probability at position $(i, j) = (y/a, z/a)$ of the array, and the site distances $\Delta k, \Delta l$ each ranging from -6 to 6. Both $n_{i,j}$ and $n_{i+\Delta k, j+\Delta l}$ are computed from only those experiments where a ground state atom is present in the

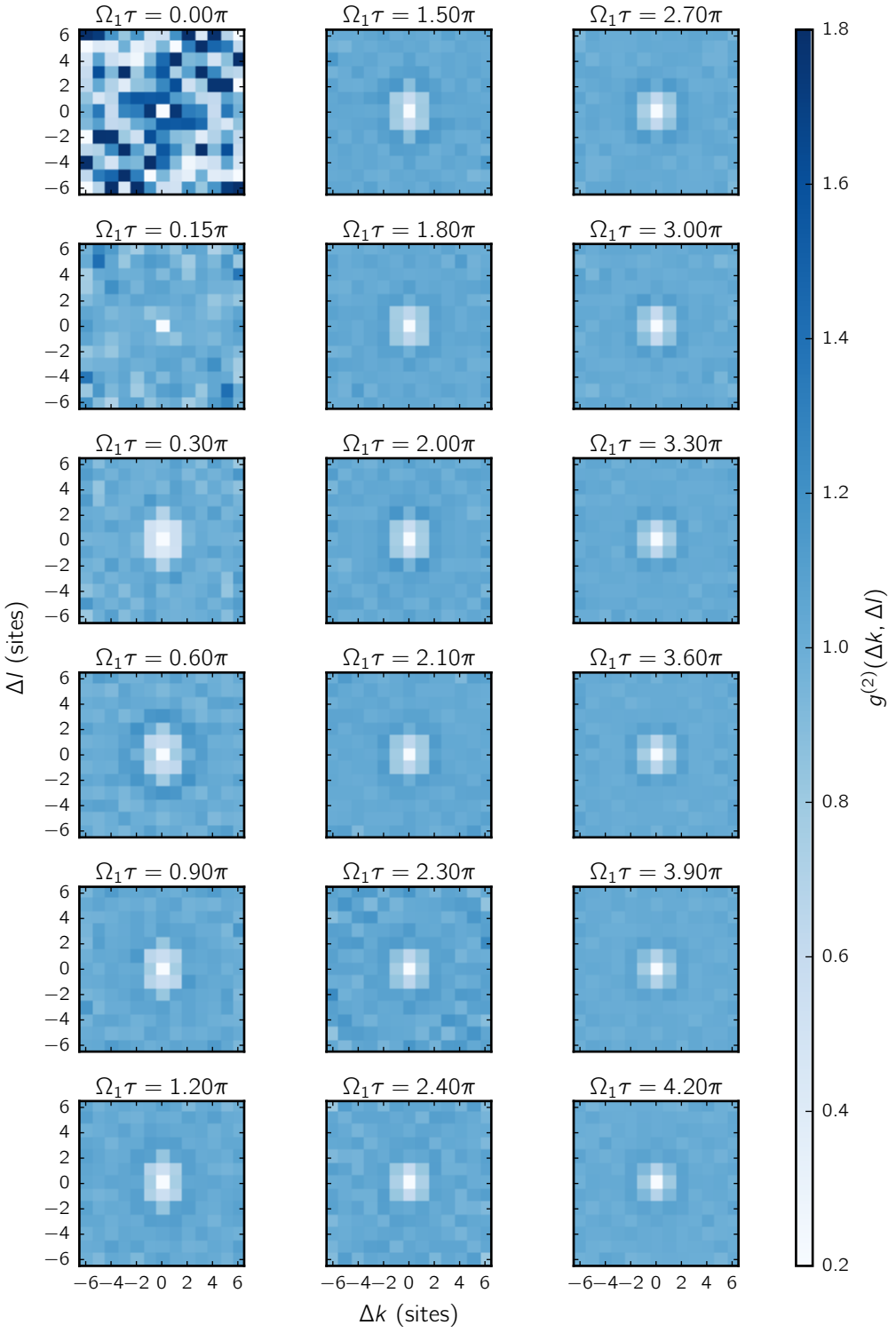

Figure 6.11: Time evolution of the pair correlation function in the 7x7 array. Already after very short excitation times a strong suppression of neighbouring Rydberg pairs emerges in the correlation function, becoming slightly weaker for long excitation times. Note the unevenly spaced excitation times of the experiment.

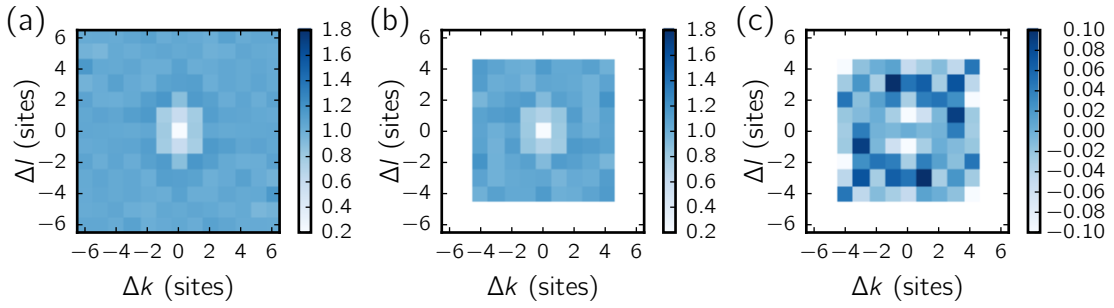

Figure 6.12: Influence of the edge atoms on the pair correlations. Pair correlation function $g^{(2)}(\Delta k, \Delta l)$ of the 7x7 array, for a excitation time of $\Omega_1\tau = 1.5\pi$, (a) taking into account all sites on the array, as shown in Figure 6.11, (b) ignoring correlations where one atom sits on the edge of the array, and (c) the difference for the two. The same behaviour is observed for other excitation times.

initial atom configuration both at site (i, j) and at site $(i + \Delta k, j + \Delta l)$ at the same time. Here we omit the explicit time dependence of $g^{(2)}$ for better readability.

The measured Rydberg-Rydberg pair correlations are shown in Figure 6.11. Despite the finite size of the array, we clearly see the fast emergence of a strong depletion around each excitation. We already see strong correlations after an excitation pulse area of only $\Omega_1\tau = 0.3\pi$. For excitation times up to $\Omega_1\tau \approx 2\pi$ we see an isotropy in the pair correlations which resembles that of the effective van der Waals potential of Equation 5.7, which then seems to disappear at later times. This is not yet understood.

Lastly, in order to probe the effect of the finite size of the system, we again compute the pair correlation function according to Equation 6.7, this time neglecting the sites which are on the edge of the 7×7 array, i.e letting i and j only run from 2 to 6 thus and Δk and Δl from -4 to 4. The obtained $g^{(2)}$, together with that of Figure 6.11 using the full array, are shown in Figure 6.12 for an excitation time $\Omega_1\tau = 1.5\pi$. Except for a slightly increased noise, the results are qualitatively equivalent. The same holds true for all other measured excitation times. The finite size of the arrays therefore does not seem to have a large impact on the pair correlations, which is not surprising as the blockade radius is small compared to the size of the array.

6.4 Conclusion

We have realised the quantum Ising model of a spin-1/2 system both in effective one-dimensional atom arrays with periodic boundary conditions and in a two-dimensional atom array. We have benchmarked our implementation of a spin system by comparing

both the Rydberg fraction f_r and the Rydberg-Rydberg pair correlation function $g^{(2)}$ against a numerical simulation of the quantum Ising model for the experiments where a numerical treatment was still practical.

We observed an overall good agreement for short excitation times. For long excitation times, we notice an increase of nearby Rydberg pair-excitations for most cases, which is not reproduced by the spin-1/2 model. For the racetrack-shaped trap array with a large blockade radius, where most of the interacting atom pairs are aligned along the quantisation axis, we observe an exceptional agreement between our experiment and the spin-1/2 model.

The obtained results are promising in view of the quantum simulation of spin systems with single Rydberg atoms. Additional work is necessary to e.g. clarify the role of the Zeeman level-structure of Rydberg D-states as pointed out in Chapter 5, in order to better understand the cause of the discrepancy between the experiment and the spin-1/2 model.

Chapter 7

The Rydberg blockade in the resonant dipole-dipole regime

The Rydberg blockade is predominantly studied in the van der Waals regime [Comparat and Pillet, 2010]. However, a similar type of blockade can be observed for resonant dipole-dipole interactions [Vogt *et al.*, 2007; van Ditzhuijzen *et al.*, 2008; Reinhard, Younge, and Raithel, 2008; Maxwell *et al.*, 2013; Gunter *et al.*, 2013; Ravets *et al.*, 2014].

Although the van der Waals and the resonant dipole-dipole interaction are two regimes of the same atomic interaction, the characteristics of the blockade can be somewhat different. In the van der Waals regime, the strong interaction shifts all states with more than a single excitation out of resonance within a certain blockade volume, as we have seen in Chapter 5. In the resonant dipole-dipole regime, the blockade mechanism is a bit more involved, due to the off-diagonal nature of the interaction.

We have previously studied the resonant dipole-dipole blockade by tuning two different atomic pair states into resonance by applying a specific electric field [Ravets *et al.*, 2014, 2015], a so-called Förster resonance [Walker and Saffman, 2005].

Here, we present a slightly different approach to observe the Rydberg blockade between two single atoms in the resonant-dipole regime, by driving coherent Rydberg-Rydberg transitions using microwaves. By scanning the frequency of the microwave field, we can excite a symmetric 'superradiant' state with a coupling strength enhanced by the expected factor $\sqrt{2}$, while seeing no coupling to the antisymmetric 'dark' state.

7.1 Theoretical description

The principle of the experiment is depicted in Figure 7.1. Two atoms in the $|d\rangle = \left|nD_{3/2}\right\rangle$ Rydberg state are placed along the quantisation axis, with an interatomic distance R. We then shine in a microwave field resonant to the single atom $|d\rangle \leftrightarrow |p\rangle = \left|(n+1)P_{1/2}\right\rangle$ transition with a coupling strength given by the single atom microwave

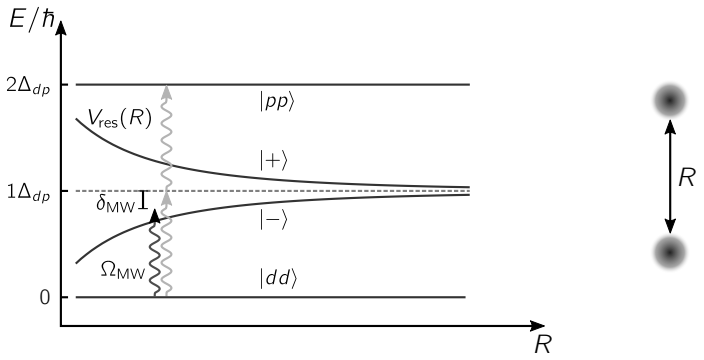

Figure 7.1: Illustration of the Rydberg blockade in the resonant dipole-dipole regime. Due to the resonant dipole-dipole interaction, the two-atom state $|dp\rangle$ is split into the bright state $|+\rangle = (|dp\rangle + |pd\rangle)/\sqrt{2}$ and the dark state $|-\rangle = (|dp\rangle - |pd\rangle)/\sqrt{2}$. For small distances, the microwave transfer is thus blockaded at the single atom resonance $\delta_{\mathrm{MW}} = 0$ (dark grey wiggly line). The state $|pp\rangle$ may still be excited via a two-photon excitation (light grey wiggly line), albeit with a reduced coupling strength. (The van der Waals interaction is neglected here.)

Rabi frequency Ω_{MW}. With the resonant dipole-dipole interaction, the new eigenstates of the system are now

$$\begin{aligned} &|dd\rangle \\ &|+\rangle = \frac{|dp\rangle + |pd\rangle}{\sqrt{2}} \\ &|-\rangle = \frac{|dp\rangle - |pd\rangle}{\sqrt{2}} \\ &|pp\rangle\,, \end{aligned} \tag{7.1}$$

where the superposition states $|\pm\rangle$ are shifted by an amount $\pm V_{\mathrm{res}} = \pm \langle dp| \hat{V}_{\mathrm{dd}} |pd\rangle = \pm C_3/R^3$. With the microwave field tuned to the single atom resonance, i.e. $\delta_{\mathrm{MW}} = 0$, the states $|\pm\rangle$ are thus shifted out of resonance if $C_3/R^3 \gg \Omega_{\mathrm{MW}}$, and the microwave transfer of one of the two atoms to the $|p\rangle$ state is thus blockaded. On the other hand, the microwave field can still transfer both atoms at the same time, to the doubly excited state $|pp\rangle$, without populating the states $|dp\rangle$ or $|pd\rangle$. However, since this is an off-resonant two photon transition, it has a reduced coupling strength $\Omega_{\mathrm{2ph}} \approx \hbar\Omega_{\mathrm{MW}}^2/V_{\mathrm{res}}$ when $\Omega_{\mathrm{MW}} \ll V_{\mathrm{res}}$.

7.2 Microwave spectroscopy of a resonantly interacting two-atom system

In order to perform this experiment, we need to be able to efficiently excite the atoms to the initial $|dd\rangle$ state, meaning that the van der Waals interaction of this state should be small compared to the optical Rabi frequency. At the same time, we want the resonant dipole-dipole interaction of the $|pd\rangle$ state to be large, in order to shift the $|\pm\rangle$ states off-resonant to the microwave field.

We therefore choose an interatomic distance of $R \simeq 10.3\,\mu$m, and the Rydberg states $|d\rangle = \left|62D_{3/2}\right\rangle$ and $|p\rangle = \left|63P_{1/2}\right\rangle$. In this case, the van der Waals interaction of the $|dd\rangle$ state $V_{\mathrm{vdW}}(10.3\,\mu\mathrm{m}) \simeq h \times 0.7\,\mathrm{MHz}$ can be neglected compared to the optical Rabi frequency $\Omega_1 \simeq 2\pi \times 7.8\,\mathrm{MHz}$ used to prepare the initial $|dd\rangle$ state. We have previously measured a $C_3 = 7950 \pm 130\,\mathrm{MHz}\,\mu\mathrm{m}^3$ for the resonant dipole-dipole interaction of the $|pd\rangle$ state [Barredo *et al.*, 2015]. The expected interaction strength at the chosen distance $V_{\mathrm{res}}^{(\mathrm{theo})}(10.3\,\mu\mathrm{m}) = h \times 7.3 \pm 0.1\,\mathrm{MHz}$ is large compared to the chosen microwave Rabi frequency $\Omega_{\mathrm{MW}} \simeq 2\pi \times 0.87\,\mathrm{MHz}$. The van der Waals interaction of the $|pp\rangle$ state is $V_{\mathrm{vdW}}(10.3\,\mu\mathrm{m}) < h \times 0.1\,\mathrm{MHz}$ and is negligible compared to all other relevant frequencies. As explained in Section 2.5, we measure the final population in $|d\rangle$ at the end of an experiment by coherently coupling it back to the ground state $|g\rangle$.

We first use one single atom to calibrate the transition frequency between the $|d\rangle$ and $|p\rangle$ state, and find[1] $\Delta_{dp}/2\pi \simeq 9132.50\,\mathrm{MHz}$, shown in Figure 7.2(a). We then use two atoms as mentioned above. Figure 7.2(b) shows the probability to find the atoms in $|dd\rangle$ after sending a microwave pulse with a $\tau_{\mathrm{MW}} = 0.4\,\mu$s duration, when scanning the microwave detuning δ_{MW}. We see a depletion of the population in the $|dd\rangle$ state for $\delta_{\mathrm{MW}}/2\pi = V_{\mathrm{res}}^{(\mathrm{exp})}/h = -7.45\,\mathrm{MHz}$, corresponding to the excitation of the $|+\rangle$ state, close to the expected value of $V_{\mathrm{res}}^{(\mathrm{theo})}/h = 7.3 \pm 0.1\,\mathrm{MHz}$. The width of the resonance is about 1.8 times the width of the single atom resonance, larger than the expected factor $\sqrt{2} \simeq 1.414$. This broadening is explained by the shot-to-shot fluctuations of the interatomic distance of $\approx 100\,\mathrm{nm}$ due to the finite temperature of the atoms, which in turn can lead to variations in interaction strength of up to 0.5 MHz.

Changing the microwave frequency by the same absolute value but with a positive detuning should tune the field resonant to the $|-\rangle$ state. However, we do not observe any transfer away from the $|dd\rangle$ state, since the microwave coupling to this 'dark' state

[1] We still apply a $+6\,\mathrm{G}$ magnetic field along the z axis to define a quantisation axis.

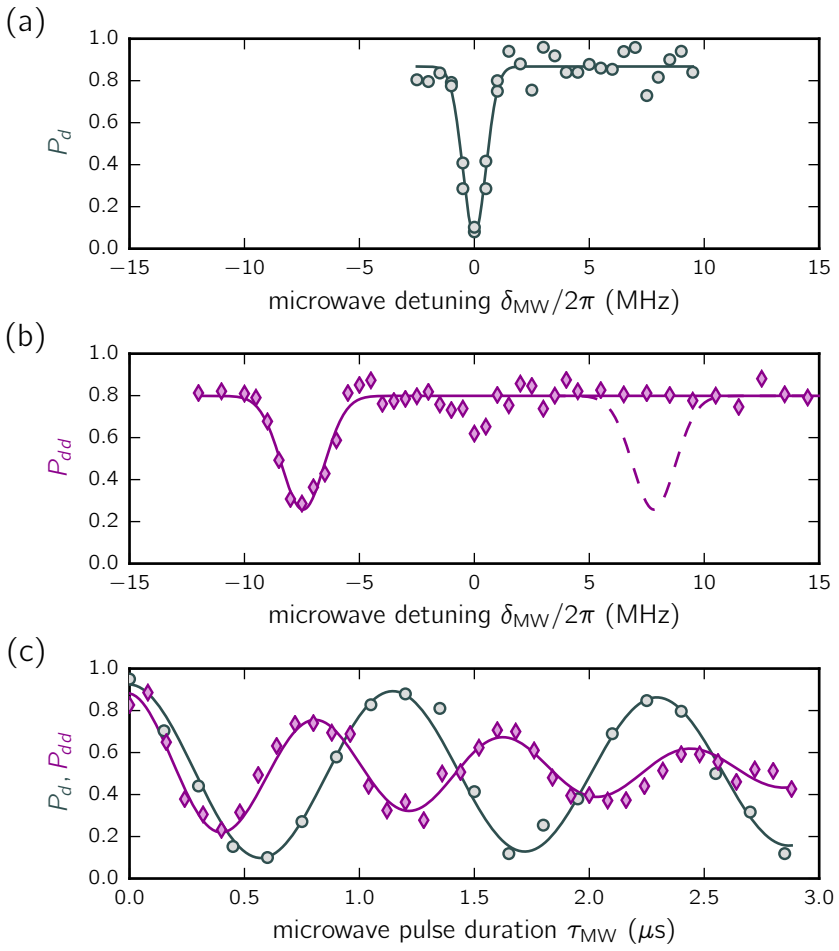

Figure 7.2: Spectroscopy and Rabi oscillation of the p-d microwave transition for one and two atoms. (a) Spectroscopy of a single atom. We show the probability P_d to find the atom in the $|d\rangle$ state after sending a 400 ns microwave pulse of frequency $(\Delta_{dp}+\delta_{MW})$, with $\Delta_{dp}/2\pi = 9\,132.50$ MHz. (b) Spectroscopy of two atoms with an interatomic distance of $R = 10.3\,\mu$m. We measure the probability P_{dd} to find the atoms in the $|dd\rangle$ state after sending the 400 ns microwave pulse. We find a shift of the superradiant $|+\rangle$ state of $\delta_+/2\pi \simeq -7.45$ MHz, whereas we find no population transfer at the expected position of the subradiant $|-\rangle$ state (dashed purple line). The small dip pf P_{dd} at $\delta_{MW} = 0$ is caused by the imperfect state preparation (see text). (c) Microwave driven Rabi oscillations. We measure a single atom Rabi oscillation (grey circles) of $\Omega_{MW} = 2\pi \times 0.87$ MHz for a detuning $\delta_{MW} = 0$. For two atoms and the microwave field tuned resonant to the $|dd\rangle \leftrightarrow |+\rangle$ transition, i.e. $\delta_{MW} = \delta_+$ (purple diamonds), we measure an enhanced Rabi frequency $\Omega_+ \simeq 1.41\Omega_{MW}$.

is zero. With the microwave field tuned to the single atom resonance, i.e. $\delta_{\mathrm{MW}} = 0$, we observe a small dip in the $|dd\rangle$ population. One might think that this is caused by a two-photon transition to the $|pp\rangle$ state. This not the case however, as the two-photon Rabi frequency $\Omega_{2\mathrm{ph}} \approx \hbar\Omega_{\mathrm{MW}}^2/V_{\mathrm{res}} \simeq 0.1\,\mathrm{MHz}$ is very weak, and with the $\tau_{\mathrm{MW}} = 0.4\,\mu\mathrm{s}$ microwave pulse we only expect a population in $|pp\rangle$ of $P_{pp} < 0.02$ according to Equation 2.10[2]. The dip is actually caused by an imperfect initial Rydberg state preparation. As in some cases only one of the two ground state atoms is excited, thus preparing the state $|gd\rangle$, the microwave pulse is now resonant again for the single Rydberg atom, resulting in the final state $|gp\rangle$ and thus a reduced observed population in $|dd\rangle$.

We now tune the microwave field resonant to the $|dd\rangle \leftrightarrow |+\rangle$ transition, i.e. $\delta_{\mathrm{MW}}/2\pi = -7.45\,\mathrm{MHz}$, to drive a coherent Rabi oscillation between the two states. We measure a collective Rabi frequency of $\Omega_{\mathrm{MW}}^{(2)} = 2\pi \times 1.2\,\mathrm{MHz} = 1.4\Omega_{\mathrm{MW}}$, perfectly matching the expected $\sqrt{2}$ enhancement. We notice a significant increase of damping for the two-atom oscillation compared to the single-atom oscillation. Again, this is due to the shot-to-shot fluctuations of the interatomic separation, which can lead to a slightly off-resonant excitation of the $|+\rangle$ state. Note that for the collective Rabi oscillation in the van der Waals regime these fluctuations do not play a role. They do change the exact interaction strength between the atoms from shot to shot, they do not play any role however, since the exact magnitude of the interaction is not important here, as long as it is larger than optical Rabi frequency.

7.3 A possible extension to many atoms

We have seen that here, different to the van der Waals Rydberg blockade, there is interaction between the atoms even if there is only one 'excitation' present in the system. In view of extending the above experiment from two to many atoms, analogous to the van der Waals regime in Chapter 5, and to further illustrate the difference of the two regimes, we consider the following 'gedankenexperiment'. We take a system of 9 atoms all in the $|d\rangle$ state, arranged in a 3×3 array, with the quantisation axis parallel to the plane of the atoms, such that the resonant dipole-dipole interaction is isotropic in the plane of the atoms. We want to see what to expect when we couple this state $\left|d^{(9)}\right\rangle = |d_1 d_2 ... d_N\rangle$ to a state with a single $|p\rangle$ excitation.

The eigenenergies of a system whose basis consists of the nine states containing one

[2] This is confirmed by a numerically solving the Schrödinger equation of the 4-level system, showing a negligible population of the $|pp\rangle$ state for experimental parameters used here.

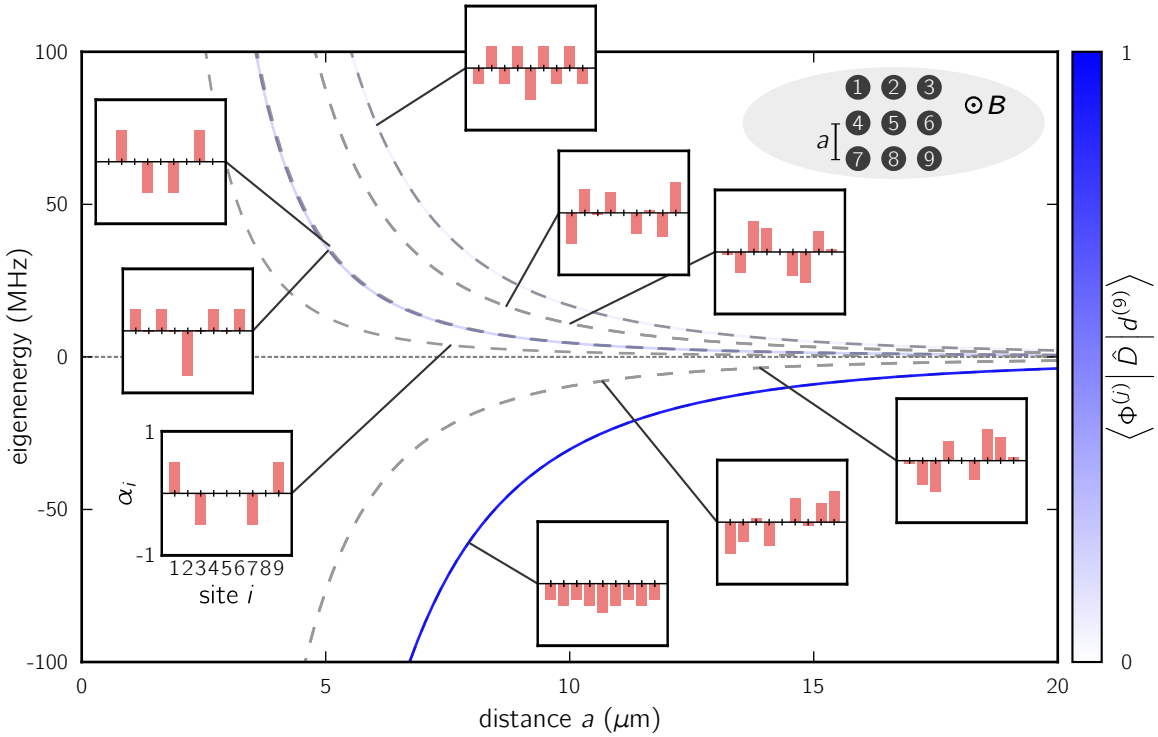

Figure 7.3: Calculated energy spectrum of a 3x3 atom array with a single P excitation in the resonant dipole-dipole regime. We calculate the eigenenergies of a 3×3 array of Rydberg atoms, with 8 atoms in the $|d\rangle = |62D_{3/2}\rangle$ state, and a single $|p\rangle = |63P_{1/2}\rangle$ excitation, with a $C_3 = 7\,965\,\text{MHz}\,\mu\text{m}^3$, and isotropic in-plane interactions. The grey dashed lines indicate the eigenenergies of the nine eigenstates $|\Phi^{(j)}\rangle$, $j \in [1, 9]$, as the function of the lattice spacing. The strength of the blue shading indicates the relative microwave coupling strength to the state $|d^{(9)}\rangle = |d_1 d_2 ... d_9\rangle$. The insets show for each eigenstate the probability amplitudes $\alpha_i^{(j)} = \langle \phi_i | \Phi^{(j)} \rangle$ to find the $|p\rangle$ excitation at atom i for each eigenstate , with $|\phi_i\rangle = |d_1 d_2 ... p_i ... d_N\rangle$ (atom labelling indicated in the top right).

single excitation $|\phi_i\rangle = |d_1 d_2 ... p_i ... d_N\rangle$, with $i \in [1, 9]$, are shown in Figure 7.3. Due to the resonant dipole-dipole interaction between the single $|p\rangle$ excitation and the remaining $|d\rangle$ state atoms, the absolute values of the eigenenergies become large for small lattice spacings.

We now compute the microwave coupling strength to the various singly excited eigenstates $|\Phi^{(j)}\rangle = \frac{1}{\sqrt{N}} \sum_{i=1}^{N} \alpha_i^{(j)} |\phi_i\rangle$. The coefficients α_i are shown in the insets in Figure 7.3 for all eigenstates j. We assume that the microwave coupling is equal for all atoms, i.e. $\langle d_i | \hat{d} | p_i \rangle = c$ for all i, with $\hat{d}$ being the transition dipole operator, and c a constant. The coupling strength $\langle \Phi^{(j)} | \hat{D} | d^{(9)} \rangle$ is shown as the strength of the blue shading on the eigenenergies in Figure 7.3, with $\hat{D} = \sum_i \hat{d}_i$. We see one

strongly superradiant state with an enhanced coupling, although showing a smaller enhancement than the $\sqrt{9}$ in the van der Waals regime. A second eigenstate is still weakly coupled, whereas the coupling to all other states is zero. It should therefore be possible, if one where to spectroscopically probe such a 3×3 atom array, to find 2 resonances for the microwave transition.

For a fully symmetric system, e.g. all atoms arranged on a ring, all states $|\phi_i\rangle = |d_1 d_2 ... p_i ... d_N\rangle$ would have the same energy, since it makes no difference at which site the $|p\rangle$ excitation is. One finds that in this case, there is only one superradiant state with a $\sqrt{N}$ enhanced coupling (N being the number of atoms), the remaining eigenstates all being dark states. The difficulty in this type of microwave experiment remains the reliable excitation of the array of ground state atoms to the Rydberg $|d\rangle$ states, i.e. overcoming the van der Waals interaction, while at the same time being fully blockaded in the resonant dipole-dipole regime.

7.4 Conclusion

We observed the Rydberg blockade in the resonant dipole-dipole regime by shining a microwave pulse on two single Rydberg atoms. Unlike the van der der Waals interaction, which only acts perturbatively on interacting pair states, the resonant dipole-dipole interaction changes the eigenstates of the interacting system, due to its off-diagonal nature.

By tuning the microwave field resonant to the symmetric 'bright' superposition state we could observe its $\sqrt{2}$-enhanced coupling to the initially prepared Rydberg pair-state.

Using the resonant dipole-dipole interaction between Rydberg atoms we can implement an XY spin-Hamiltonian of the form [Barredo *et al.*, 2015]

$$H = \frac{1}{2} \sum_{i \neq j} V_{ij} (\sigma_i^+ \sigma_j^- + \sigma_i^- \sigma_j^+), \tag{7.2}$$

allowing the study of dipolar energy transport, which plays for example an important role in photosynthesis [Collini *et al.*, 2010] and organic semiconductors [Najafov *et al.*, 2010].

Chapter 8

Conclusion and outlook

In this thesis I presented my work on probing the dynamics and pair correlations of Rydberg excitations in 2D arrays of single neutral atoms. Two main technical advancements of the existing experimental setup [Béguin, 2013; Ravets, 2014] were necessary to realise such kind of experiments. First, the implementation of a spatial light modulator to shape the spatial phase of our optical dipole trap beam now allows us to arrange as many as ~ 100 single atom traps in any desired 2D pattern, with trap separations as low as $\sim 3\,\mu$m, and array sizes as large as $\sim 50 \times 50\,\mu\text{m}^2$. Second, using a sensitive CCD camera to detect the atomic fluorescence provides the real-time, single-site resolved monitoring of the filling of the traps.

The combination of these two techniques lets us to perform Rydberg experiments with any chosen two-dimensional arrangement of ground state atoms, measuring the site-resolved Rydberg excitation efficiency with an unprecedented $\gtrsim 95\,\%$ efficiency. The real-time monitoring of the fluorescence from the traps allows us to trigger and / or post-sort experiments on any atom configuration, e.g. a given number of present atoms. We can perform experiments with fully loaded trap arrays with up to nine traps. For larger trap numbers, we are as of now constrained to partially loaded arrays, due to the randomness of loading single atoms in the microtraps, which results in a probability of about 0.5^{N_t} to have a fully loaded N_t-trap array.

Techniques leading to single-trap occupation probabilities up to $90\,\%$ have been successfully demonstrated recently by optimising the light-assisted collision process [Fung and Andersen, 2015; Lester *et al.*, 2015]. This is comparable to the filling fraction of single atoms in an optical lattice in the Mott-insulator regime for a defined pattern [Weitenberg *et al.*, 2011]. A preliminary implementation of this technique in our experiment gave trap loading probabilities of about $80\,\%$ (see Figure 8.1).

We measured the collective enhancement of a single Rydberg excitation for up to $N = 15$ atoms, in the full blockade regime of the van der Waals interaction, observing the expected $\sqrt{N}$-scaling. Our single-site resolved atom detection lets us determine the initially prepared number states with a fidelity close to unity. We measure a double excitation probability higher than expected from both the simple blockade picture and

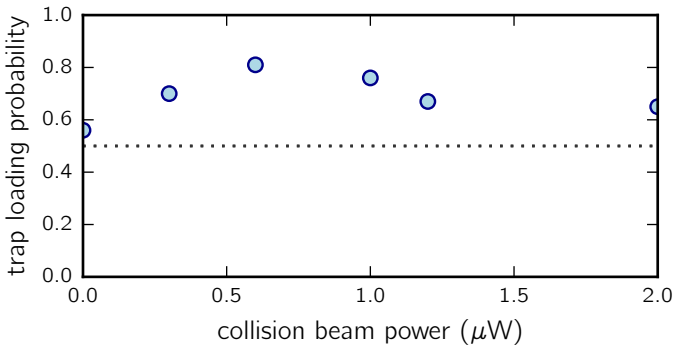

Figure 8.1: Enhanced single atom loading. By adjusting the parameters of the collision beam, the laser beam photo-associating the atom pair in the inelastic collision, collisions where only one atom leaves the trap become more probable. In a preliminary test, we achieve trap loading probabilities up to 80 %.

the numerical simulation of the Schrödinger equation. We suggest that this is caused by the Zeeman-substructure of the used Rydberg D-states, which are coupled by the van der Waals interaction for atom pairs not aligned with the quantisation axis.

We have measured a similar Rydberg blockade in the regime of resonant dipole-dipole interactions for two single atoms, using microwave transitions in the Rydberg manifold. When tuning the microwave field resonant to the superradiant symmetric superposition state, we again measure the expected $\sqrt{2}$-enhancement of the microwave coupling.

Finally, demonstrating the versatility of the presented setup, we have implemented the quantum Ising model of a spin-1/2 system, in various one- and two-dimensional geometries, for up to 30 atoms. We probed the excitation dynamics and Rydberg-Rydberg pair correlations in the partial blockade regime of the van der Waals interaction, and compared the results to numerical simulations of the quantum Ising model wherever possible. We observe a good agreement to the model especially for short excitation times. If the effect of the anisotropy of the van der Waals interaction is small, the agreement to the spin-1/2 model is exceptional.

Apart from achieving a higher filling fraction of the traps by optimising the light-assisted collisions, reducing the temperature of the single atom, e.g. by Raman sideband cooling [Kaufman, Lester, and Regal, 2012], will be an important task in view of future experiments. Lower atom temperatures will improve the false Rydberg detection probability, which will be important when working with even larger atom numbers, and reduce the Doppler effect during the Rydberg excitation.

The results presented in this thesis are an important step towards the realisation of Rydberg quantum simulator for spin-1/2 system, of both the quantum Ising model

presented in this thesis, and the XY-model, which we have already realised in a chain of three atoms [Barredo *et al.*, 2015].

This experiment will allow to probe strongly correlated mesoscopic quantum systems with single particle resolution, ranging from the study of topological insulators by effective spin-orbit coupling [Peter *et al.*, 2015], exotic states of matter [Glaetzle *et al.*, 2014], thermalisation in closed quantum systems [Ates, Garrahan, and Lesanovsky, 2012], to the dynamical emergence of entanglement following a quantum quench [Hazzard *et al.*, 2014].

Following the path of quantum information with Rydberg atoms [Saffman, Walker, and Mølmer, 2010; Wilk *et al.*, 2010; Isenhower *et al.*, 2010], we can put to test protocols such as the CNOT-gate [Maller *et al.*, 2015], or creating strongly entangled GHZ states [Greenberger, Horne, and Zeilinger, 1989; Müller *et al.*, 2009].

Bibliography

Anderson, P. W., *"Absence of Diffusion in Certain Random Lattices,"* Physical Review **109**, 1492–1505 (1958).

Anderson, W. R., Veale, J. R., and Gallagher, T. F., *"Resonant Dipole-Dipole Energy Transfer in a Nearly Frozen Rydberg Gas,"* Physical Review Letters **80**, 249–252 (1998).

Ates, C., Garrahan, J. P., and Lesanovsky, I., *"Thermalization of a Strongly Interacting Closed Spin System: From Coherent Many-Body Dynamics to a Fokker-Planck Equation,"* Physical Review Letters **108**, 110603 (2012).

Auerbach, A., Interacting electrons and quantum magnetism (Springer Science & Business Media, 2012).

Balewski, J. B., Krupp, A. T., Gaj, A., Peter, D., Büchler, H. P., Löw, R., Hofferberth, S., and Pfau, T., *"Coupling a single electron to a BoseEinstein condensate,"* Nature **502**, 664–667 (2013).

Balmer, J. J., *"Notiz über die Spectrallinien des Wasserstoffs,"* Annalen der Physik **261**, 80–87 (1885).

Barredo, D., Labuhn, H., Ravets, S., Lahaye, T., Browaeys, A., and Adams, C. S., *"Coherent Excitation Transfer in a Spin Chain of Three Rydberg Atoms,"* Physical Review Letters **114**, 113002 (2015).

Barredo, D., Ravets, S., Labuhn, H., Béguin, L., Vernier, A., Nogrette, F., Lahaye, T., and Browaeys, A., *"Demonstration of a Strong Rydberg Blockade in Three-Atom Systems with Anisotropic Interactions,"* Physical Review Letters **112**, 183002 (2014).

Bässler, H., *"Charge Transport in Disordered Organic Photoconductors a Monte Carlo Simulation Study,"* physica status solidi (b) **175**, 15–56 (1993).

Baur, S., Tiarks, D., Rempe, G., and Dürr, S., *"Single-Photon Switch Based on Rydberg Blockade,"* Physical Review Letters **112**, 073901 (2014).

Becker, C., Stellmer, S., Soltan-Panahi, P., Dörscher, S., Baumert, M., Richter, E.-M., Kronjäger, J., Bongs, K., and Sengstock, K., *"Oscillations and interactions of dark and darkbright solitons in BoseEinstein condensates,"* Nature Physics **4**, 496–501 (2008).

Béguin, L., Measurement of the van der Waals interaction between two Rydberg atoms, Ph.D. thesis, Université Paris IX (2013).

Béguin, L., Vernier, A., Chicireanu, R., Lahaye, T., and Browaeys, A., *"Direct Measurement of the van der Waals Interaction between Two Rydberg Atoms,"* Physical Review Letters **110**, 263201 (2013).

Bergamini, S., Darquié, B., Jones, M., Jacubowiez, L., Browaeys, A., and Grangier, P., *"Holographic generation of microtrap arrays for single atoms by use of a programmable phase modulator,"* Journal of the Optical Society of America B **21**, 1889 (2004).

Beugnon, J., Tuchendler, C., Marion, H., Gaëtan, A., Miroshnychenko, Y., Sortais, Y. R. P., Lance, A. M., Jones, M. P. A., Messin, G., Browaeys, A., and Grangier, P., *"Two-dimensional transport and transfer of a single atomic qubit in optical tweezers,"* Nature Physics **3**, 696–699 (2007).

van Bijnen, R. M. W., Quantum Engineering with Ultracold Atoms, Ph.D. thesis, Technische Universiteit Eindhoven (2013).

van Bijnen, R. M. W., Ravensbergen, C., Bakker, D. J., Dijk, G. J., Kokkelmans, S. J. J. M. F., and Vredenbregt, E. J. D., *"Patterned Rydberg excitation and ionization with a spatial light modulator,"* New Journal of Physics **17**, 023045 (2015).

Blatt, R. and Roos, C. F., *"Quantum simulations with trapped ions,"* Nature Physics **8**, 277–284 (2012).

Bohnet, J. G., Sawyer, B. C., Britton, J. W., Wall, M. L., Rey, A. M., Foss-feig, M., and Bollinger, J. J., *"Quantum spin dynamics and entanglement generation with hundreds of trapped ions,"* (2015), arXiv:1512.03756 .

Bohr, N., *"I. On the constitution of atoms and molecules,"* Philosophical Magazine Series 6 **26**, 1–25 (1913).

Born, M., Wolf, E., Bhatia, A. B., Clemmow, P. C., Gabor, D., Stokes, A. R., Taylor, A. M., Wayman, P. A., and Wilcock, W. L., Principles of Optics (Cambridge University Press, Cambridge, 1999).

Boyer, V., Godun, R. M., Smirne, G., Cassettari, D., Chandrashekar, C. M., Deb, A. B., Laczik, Z. J., and Foot, C. J., *"Dynamic manipulation of Bose-Einstein condensates with a spatial light modulator,"* Physical Review A **73**, 031402 (2006).

Bozinovic, N., Yue, Y., Ren, Y., Tur, M., Kristensen, P., Huang, H., Willner, A. E., and Ramachandran, S., *"Terabit-Scale Orbital Angular Momentum Mode Division Multiplexing in Fibers,"* Science **340**, 1545–1548 (2013).

Branden, D. B., Juhasz, T., Mahlokozera, T., Vesa, C., Wilson, R. O., Zheng, M., Kortyna, A., and Tate, D. A., *"Radiative lifetime measurements of rubidium Rydberg states,"* Journal of Physics B: Atomic, Molecular and Optical Physics **43**, 015002 (2010).

Britton, J. W., Sawyer, B. C., Keith, A. C., Wang, C.-C. J., Freericks, J. K., Uys, H., Biercuk, M. J., and Bollinger, J. J., *"Engineered two-dimensional Ising interactions in a trapped-ion quantum simulator with hundreds of spins."* Nature **484**, 489–92 (2012).

Brunner, N., Cavalcanti, D., Pironio, S., Scarani, V., and Wehner, S., *"Bell nonlocality,"* Reviews of Modern Physics **86**, 419–478 (2014).

Carroll, T. J., Claringbould, K., Goodsell, A., Lim, M. J., and Noel, M. W., *"Angular Dependence of the Dipole-Dipole Interaction in a Nearly One-Dimensional Sample of Rydberg Atoms,"* Physical Review Letters **93**, 153001 (2004).

Castro Neto, A. H., Guinea, F., Peres, N. M. R., Novoselov, K. S., and Geim, A. K., *"The electronic properties of graphene,"* Reviews of Modern Physics **81**, 109–162 (2009).

Cheneau, M., Barmettler, P., Poletti, D., Endres, M., Schauß, P., Fukuhara, T., Gross, C., Bloch, I., Kollath, C., and Kuhr, S., *"Light-cone-like spreading of correlations in a quantum many-body system."* Nature **481**, 484–7 (2012).

Cohen-Tannoudji, C., Dupont-Roc, J., and Grynberg, G., Atom-Photon Interactions: Basic Processes and Applications (Wiley-VCH, New York, 1998).

Collini, E., Wong, C. Y., Wilk, K. E., Curmi, P. M. G., Brumer, P., and Scholes, G. D., *"Coherently wired light-harvesting in photosynthetic marine algae at ambient temperature,"* Nature **463**, 644–647 (2010).

Comparat, D. and Pillet, P., *"Dipole blockade in a cold Rydberg atomic sample,"* JOSA B **27**, 208–232 (2010).

Cooley, J. W. and Tukey, J. W., *"An algorithm for the machine calculation of complex Fourier series,"* Mathematics of Computation **19**, 297–297 (1965).

Curtis, J. E. and Grier, D. G., *"Structure of Optical Vortices,"* Physical Review Letters **90**, 133901 (2003).

Darquié, B., Manipulation d'atomes dans des pièges dipolaires microscopiques et émission contrôlée de photons par un atome unique, Ph.D. thesis, Université Paris Sud - Paris XI (2005).

Derevianko, A., Kómár, P., Topcu, T., Kroeze, R. M., and Lukin, M. D., *"Effects of molecular resonances on Rydberg blockade,"* Physical Review A **92**, 063419 (2015).

van Ditzhuijzen, C. S. E., Koenderink, A. F., Hernández, J. V., Robicheaux, F., Noordam, L. D., and van den Heuvell, H. B. v. L., *"Spatially Resolved Observation of Dipole-Dipole Interaction between Rydberg Atoms,"* Physical Review Letters **100**, 243201 (2008).

Dudin, Y. O., Bariani, F., and Kuzmich, A., *"Emergence of Spatial Spin-Wave Correlations in a Cold Atomic Gas,"* Physical Review Letters **109**, 133602 (2012).

Dudin, Y. O., Li, L., Bariani, F., and Kuzmich, A., *"Observation of coherent many-body Rabi oscillations,"* Nature Physics **8**, 790–794 (2012).

Ebert, M., Gill, A., Gibbons, M., Zhang, X., Saffman, M., and Walker, T. G., *"Atomic Fock State Preparation Using Rydberg Blockade,"* Physical Review Letters **112**, 043602 (2014).

Ebert, M., Kwon, M., Walker, T. G., and Saffman, M., *"Coherence and Rydberg Blockade of Atomic Ensemble Qubits,"* Physical Review Letters **115**, 093601 (2015).

Faoro, R., Pelle, B., Zuliani, A., Cheinet, P., Arimondo, E., and Pillet, P., *"Borromean three-body FRET in frozen Rydberg gases,"* Nature Communications **6**, 8173 (2015).

Feldker, T., Bachor, P., Stappel, M., Kolbe, D., Gerritsma, R., Walz, J., and Schmidt-Kaler, F., *"Rydberg Excitation of a Single Trapped Ion,"* Physical Review Letters **115**, 173001 (2015).

Feynman, R. P., *"Simulating physics with computers,"* International Journal of Theoretical Physics **21**, 467–488 (1982).

Friedrich, H., Theoretical Atomic Physics, Vol. 1 (Springer, Berlin Heidelberg, 1991).

Fuhrmanek, A., Bourgain, R., Sortais, Y. R. P., and Browaeys, A., *"Light-assisted collisions between a few cold atoms in a microscopic dipole trap,"* Physical Review A **85**, 062708 (2012).

Fung, Y. H. and Andersen, M. F., *"Efficient collisional blockade loading of a single atom into a tight microtrap,"* New Journal of Physics **17**, 073011 (2015).

Gabor, D., *"A New Microscopic Principle,"* Nature **161** (1948).

Gaëtan, A., Miroshnychenko, Y., Wilk, T., Chotia, A., Viteau, M., Comparat, D., Pillet, P., Browaeys, A., and Grangier, P., *"Observation of collective excitation of two individual atoms in the Rydberg blockade regime,"* Nature Physics **5**, 115–118 (2009).

Gallagher, T. F., Rydberg atoms, 3rd ed. (Cambridge University Press, 2005).

Gaunt, A. L. and Hadzibabic, Z., *"Robust Digital Holography For Ultracold Atom Trapping,"* Scientific Reports **2**, 1–5 (2012).

Georgescu, I. M., Ashhab, S., and Nori, F., *"Quantum simulation,"* Reviews of Modern Physics **86**, 153–185 (2014).

Gerchberg, R. W. and Saxton, W. O., *"A practical algorithm for the determination of the phase from image and diffraction plane pictures,"* Optik **35** (1972).

Gibson, G., Courtial, J., Padgett, M. J., Vasnetsov, M., Pas'ko, V., Barnett, S. M., and Franke-Arnold, S., *"Free-space information transfer using light beams carrying orbital angular momentum,"* Optics Express **12**, 5448 (2004).

Glaetzle, A. W., Dalmonte, M., Nath, R., Rousochatzakis, I., Moessner, R., and Zoller, P., *"Quantum Spin-Ice and Dimer Models with Rydberg Atoms,"* Physical Review X **4**, 041037 (2014).

Goodman, J. W., Introduction to Fourier Optics, 2nd ed. (Roberts & Company Publishers, 1996).

Gorniaczyk, H., Tresp, C., Schmidt, J., Fedder, H., and Hofferberth, S., *"Single-Photon Transistor Mediated by Interstate Rydberg Interactions,"* Physical Review Letters **113**, 053601 (2014).

Greenberger, D. M., Horne, M. A., and Zeilinger, A., *"Going Beyond Bell's Theorem,"* in Bells Theorem, Quantum Theory, and Conceptions of the Universe (ed. M. Kafatos, 1989).

Grier, D. G., *"A revolution in optical manipulation,"* Nature **424**, 810–816 (2003).

Grimm, R., Weidemüller, M., and Ovchinnikov, Y. B., *"Optical Dipole Traps for Neutral Atoms,"* in Advances In Atomic, Molecular, and Optical Physics, Vol. 42 (2000) pp. 95–170.

Gunter, G., Schempp, H., Robert-de Saint-Vincent, M., Gavryusev, V., Helmrich, S., Hofmann, C. S., Whitlock, S., and Weidemuller, M., *"Observing the Dynamics of Dipole-Mediated Energy Transport by Interaction-Enhanced Imaging,"* Science **342**, 954–956 (2013).

Haas, F., Volz, J., Gehr, R., Reichel, J., and Esteve, J., *"Entangled States of More Than 40 Atoms in an Optical Fiber Cavity,"* Science **344**, 180–183 (2014).

Han, J., Jamil, Y., Norum, D. V. L., Tanner, P. J., and Gallagher, T. F., *"Rb nf quantum defects from millimeter-wave spectroscopy of cold 85Rb Rydberg atoms,"* Physical Review A **74**, 054502 (2006).

Hankin, A. M., Jau, Y.-Y., Parazzoli, L. P., Chou, C. W., Armstrong, D. J., Landahl, A. J., and Biedermann, G. W., *"Two-atom Rydberg blockade using direct 6S to nP excitation,"* Physical Review A **89**, 033416 (2014).

Hardy, J. W., Adaptive Optics for Astronomical Telescopes (Oxford University Press, 1998).

Haroche, S., *"Controlling Photons in a Box and Exploring the Quantum to Classical Boundary (Nobel Lecture),"* Angewandte Chemie International Edition **52**, 10158–10178 (2013).

Hauke, P., Cucchietti, F. M., Tagliacozzo, L., Deutsch, I., and Lewenstein, M., *"Can one trust quantum simulators?"* Reports on Progress in Physics **75**, 082401 (2012).

Hauke, P. and Heyl, M., *"Many-body localization and quantum ergodicity in disordered long-range Ising models,"* Physical Review B **92**, 134204 (2015).

Hazzard, K. R. A., van den Worm, M., Foss-Feig, M., Manmana, S. R., Dalla Torre, E. G., Pfau, T., Kastner, M., and Rey, A. M., *"Quantum correlations and entanglement in far-from-equilibrium spin systems,"* Physical Review A **90**, 063622 (2014).

Heidemann, R., Raitzsch, U., Bendkowsky, V., Butscher, B., Löw, R., and Pfau, T., *"Rydberg Excitation of Bose-Einstein Condensates,"* Physical Review Letters **100**, 033601 (2008).

Heidemann, R., Raitzsch, U., Bendkowsky, V., Butscher, B., Löw, R., Santos, L., and Pfau, T., *"Evidence for Coherent Collective Rydberg Excitation in the Strong Blockade Regime,"* Physical Review Letters **99**, 163601 (2007).

Heidrich-Meisner, F., Honecker, A., and Brenig, W., *"Transport in quasi one-dimensional spin-1/2 systems,"* The European Physical Journal Special Topics **151**, 135–145 (2007).

Isenhower, L., Urban, E., Zhang, X. L., Gill, A. T., Henage, T., Johnson, T. A., Walker, T. G., and Saffman, M., *"Demonstration of a Neutral Atom Controlled-NOT Quantum Gate,"* Physical Review Letters **104**, 010503 (2010).

Jaksch, D., Cirac, J. I., Zoller, P., Rolston, S. L., Côté, R., and Lukin, M. D., *"Fast Quantum Gates for Neutral Atoms,"* Physical Review Letters **85**, 2208–2211 (2000).

Jau, Y.-Y., Hankin, A. M., Keating, T., Deutsch, I. H., and Biedermann, G. W., *"Entangling atomic spins with a Rydberg-dressed spin-flip blockade,"* Nature Physics **12**, 71–74 (2015).

Johnson, T. A., Urban, E., Henage, T., Isenhower, L., Yavuz, D. D., Walker, T. G., and Saffman, M., *"Rabi Oscillations between Ground and Rydberg States with Dipole-Dipole Atomic Interactions,"* Physical Review Letters **100**, 113003 (2008).

Jungen, C., *"Quantum Defect Theory for Molecules,"* in Reports on Progress in Physics, Vol. 46 (1988) pp. 79–103.

Jurcevic, P., Lanyon, B. P., Hauke, P., Hempel, C., Zoller, P., Blatt, R., and Roos, C. F., *"Quasiparticle engineering and entanglement propagation in a quantum many-body system,"* Nature **511**, 202–205 (2014).

Kaufman, A. M., Lester, B. J., and Regal, C. A., *"Cooling a Single Atom in an Optical Tweezer to Its Quantum Ground State,"* Physical Review X **2**, 041014 (2012).

Kazimierczuk, T., Fröhlich, D., Scheel, S., Stolz, H., and Bayer, M., *"Giant Rydberg excitons in the copper oxide Cu2O,"* Nature **514**, 343–347 (2014).

Kruse, J., Gierl, C., Schlosser, M., and Birkl, G., *"Reconfigurable site-selective manipulation of atomic quantum systems in two-dimensional arrays of dipole traps,"* Physical Review A **81**, 060308 (2010).

Kübler, H., Shaffer, J. P., Baluktsian, T., Löw, R., and Pfau, T., *"Coherent excitation of Rydberg atoms in micrometre-sized atomic vapour cells,"* Nature Photonics **4**, 112–116 (2010).

Labuhn, H., Barredo, D., Ravets, S., de Léséleuc, S., Macrì, T., Lahaye, T., and Browaeys, A., *"A highly-tunable quantum simulator of spin systems using two-dimensional arrays of single Rydberg atoms,"* (2015), arXiv:1509.04543 .

Labuhn, H., Ravets, S., Barredo, D., Béguin, L., Nogrette, F., Lahaye, T., and Browaeys, A., *"Single-atom addressing in microtraps for quantum-state engineering using Rydberg atoms,"* Physical Review A **90**, 023415 (2014).

Lee, J. H., Montano, E., Deutsch, I. H., and Jessen, P. S., *"Robust site-resolvable quantum gates in an optical lattice via inhomogeneous control,"* Nature Communications **4** (2013), 10.1038/ncomms3027.

Lengwenus, A., Kruse, J., Schlosser, M., Tichelmann, S., and Birkl, G., *"Coherent Transport of Atomic Quantum States in a Scalable Shift Register,"* Physical Review Letters **105**, 170502 (2010).

Lesanovsky, I., *"Many-body spin interactions and the ground state of a dense Rydberg lattice gas."* Physical review letters **106**, 025301 (2011).

Lester, B. J., Luick, N., Kaufman, A. M., Reynolds, C. M., and Regal, C. A., *"Rapid Production of Uniformly Filled Arrays of Neutral Atoms,"* Physical Review Letters **115**, 073003 (2015).

Li, W., Mourachko, I., Noel, M. W., and Gallagher, T. F., *"Millimeter-wave spectroscopy of cold Rb Rydberg atoms in a magneto-optical trap: Quantum defects of the ns , np , and nd series,"* Physical Review A **67**, 052502 (2003).

Lochead, G., Boddy, D., Sadler, D. P., Adams, C. S., and Jones, M. P. A., *"Number-resolved imaging of excited-state atoms using a scanning autoionization microscope,"* Physical Review A **87**, 053409 (2013).

López-Quesada, C., Andilla, J., and Martín-Badosa, E., *"Correction of aberration in holographic optical tweezers using a Shack-Hartmann sensor,"* Applied Optics **48**, 1084 (2009).

Loudon, R., The Quantum Theory of Light (Oxford Science Publications), 3rd ed. (Oxford University Press, USA, 2000).

Löw, R., Weimer, H., Krohn, U., Heidemann, R., Bendkowsky, V., Butscher, B., Büchler, H. P., and Pfau, T., *"Universal scaling in a strongly interacting Rydberg gas,"* Physical Review A **80**, 033422 (2009).

Lukin, M. D., Fleischhauer, M., Cote, R., Duan, L. M., Jaksch, D., Cirac, J. I., and Zoller, P., *"Dipole Blockade and Quantum Information Processing in Mesoscopic Atomic Ensembles,"* Physical Review Letters **87**, 037901 (2001).

Lundblad, N., Obrecht, J. M., Spielman, I. B., and Porto, J. V., *"Field-sensitive addressing and control of field-insensitive neutral-atom qubits,"* Nature Physics **5**, 575–580 (2009).

Maller, K. M., Lichtman, M. T., Xia, T., Sun, Y., Piotrowicz, M. J., Carr, A. W., Isenhower, L., and Saffman, M., *"Rydberg-blockade controlled-not gate and entanglement in a two-dimensional array of neutral-atom qubits,"* Physical Review A **92**, 022336 (2015).

Manthey, T., Weber, T. M., Niederprüm, T., Langer, P., Guarrera, V., Barontini, G., and Ott, H., *"Scanning electron microscopy of Rydberg-excited BoseEinstein condensates,"* New Journal of Physics **16**, 083034 (2014).

MathWorks,, *"Matlab Fast Fourier Transform (FFT): http://mathworks.com/help/matlab/math/fast-fourier-transform-fft.html,"* (2015).

Matsumoto, N., Inoue, T., Ando, T., Takiguchi, Y., Ohtake, Y., and Toyoda, H., *"High-quality generation of a multispot pattern using a spatial light modulator with adaptive feedback,"* Optics Letters **37**, 3135 (2012).

Mattioli, M., Glätzle, A. W., and Lechner, W., *"From classical to quantum non-equilibrium dynamics of Rydberg excitations in optical lattices,"* New Journal of Physics **17**, 113039 (2015).

Maxwell, D., Szwer, D. J., Paredes-Barato, D., Busche, H., Pritchard, J. D., Gauguet, A., Weatherill, K. J., Jones, M. P. A., and Adams, C. S., *"Storage and Control of Optical Photons Using Rydberg Polaritons,"* Physical Review Letters **110**, 103001 (2013).

Miroshnychenko, Y., Gaëtan, A., Evellin, C., Grangier, P., Comparat, D., Pillet, P., Wilk, T., and Browaeys, A., *"Coherent excitation of a single atom to a Rydberg state,"* Physical Review A **82**, 013405 (2010).

Monroe, C., Campbell, W. C., Edwards, E. E., Islam, R., Kafri, D., Lee, A., Richerme, P., Senko, C., and Smith, J., *"Quantum Simulation of Spin Models with Trapped Ions,"* Proceedings of the International School of Physics 'Enrico Fermi' **189** (2015).

Monroe, C. and Kim, J., *"Scaling the ion trap quantum processor."* Science **339**, 1164–9 (2013).

Moses, S. A., Covey, J. P., Miecnikowski, M. T., Yan, B., Gadway, B., Ye, J., and Jin, D. S., *"Creation of a low-entropy quantum gas of polar molecules in an optical lattice,"* Science **350**, 1507.02377 (2015).

Mourachko, I., Comparat, D., de Tomasi, F., Fioretti, A., Nosbaum, P., Akulin, V. M., and Pillet, P., *"Many-Body Effects in a Frozen Rydberg Gas,"* Physical Review Letters **80**, 253–256 (1998).

Mudrich, M., Zahzam, N., Vogt, T., Comparat, D., and Pillet, P., *"Back and Forth Transfer and Coherent Coupling in a Cold Rydberg Dipole Gas,"* Physical Review Letters **95**, 233002 (2005).

Müller, M., Lesanovsky, I., Weimer, H., Büchler, H. P., and Zoller, P., *"Mesoscopic Rydberg Gate Based on Electromagnetically Induced Transparency,"* Physical Review Letters **102**, 170502 (2009).

Nägerl, H. C., Leibfried, D., Rohde, H., Thalhammer, G., Eschner, J., Schmidt-Kaler, F., and Blatt, R., *"Laser addressing of individual ions in a linear ion trap,"* Physical Review A **60**, 145–148 (1999).

Najafov, H., Lee, B., Zhou, Q., Feldman, L. C., and Podzorov, V., *"Observation of long-range exciton diffusion in highly ordered organic semiconductors,"* Nature Materials **9**, 938–943 (2010).

Nielsen, M. A. and Chuang, I. L., Quantum Computation and Quantum Information: 10th Anniversary Edition, 10th ed. (Cambridge University Press, New York, NY, USA, 2011).

Nogrette, F., Labuhn, H., Ravets, S., Barredo, D., Béguin, L., Vernier, A., Lahaye, T., and Browaeys, A., *"Single-Atom Trapping in Holographic 2D Arrays of Microtraps with Arbitrary Geometries,"* Physical Review X **4**, 021034 (2014).

Olmos, B., Lesanovsky, I., and Garrahan, J. P., *"Facilitated Spin Models of Dissipative Quantum Glasses,"* Physical Review Letters **109**, 020403 (2012).

Olmos, B., Müller, M., and Lesanovsky, I., *"Thermalization of a strongly interacting 1D Rydberg lattice gas,"* New Journal of Physics **12**, 013024 (2010).

Ortner, M., Micheli, A., Pupillo, G., and Zoller, P., *"Quantum simulations of extended Hubbard models with dipolar crystals,"* New Journal of Physics **11**, 055045 (2009).

Osten, W., *"Holography in New Shoes: A Digital-Analogue Interface,"* in 2006 IEEE LEOS Annual Meeting Conference Proceedings (IEEE, 2006) pp. 72–73.

Peter, D., Yao, N. Y., Lang, N., Huber, S. D., Lukin, M. D., and Büchler, H. P., *"Topological bands with a Chern number C=2 by dipolar exchange interactions,"* Physical Review A **91**, 053617 (2015).

Petrosyan, D., Mølmer, K., and Fleischhauer, M., *"On the adiabatic preparation of spatially-ordered Rydberg excitations of atoms in a one-dimensional optical lattice by laser frequency sweeps,"* (2015), arXiv:1511.09214 .

Platt, B. C. and Shack, R., *"History and principles of Shack-Hartmann wavefront sensing."* Journal of Refractive Surgery **17**, 573–577 (2001).

Pohl, T., Demler, E., and Lukin, M. D., *"Dynamical Crystallization in the Dipole Blockade of Ultracold Atoms,"* Physical Review Letters **104**, 043002 (2010).

Ravets, S., Development of tools for quantum engineering using individual atoms: optical nanofibers and controlled Rydberg interactions, Ph.D. thesis, Universite Paris XI (2014).

Ravets, S., Labuhn, H., Barredo, D., Béguin, L., Lahaye, T., and Browaeys, A., *"Coherent dipoledipole coupling between two single Rydberg atoms at an electrically-tuned Förster resonance,"* Nature Physics **10**, 914–917 (2014).

Ravets, S., Labuhn, H., Barredo, D., Lahaye, T., and Browaeys, A., *"Measurement of the angular dependence of the dipole-dipole interaction between two individual Rydberg atoms at a Förster resonance,"* Physical Review A **92**, 020701 (2015).

Reinhard, A., Liebisch, T. C., Knuffman, B., and Raithel, G., *"Level shifts of rubidium Rydberg states due to binary interactions,"* Physical Review A **75**, 032712 (2007).

Reinhard, A., Younge, K. C., and Raithel, G., *"Effect of Förster resonances on the excitation statistics of many-body Rydberg systems,"* Physical Review A **78**, 060702 (2008).

Reymond, G., Schlosser, N., Protsenko, I., and Grangier, P., *"Single-atom manipulations in a microscopic dipole trap,"* Philosophical Transactions of the Royal Society A: Mathematical, Physical and Engineering Sciences **361**, 1527–1536 (2003).

Reymond, G.-O., Etudes expérimentales d'atomes dans un piège dipolaire microscopique, Ph.D. thesis, Universit e Paris Sud - Paris XI (2002).

Richerme, P., Gong, Z.-X., Lee, A., Senko, C., Smith, J., Foss-Feig, M., Michalakis, S., Gorshkov, A. V., and Monroe, C., *"Non-local propagation of correlations in quantum systems with long-range interactions."* Nature **511**, 198–201 (2014).

Robicheaux, F. and Hernández, J. V., *"Many-body wave function in a dipole blockade configuration,"* Physical Review A **72**, 063403 (2005).

Rydberg, J., Recherches sur la constitution des spectres d'émission des éléments chimiques. (Norstedt, 1890).

Saffman, M. and Walker, T. G., *"Analysis of a quantum logic device based on dipole-dipole interactions of optically trapped Rydberg atoms,"* Physical Review A **72**, 022347 (2005).

Saffman, M., Walker, T. G., and Mølmer, K., *"Quantum information with Rydberg atoms,"* Reviews of Modern Physics **82**, 2313–2363 (2010).

Santos, L., Baranov, M., Cirac, J., Everts, H.-U., Fehrmann, H., and Lewenstein, M., *"Atomic Quantum Gases in Kagomé Lattices,"* Physical Review Letters **93**, 030601 (2004).

Schauß, P., High-resolution imaging of ordering in Rydberg many-body systems, Ph.D. thesis (2014).

Schauß, P., Cheneau, M., Endres, M., Fukuhara, T., Hild, S., Omran, A., Pohl, T., Gross, C., Kuhr, S., and Bloch, I., *"Observation of spatially ordered structures in a two-dimensional Rydberg gas,"* Nature **491**, 87–91 (2012).

Schauss, P., Zeiher, J., Fukuhara, T., Hild, S., Cheneau, M., Macri, T., Pohl, T., Bloch, I., and Gross, C., *"Crystallization in Ising quantum magnets,"* Science **347**, 1455–1458 (2015).

Schempp, H., Günter, G., Robert-de Saint-Vincent, M., Hofmann, C. S., Breyel, D., Komnik, A., Schönleber, D. W., Gärttner, M., Evers, J., Whitlock, S., and Weidemüller, M., *"Full Counting Statistics of Laser Excited Rydberg Aggregates in a One-Dimensional Geometry,"* Physical Review Letters **112**, 013002 (2014).

Schlosser, M., Tichelmann, S., Kruse, J., and Birkl, G., *"Scalable architecture for quantum information processing with atoms in optical micro-structures,"* Quantum Information Processing **10**, 907–924 (2011).

Schlosser, N., Reymond, G., and Grangier, P., *"Collisional Blockade in Microscopic Optical Dipole Traps,"* Physical Review Letters **89**, 023005 (2002).

Schlosser, N., Reymond, G., Protsenko, I., and Grangier, P., *"No Title,"* Nature **411**, 1024–1027 (2001).

Schneider, C., Porras, D., and Schaetz, T., *"Experimental quantum simulations of many-body physics with trapped ions."* Reports on progress in physics. Physical Society (Great Britain) **75**, 024401 (2012).

Scholak, T., de Melo, F., Wellens, T., Mintert, F., and Buchleitner, A., *"Efficient and coherent excitation transfer across disordered molecular networks,"* Physical Review E **83**, 021912 (2011).

Schrader, D., Dotsenko, I., Khudaverdyan, M., Miroshnychenko, Y., Rauschenbeutel, A., and Meschede, D., *"Neutral Atom Quantum Register,"* Physical Review Letters **93**, 150501 (2004).

Schrödinger, E., *"Are there Quantum Jumps?"* The British Journal for the Philosophy of Science **III**, 233–242 (1952).

Schwarzkopf, A., Sapiro, R. E., and Raithel, G., *"Imaging Spatial Correlations of Rydberg Excitations in Cold Atom Clouds,"* Physical Review Letters **107**, 103001 (2011).

Shih, C.-Y. and Chapman, M. S., *"Nondestructive light-shift measurements of single atoms in optical dipole traps,"* Physical Review A **87**, 063408 (2013).

Simon, J., Bakr, W. S., Ma, R., Tai, M. E., Preiss, P. M., and Greiner, M., *"Quantum simulation of antiferromagnetic spin chains in an optical lattice."* Nature **472**, 307–12 (2011).

Singer, K., Reetz-Lamour, M., Amthor, T., Marcassa, L. G., and Weidemüller, M., *"Suppression of Excitation and Spectral Broadening Induced by Interactions in a Cold Gas of Rydberg Atoms,"* Physical Review Letters **93**, 163001 (2004).

Somaroo, S., Tseng, C. H., Havel, T. F., Laflamme, R., and Cory, D. G., *"Quantum Simulations on a Quantum Computer,"* Physical Review Letters **82**, 5381–5384 (1999).

Sortais, Y. R. P., Marion, H., Tuchendler, C., Lance, A. M., Lamare, M., Fournet, P., Armellin, C., Mercier, R., Messin, G., Browaeys, A., and Grangier, P., *"Diffraction-limited optics for single-atom manipulation,"* Physical Review A **75**, 013406 (2007).

Struck, J., Ölschläger, C., Le Targat, R., Soltan-Panahi, P., Eckardt, A., Lewenstein, M., Windpassinger, P., and Sengstock, K., *"Quantum simulation of frustrated classical magnetism in triangular optical lattices."* Science **333**, 996–9 (2011).

Texas Advanced Computing Center,, *"8 Things You Should Know About GPGPU Technology,"* Tech. Rep. (https://www.tacc.utexas.edu/documents/13601/88790/8Things.pdf, 2010).

Tey, M. K., Chen, Z., Aljunid, S. A., Chng, B., Huber, F., Maslennikov, G., and Kurtsiefer, C., *"Strong interaction between light and a single trapped atom without the need for a cavity,"* Nature Physics **4**, 924–927 (2008).

Tong, D., Farooqi, S. M., Stanojevic, J., Krishnan, S., Zhang, Y. P., Côté, R., Eyler, E. E., and Gould, P. L., *"Local Blockade of Rydberg Excitation in an Ultracold Gas,"* Physical Review Letters **93**, 063001 (2004).

Tresp, C., Bienias, P., Weber, S., Gorniaczyk, H., Mirgorodskiy, I., Büchler, H. P., and Hofferberth, S., *"Dipolar Dephasing of Rydberg D-State Polaritons,"* Physical Review Letters **115**, 083602 (2015).

Tuchendler, C., Lance, A. M., Browaeys, A., Sortais, Y. R. P., and Grangier, P., *"Energy distribution and cooling of a single atom in an optical tweezer,"* Physical Review A **78**, 033425 (2008).

Urban, E., Johnson, T. A., Henage, T., Isenhower, L., Yavuz, D. D., Walker, T. G., and Saffman, M., *"Observation of Rydberg blockade between two atoms,"* Nature Physics **5**, 110–114 (2009).

Urvoy, A., Ripka, F., Lesanovsky, I., Booth, D., Shaffer, J. P., Pfau, T., and Löw, R., *"Strongly Correlated Growth of Rydberg Aggregates in a Vapor Cell,"* Physical Review Letters **114**, 203002 (2015).

Vermersch, B., Glaetzle, a. W., and Zoller, P., *"Magic distances in the blockademechanism of Rydberg p and d states,"* Physical Review A **91**, 023411 (2015).

Viteau, M., Bason, M. G., Radogostowicz, J., Malossi, N., Ciampini, D., Morsch, O., and Arimondo, E., *"Rydberg Excitations in Bose-Einstein Condensates in Quasi-One-Dimensional Potentials and Optical Lattices,"* Physical Review Letters **107**, 060402 (2011).

Vogt, T., Viteau, M., Chotia, A., Zhao, J., Comparat, D., and Pillet, P., *"Electric-Field Induced Dipole Blockade with Rydberg Atoms,"* Physical Review Letters **99**, 073002 (2007).

Volkov, S. and Wong, T., *"A note on random walks in a hypercube,"* Pi Mu Epsilon journal **9**, 551–557 (2008).

Walker, T. G. and Saffman, M., *"Zeros of RydbergRydberg Föster interactions,"* Journal of Physics B: Atomic, Molecular and Optical Physics **38**, S309–S319 (2005).

Weimer, H. and Büchler, H. P., *"Two-Stage Melting in Systems of Strongly Interacting Rydberg Atoms,"* Physical Review Letters **105**, 230403 (2010).

Weimer, H., Löw, R., Pfau, T., and Büchler, H. P., *"Quantum Critical Behavior in Strongly Interacting Rydberg Gases,"* Physical Review Letters **101**, 250601 (2008).

Weiner, A. M., *"Femtosecond pulse shaping using spatial light modulators,"* Review of Scientific Instruments **71**, 1929 (2000).

Weise, T., Global Optimization Algorithms, Theory and Application, 2nd ed. (http://it-weise.de, 2009).

Weitenberg, C., Endres, M., Sherson, J. F., Cheneau, M., Schauß, P., Fukuhara, T., Bloch, I., and Kuhr, S., *"Single-spin addressing in an atomic Mott insulator,"* Nature **471**, 319–324 (2011).

Wilk, T., Gaëtan, A., Evellin, C., Wolters, J., Miroshnychenko, Y., Grangier, P., and Browaeys, A., *"Entanglement of Two Individual Neutral Atoms Using Rydberg Blockade,"* Physical Review Letters **104**, 010502 (2010).

Windpassinger, P. and Sengstock, K., *"Engineering novel optical lattices,"* Reports on Progress in Physics **76**, 086401 (2013).

Wineland, D. J., *"Nobel Lecture: Superposition, entanglement, and raising Schrödingers cat,"* Reviews of Modern Physics **85**, 1103–1114 (2013).

Yan, S., Huse, D. A., and White, S. R., *"Spin-Liquid Ground State of the $S = 1/2$ Kagome Heisenberg Antiferromagnet,"* Science **332**, 1173–1176 (2011).

Yao, N. Y., Zaletel, M. P., Stamper-Kurn, D. M., and Vishwanath, A., *"A Quantum Dipolar Spin Liquid,"* (2015), arXiv:1510.06403 .

Zeiher, J., Schauß, P., Hild, S., Macrì, T., Bloch, I., and Gross, C., *"Microscopic Characterization of Scalable Coherent Rydberg Superatoms,"* Physical Review X **5**, 031015 (2015).

Zernike, v. F., *"Beugungstheorie des schneidenver-fahrens und seiner verbesserten form, der phasenkontrastmethode,"* Physica **1**, 689–704 (1934).